

**ACOUSTIC MONITORING  
FOR TUNNEL BORING  
IN SOFT SOILS**



**ACOUSTIC MONITORING  
FOR TUNNEL BORING  
IN SOFT SOILS**

PROEFSCHRIFT

ter verkrijging van de graad van doctor  
aan de Technische Universiteit Delft,  
op gezag van de Rector Magnificus prof. dr. ir. J.T. Fokkema,  
voorzitter van het College voor Promoties,  
in het openbaar te verdedigen op dinsdag 18 november 2003 om 13.00 uur

door

**Gerda SWINNEN**

Burgerlijk Mijnbouwkundig Ingenieur  
geboren te Turnhout, België

Dit proefschrift is goedgekeurd door de promotor  
Prof. dr. ir. J.T. Fokkema  
en toegevoegd promotor  
Dr. ir. G.G. Drijkoningen

Samenstelling promotiecommissie:

Prof. dr. ir. J.T. Fokkema,	Technische Universiteit Delft, promotor
Dr. ir. G.G. Drijkoningen,	Technische Universiteit Delft toegevoegd promotor
Prof. dr. ir. C.P.A. Wapenaar,	Technische Universiteit Delft
Prof. ir. J.W. Bosch,	Technische Universiteit Delft
Prof. dr. ir. G. De Roeck,	Katholieke Universiteit Leuven
Prof. dr. ir. L. Halleux,	Katholieke Universiteit Leuven
Dr. ir. D.J.M. Ngan-Tillard,	Technische Universiteit Delft

Copyright ©2003 by G. Swinnen, Section of Applied Geophysics, Department of Applied Earth Sciences, Delft University of Technology.

All rights reserved. No parts of this publication may be reproduced, stored in a retrieval system or transmitted, in any form or by any means, electronic, mechanical, photocopying, recording, or otherwise, without the prior written permission of the author.

Cover design by Peter Peeters.

#### **Support**

The research reported in this thesis has been financially supported by the Centre for Underground Construction (COB), Gouda.

*If you don't start, it's certain you won't arrive.*



# Contents

---

<b>1</b>	<b>Introduction</b>	<b>1</b>
1.1	Tunnelling through history . . . . .	1
1.2	Tunnel boring . . . . .	2
1.3	Soil testing before tunnelling . . . . .	6
1.4	Seismic investigation of the subsurface . . . . .	8
1.5	Data processing . . . . .	11
1.6	Outline of this thesis . . . . .	12
<b>2</b>	<b>TBM, a Seismic Source</b>	<b>15</b>
2.1	Generation of seismic signals . . . . .	15
2.2	Properties of the signal . . . . .	18
<b>3</b>	<b>The Source Inside the TBM</b>	<b>23</b>
3.1	Position of the source . . . . .	23
3.2	Determination of the source . . . . .	26
3.3	Cause of the shear waves . . . . .	30
3.3.1	Engines and pumps . . . . .	30
3.3.2	The measuring equipment . . . . .	31
3.3.3	Friction effects . . . . .	31
<b>4</b>	<b>Imaging around the TBM</b>	<b>35</b>

4.1	Imaging in front of the TBM using external sources . . . . .	36
4.1.1	Experiments . . . . .	36
4.1.2	Results . . . . .	38
4.2	Imaging around the TBM using shear waves emitted by the jacks . .	39
4.2.1	Experiments . . . . .	39
4.2.2	Results . . . . .	40
4.3	Passive vs. active seismic source . . . . .	44
<b>5</b>	<b>WLSQ Optimization of Extrapolation Operators</b>	<b>47</b>
5.1	Phaseshift extrapolation and imaging . . . . .	47
5.1.1	The Kirchhoff integral . . . . .	47
5.1.2	Forward wavefield extrapolator . . . . .	51
5.1.3	Inverse wavefield extrapolator . . . . .	53
5.1.4	Imaging . . . . .	53
5.2	Extrapolation operator optimisation in 2-D . . . . .	54
5.2.1	Phaseshift operator . . . . .	55
5.2.2	Weighted least-squares approximation . . . . .	59
5.2.3	Asymmetric operator design . . . . .	74
<b>6</b>	<b>Operator Performance in Recursive Extrapolation</b>	<b>91</b>
6.1	Forward wavefield extrapolation . . . . .	92
6.2	Inverse wavefield extrapolation . . . . .	99
<b>7</b>	<b>Recursive Migration of Tunnelling Configurations</b>	<b>103</b>
7.1	Boulder in the path of the TBM . . . . .	104
7.2	Foundation in the path of the TBM . . . . .	108

7.3 Layered background . . . . .	111
7.4 Forward propagation of the TBM . . . . .	114
<b>8 Conclusions and Discussion</b>	<b>117</b>
<b>A Field configuration 1</b>	<b>121</b>
<b>B Field configuration 2</b>	<b>125</b>
B.1 Geophones in depth . . . . .	125
B.2 Geophones at the surface . . . . .	128
B.3 Geophones in the TBM . . . . .	128
B.4 Pressure sensors . . . . .	130
B.5 Sources . . . . .	132
B.6 Synchronization . . . . .	132
<b>C Field configuration 3</b>	<b>135</b>
<b>Bibliography</b>	<b>137</b>
<b>Summary</b>	<b>143</b>
<b>Samenvatting</b>	<b>147</b>
<b>Curriculum Vitae</b>	<b>151</b>
<b>Acknowledgments / Dankwoord</b>	<b>153</b>



# Introduction

---

## 1.1 Tunnelling through history

Humans have been looking for shelter, work, materials, communication paths, etc. in the subsurface since prehistory. Tunnels were built thousands of years ago in the Middle East to transport water to cities. Most of the ancient Egyptian pyramids have an underground tunnel system. During the Roman Empire, mining methods were used for the excavation of traffic tunnels through rock near Rome and Naples. In the seventeenth century, there was renewed interest in the construction of tunnels because of improvement in gunpowder. In France, and later in Great Britain and the United States of America, many tunnels were built in channels. In the nineteenth century, the construction of railways in Great Britain led to renewed tunnelling activity. Rock was excavated using gunpowder and chisels. A lack of knowledge of rock and soil mechanics caused many accidents in those days.

Marc I. Brunel designed the first shield tunnelling machine in 1825 for the construction of a tunnel underneath the river Thames in London. The square shield was divided into 12 compartments, each reserved for one worker. As excavation proceeded, bricks were laid down to form the tunnel roof, bottom and walls in the outer compartments. Repeated tunnel collapses and flooding discouraged further use of this method. No further attempt was made to construct another tunnel in London until 1869. For this project, Barlow designed a machine with a round shield. Behind the shield, a tunnel wall was installed using cast iron tunnel elements. Owing to continuous improvement, shield tunnelling became a common method in rock excavation in the 20th century [Stack, 1982].

However, new tunnelling methods were necessary for river crossings where shield tunnelling was impossible owing to soft ground conditions. This led to the development of sink tunnelling. A groove was made in the river, and tunnel elements

were sunk into it. This method was first used for a tunnel under the Detroit River in the United States of America in 1910. The first tunnel constructed in the Netherlands, under the "Nieuwe Maas" in Rotterdam, was also a sunken tunnel. Until the 1940s, there had not been any need for tunnels in the Netherlands. It is a deltaic country dominated by natural and artificial waterways, with a tradition of building bridges instead of tunnels [Leendertse et al., 1997]. Construction of sunken tunnels increased with extension of the railway and road system, and knowledge of sunken tunnelling grew proportionally. Nowadays, sunken tunnels are the most common type in the Netherlands.

A cut-and-cover method has usually been preferred in large cities for the construction of subway systems. This method also consists of excavating a trench. The tunnel is built in the trench, which is backfilled afterwards. Logically, these tunnels often follow the street pattern, causing major disturbances in the city during construction.

In the last decade, hindrance to urban life, together with lack of space, has become an important issue in the Netherlands. The possibility of moving several applications underground has been studied, including transport, storage, working, and even living. A lot of research has been put into tunnel boring methods in the Netherlands [Jovanovic and Jonker, 2003], since they have become a necessity for transportation. Roxo [2003] gives an overview of the advantages of tunnelling in general.

## 1.2 Tunnel boring

Since Brunel's first shield tunnelling machine, tunnel boring has undergone many changes and improvements. Worldwide expertise exists for applications in hard rock. In the Netherlands, soft soil with high variation of soil type both in the horizontal and in the vertical direction, together with the high ground water level, brings new challenges. Experience with tunnelling in soft soil exists only in Japan, where ground conditions are similar to those in the Netherlands. Kurihara et al. [1995], Kanayasu et al. [1995] and Nomoto et al. [1995] describe some of the issues encountered in Japanese tunnelling. Subsurface construction is much more complex than building on the surface. The tunnel and the surrounding soil need to be in a state of equilibrium to ensure a stable construction. During excavation,

the subsoil undergoes considerable change, which needs to be closely monitored and kept under control. Deformation of the soil may result in settling of the earth surface and should be limited as much as possible as it can cause damage to foundations and structures on the surface. Tunnelling in urban areas like is done in Amsterdam [Netzel and Kaalberg, 2003], Barcelona [Borràs i Gabarró et al., 2003], Copenhagen [Nymann and Taylor, 2003], Hong Kong [Storry et al., 2003] increases the risks. Therefore, extensive knowledge of the soil and its geotechnical and hydrogeological behaviour in tunnelling projects is crucial.

Based on the soil profile in the area where the tunnel is bored, a choice of Tunnel Boring Machine (TBM) will be made. TBMs for soft soils use a method of positive ground control, which relies on minimizing the disturbance at the face around the boring machine. Therefore, the induced stress is varied to conform to the resisting capacity of the existing soil conditions. In this way, the resulting ground movements are kept within acceptable limits [Eisenstein and Ezzeldine, 1994]. The soil properties influence the amount of deformation that occurs around the TBM due to the boring process. Consequently, an extensive knowledge of the soil and its geotechnical and hydrogeological behaviour is crucial when tunnelling is undertaken in sensitive environments.

The choice of TBM is also based on the soil profile in the tunnel alignment. The most popular machines are the Bentonite Slurry Shield (BSS) and the Earth Pressure Balance Shield (EPBS) [Arends et al., 1997, Maidl and Hintz, 2003].

The BSS is mainly used in sandy soils. Bentonite slurry is pumped to the working chamber of the TBM. Its pressure has to be high enough to provide a counter pressure that prevents the soil face from collapsing. However, it has to be set below a certain threshold to avoid loss of the supporting medium by seepage to the ground surface. The range of allowable support pressures is limited. It depends on the soil and ground water conditions encountered, the excavation technique, and the tunnel size and cover. The rheological properties of the slurry, including its penetrability, have to be adjusted to the type of soil at the tunnel face. Ideally, the bentonite should infiltrate the soil in front of the TBM cutting wheel and form a thin impermeable filter cake. The slurry pressure is applied to the soil skeleton over the length of this cake. However, in very coarse materials, the slurry infiltrates the soil and fails to build up a cake. Additives are then necessary to allow clogging of the pores and formation of a mud cake. Without this cake, excessive pore pressures might be generated in front of the front face of the tunnel. As a result, effective stresses drop and the stability of the front face is placed at risk [Broere, 2001]. The

transportation capacity of the bentonite slurry is also adapted to the type of soil excavated. During excavation, the cutter wheel of the TBM scrapes the consolidated soil face, and the slurry must be able to transport the excavated soil out of the tunnel before being cleaned in a separation plant and recycled.

With the EPBS, the excavated soil has to provide the counter pressure for a stable bore front. The soil is mixed into a plastic slurry, if necessary by the addition of foam, and is used as support for the soil face. This machine will be used mainly if the subsurface contains a high proportion of clay, since this will reduce the required amount of foam.

Among other things, the choice of tunnelling system is based on topographic and demographic conditions, and on the costs of maintenance, muck handling systems and consumables such as bentonite and additives. But geotechnical factors, including soil type, and mechanical and hydraulic properties, are predominant [Steiner, 1996]. Knowledge of these is also essential in the operation of the TBM when fine tuning of the boring process parameters is necessary to minimize the risk of disturbance.

### **Second Heinenoord Tunnel**

The Second Heinenoord Tunnel is the first bored large-diameter tunnel in the Netherlands. It was constructed in 1997-1999, south of Rotterdam, where it is used to cross the river "Oude Maas". The tunnel consists of two tubes, one for agricultural vehicles and one for other slow-moving traffic. Both tubes have an internal diameter of 7.6 m and are 1350 m in length, of which 950 m is bored. The distance between the tubes is equal to the tunnel external diameter of 8.3 m, as is their soil cover at the deepest point. The position of the tunnel is in an area where the soil layers, with their specific properties, are somewhat irregular; there are cohesive and sandy Holocene and sandy Pleistocene layers, a varied layering that can become even more complex because of old river beds and sea gullies. This is typical of the Dutch subsurface. In the Pleistocene, a large alluvial fan was built up in the Netherlands by the combined rivers Rhine and Meuse and the eastern riversystem. During the glacial periods, deep erosion channels were formed. These were filled with suglacial lake sediments, mainly clays while the Rhine and Meuse continued to supply material to the delta. Sealevel rise after the glaciation caused a rise of the groundwater table on land, resulting in Holocene peat formation. The marine depo-

sists consist mainly of fine sands and clays. Since transgression, the fluvial sandy deposits determine the area of the Meuse. [van Staalduinen et al., 1979]

Since this tunnel was the first experience with a TBM in the typical soft Dutch subsurface, a special project was set up to coordinate the research and gain knowledge on subsurface construction in the Netherlands. In 1994, the COB (Centrum Ondergronds Bouwen = Centre for Underground Construction) was formed, and it initiated a five-year program of cooperation between government, industry and universities. Aspects of the research program included stability of the TBM front face, changes in the soil mass before, during, and after the passage of the TBM, stresses in the rings of the tunnel lining, effects of the boring process on the environment, and considerations regarding planning, risk and cost [Wermer, 1997, Peters and Plekkenpol, 1997].

Because “Second Heinenoord Tunnel” was a research project, many tests were carried out at various stages of the construction [Arends et al., 1997, Bakker et al., 1999]. They can be divided in four groups.

(1) Boring technology: The tunnel was bored with a Bentonite Slurry Shield. The efficiency of this machine was investigated in both sand and clay layers. Sensors were installed at the head of the TBM to monitor pressures and stability at the front face. At the shield, forces in the hydraulic jacks were registered. The progression velocity of the TBM was also important.

(2) Construction of tunnel tubes: In two tunnel rings of the first tube, measuring systems were incorporated to register the interaction between tunnel segments, and the influence of the surrounding soil on the tunnel lining and vice versa. These applications were maintained for three years to investigate the effect of the construction of the second tube, and effects over time.

(3) Geotechnics: On both banks of the river, testing fields were set up. Before, during and after passage of the TBM, numerous sensors registered settings at the earth surface, in the subsurface, stress changes in the soil, and water pressures around and in the path of the tunnel. Some of these sensors will stay in place to monitor long-term effects on the soil.

(4) Aspects of vibration, environment and risk.

The construction of the first tunnel tube started at the North river bank. On this bank, the boring conditions were more homogeneous as the tunnel is located mainly in sandy Holocene deposits. Since the boring process can be controlled better, the evaluation of the test results is easier [Leendertse et al., 1997, Wermer, 1997].

In the framework of the COB, the Botlek Railroad Tunnel, part of the Betuweroute near Rotterdam [Jonker et al., 2003], is a second research project. This tunnel is also being bored under the Oude Maas, this time using an EPBS. The project can build on the experiences of the Second Heinenoord Tunnel, but will have to deal with previous unsolved problems and new challenges.

The Betuweroute is a double-track railway for freight transport in the Netherlands for which three tunnels had to be completed: The Botlek railway tunnel, the Sophia railway tunnel in the West of the Netherlands and the tunnel Pannerdensch Kanaal near the border with Germany [Jonker et al., 2003]. Another tunnelling project in the Netherlands is the Green Heart Tunnel in the west of the Netherlands, part of the High Speed Line from Amsterdam to the Belgium border [Aartsen and Wijnants, 2003]. The Westerschelde Tunnel, connecting Zeeuwsch Vlaanderen with the rest of Zeeland in the South of the Netherlands, is one of the longest bored tunnels in the world [de Leeuw and Oele, 2003]. The North-South line, a new metroline, is built underneath the city of Amsterdam [Netzel and Kaalberg, 2003].

### 1.3 Soil testing before tunnelling

Before tunnelling is started, it is common to develop schematically the underground structure along the trajectory of the tunnel. Soil investigation consists of different tests, both in situ and in laboratories, which are combined to produce as accurate a picture of the subsurface as possible [Arends et al., 1997]. Soil samples of various qualities can be recovered from vertical bore holes using different technologies. Cuttings washed out of the bore hole with the boring fluid give a rough indication of the soil type encountered: gravels, sands, silts, clay or peat. Disturbed samples can be analyzed in the laboratory to obtain better soil identification and to perform some index tests. Soils are then classified based on their grain size distribution, organic content, colour, water content and density. Their primary and secondary constituents are specified. Undisturbed samples are necessary to obtain the soil's stress-strain response and its hydraulic properties in the laboratory. Bore holes made to recover samples and establish the soil stratigraphy can also be used for instrumentation purposes. Piezometers, extensometers or inclinometers can be installed in the bore holes for geotechnical control of the boring process. Storry et al. [2003] explains the instrumentation and monitoring of ground movements both in soil and rock, during construction of the Tsing Tsuen tunnels in Hong Kong. The remainder of the bore holes are sealed to limit their influence on tunnelling and settling of the surface.

Another way to derive information on the structure of the subsurface is by cone penetration tests (CPTs) or soundings. A cone is pushed hydraulically into the ground. The resistance of the soil and the friction along the cone are registered and interpreted in terms of soil type and geotechnical properties. Water pressure changes generated during the cone penetration can also be recorded to obtain a better definition of the soil thin layers and the soil permeability in general. Various transducers can also be mounted inside the cone to obtain information on soil deformability, small strain shear modulus, electric conductivity, or in situ density. Other types of equipment, such as the vane test apparatus and the self-boring pressure meter can also be mobilized to perform in situ tests. However, they are less popular in the Netherlands.

As far as possible, soundings and borings are performed in the vicinity of the alignment of the tunnel, but not exactly in the position where the tunnel tubes will be bored [Wermer, 1997]. This prevents disturbance of soil stability above the tunnel, which could result in unwanted ground movements during excavation. As a result, the soil profile along the trajectory of the tunnel itself is not measured, but is derived by interpolation of the data from the discontinuous set of soundings and borings, supplemented with historical geological knowledge of the area. Soundings are usually performed at a 25 to 50 m spacing and show only vertical changes at one location. Criteria to identify on a sounding a layer, what the layer is made of, and how it shows up on contiguous CPT logs, are lacking [Ngan-Tillard et al., 2003]. Layers have various lateral extents and expressions, and only the most continuous layers can be spotted on adjacent CPTs. Small heterogeneities and irregular soil changes are easily missed. In addition, a layer can present characteristics showing a high degree of spatial variability. CPTs at 50, even 25 m spacing cannot detect this spreading accurately.

However, as explained above, the knowledge of the subsurface structure is crucial for fine tuning of the boring process. Erroneous predictions of the soil stratigraphy and non-detection of sand lenses with high pore water pressures can cause instability of the tunnel front face, ground disturbance, damage to neighbouring structures, and stagnation of the TBM, leading to additional cost. Unexpected geological features can also slow down tunnelling progress. This is the case with peat layers, which are difficult to erode, owing to their tough structures. Obstacles buried in the path of the TBM are more damaging. These can be boulders, remains of older subsurface constructions, bombs, etc. The TBM is designed to bore through soft

soils and is not suitable for demolishing these hard obstacles. If they are detected beforehand, the obstacles can be removed or the trajectory of the tunnel can be adjusted.

#### 1.4 Seismic investigation of the subsurface

Complementary to the geotechnical survey, a seismic investigation of the area would result in a much more accurate profile of the subsurface. In oil and gas exploration, seismics is a commonly used technique. Oil and gas fields at a depth of a few kilometres are detected, and the large geological structures of the subsurface are mapped. For the shallow subsurface, shear wave seismics is often applied. Shear waves are much more suitable in the soft soils of the shallow subsurface than compressional waves. Compressional waves are mainly influenced by pore fluids, while shear waves only travel in solid soil. In a seismic survey, a grid of geophones at the earth surface records the reflections from contrasts between soil layers and from obstacles and voids. Processing of the data gives a continuous image of the reflectors in the subsurface, both vertical and lateral. Combination of seismic information with data from soundings and borings gives a very reliable subsurface profile of the area. At the locations of the soundings and the borings, the properties of the soil are known accurately. The reflectors registered in the seismic data sets can be linked with the different soil layers at these positions. Seismic sections can be used as a guideline for interpolation between the different sounding and boring points, resulting in a much more complete soil profile of the area. Suyama et al. [1986], Brouwer et al. [1997] Ghose et al. [1998] Ghose and Goudswaard [2001] and Ghose [2003] describe the integration of data from shallow shear-wave reflection data and CPT data. Figure 1.1 shows a seismic section and CPT made near Rotterdam. In the seismic section, a number of distinct reflection events from very shallow to all the way up to 30 m depth can be noticed. The clear S-wave reflection events at around 3-4 m and 6-12 m correspond to the Holocene sand-clay boundaries and match well with the sharp changes in the CPT data. In seismic section we notice also clear events at around 23-25 m, which is the Holocene-Pleistocene boundary evident in the CPT data. Falk [1998] gives an evaluation of the available geophysical methods for pre-investigation of the subsurface as they were investigated for construction of the fourth Elbe Tunnel in Germany.

Even with seismic surveys, there will be heterogeneities that cannot be detected from the earth surface. In addition, it is difficult, if not impossible, to perform

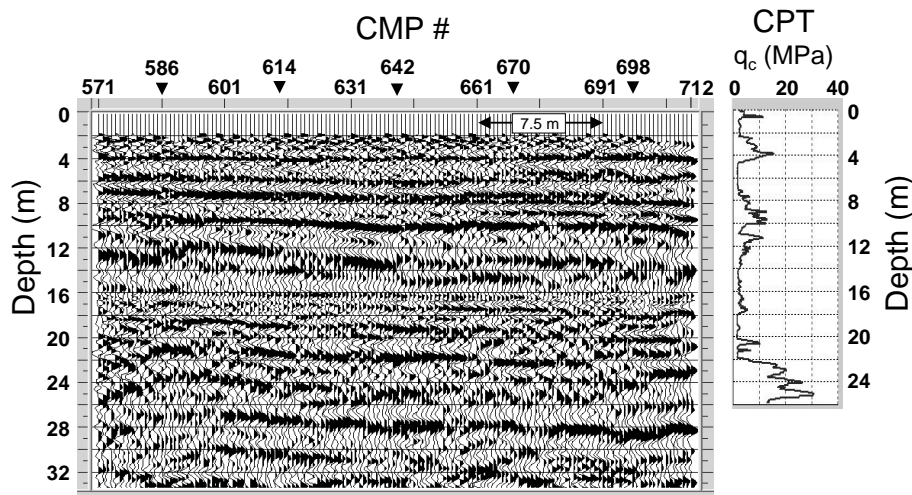


*Figure 1.1: Section from shallow shear wave seismics linked with CPT measurement [Ghose and Goudswaard, 2001]*

geotechnical and/or seismic surface investigation in certain places, e.g., urban areas. In these cases, information about the subsurface has to be gathered from geological data archives. As much knowledge as possible about the composition of the soil is necessary in cities because the risks and consequences of soil subsidence are much larger than in the countryside. In addition, the presence of subsurface constructions has to be taken into account. If the TBM hits a foundation, not only might the boring machine be damaged, but also the stability of the building that the foundation supports might be affected.

These problems can be resolved with the use of a monitoring system on the head of the TBM that continuously measures the situation of the soil in front of the tunnelling machine. When local soil changes are registered by such a system, the boring parameters can be adjusted in time. When obstacles are detected, it is too late to change the trajectory of the tunnel drastically. However, damage to the TBM is avoided and necessary measures can be taken. In this thesis, different aspects of using shear wave seismics for looking ahead of the TBM are investigated. Part of this work has been guided by experiments that have been performed at the first bored tunnel in the Netherlands, the Second Heinenoord Tunnel. During drilling of this tunnel, the bore front collapsed owing to soil disturbance from an old boring hole made for the construction of the First Heinenoord Tunnel. In addition, large boul-

ders from the bottom of the river blocked the path of the TBM. This caused serious delays that could have been avoided if a good seismic system had been available. Monitoring is also important in rock as experienced during construction of metro tunnels in Porto in weathered granite [Grasso et al., 2003] where a combination of a highly heterogeneous subsurface and discontinuities filled with weak materials where the cause of many sudden brittle collapses.

In hard rock, seismic prediction ahead of the tunnel face has been successful in providing information about abrupt changes in rock quality and formation boundaries, which could not be obtained from surface investigations. During the construction of the Tsukui conduit tunnel in central Japan, a horizontal seismic profiling system was applied [Inazaki et al., 1999]. Amberg Measuring Techniques developed a tunnel seismic prediction system (TSP) which was used in Switzerland [Sattel et al., 1992], Japan, South-Korea and Sweden [Sattel et al., 1996]. Kobayashi et al. [2003] describes the seismic true reflective tomography system installed on the TBM for the excavation of the Fujikawa Tunnel in Japan.

After an extensive literature investigation on systems that are used or being developed for monitoring the soft soils at the tunnel face [van Deen and van Lange, 1996], COB sponsored the development of two monitoring tools. First there is the so-called "Speurheus" [COB/CUR, 1999], an acoustic system applied as a pilot drill along the trajectory of the future tunnel, using directional drilling. In this set-up, the tool would mainly be suited for imaging the subsurface before construction of the tunnel. The use of a radar system in the Speurheus has also been considered, but the low penetrability of the waves in the soft Dutch soils makes acoustics preferable. In the first prototype, electromagnetic and geoelectric bore hole tools were also installed, but they only gave a small amount of information about structures at a distance from the bore hole.

The second system, the so-called "Prikneus" or horizontal cone penetration test (HCPT) [Broere, 2001, van Deen et al., 1999] is penetrated through the front shield of the TBM to investigate soil some 10 m ahead of the tunnel face. Its measurements have to be performed during installation of the tunnel elements when the TBM is not progressing. The incorporation of both systems into one tool is not considered. The main reason for this is that the geophysical tool would require a diameter of 10 to 20 cm while standard CPT diameters vary around 36 mm. [COB/CUR, 1999]

Research on a system using seismic compressional waves in soft soils has been performed by Kneib et al. [2000] using the SSP 202 system by Amberg Measuring Technique. This system has one or two compressional wave transmitters and two or more receivers installed on the cutter wheel arms of the TBM. The SSP 202 was used during construction of a tunnel in Duisburg-Meiderich in Germany

[Falk, 1998]. The performance of the system during rotation of the cutter wheel was tested. Interfering signals, such as background noise, turned out to be at least one magnitude stronger than the signals emitted by the geophysical system. They could be separated using extensive processing. However, limiting the processing time is an important issue in the development of a system where the results of the monitoring need to be quickly available to the drilling crew. This system was also implemented on the TBMs for the construction of the Betuweroute, but gave generally disappointing results [Jonker et al., 2003].

In this thesis, the seismic energy that is emitted by the tunnelling machine itself is analyzed. This energy is generated by the excavation process. Consequently, the TBM would not have to be idle. This avoids delay if measurements take longer than the installation of a tunnel ring, or if the TBM would have to be stopped to make extra recordings, or if a continuous advance method is used where excavation and segment erection happens simultaneously [Hosaka et al., 2003, B  ppler and Jonker, 2003]. Similar systems have been applied in hard rock tunnelling, using the energy from tunnel blasting or vibrations from the TBM as it cuts rock as a seismic source [Petronio et al., 2000, Ashida et al., 2002], and in borehole drilling where the drill-bit energy is a seismic source [Rector and Marion, 1991]. If the energy emitted by the TBM while drilling in soft soil is useful as a seismic source, considerable development costs could be avoided.

## 1.5 Data processing

The application of seismics in tunnelling brings about new problems in data processing. One of the traditional migration methods used in oil and gas exploration is phase shift migration [Gazdag, 1978]. This is a recursive method: the recorded wave field is extrapolated in small steps parallel to the receiver plane, where the output for one level becomes the input for the next extrapolation step. This allows velocity variations of the subsurface parallel to the receiver plane. In tunnelling applications, with source and receivers on the cutter wheel, the receivers will be in a vertical plane while layering is mainly horizontal. Recursive space-frequency migration will also take variations within the extrapolation level into account by using an extrapolation operator based on the local velocity.

Traditional migration methods assume thousands of receivers spread over a very large surface. This is common in surface seismics, since an extensive area has to be examined. When installing a source and receivers on the cutter wheel of a tun-

nelling machine, the number of receivers and the aperture of the measurements are limited by the diameter of the TBM. In the case of the Second Heinenoord Tunnel, this was only 8.3 m. Because of these limitations, the common migration techniques will generate errors in the data. They will not make optimal use of the small amount of data that are available. With only a few receivers, it is much more difficult to obtain a clearly focussed image. New extrapolation operators are necessary to improve migration of seismic tunnelling data. Their design is based on the number of receivers installed on the cutter wheel of the TBM, and they need to take into account all the information that is present in the recorded data sets.

It is important to take into account the aspect of time when developing the data processing software for imaging in front of the TBM. After recordings are made, the relevant information should be available to the drilling crew within a short time, depending on how far ahead of the front face the soil can be imaged accurately, and on the rate of progress of the TBM. The sooner heterogeneities that would influence the boring process are reported, the less the risk, the better the measures that can be taken, and the less the delay in tunnel construction.

## 1.6 Outline of this thesis

The first chapters of this thesis give an overview of experiments that were performed at the site of the Second Heinenoord Tunnel that was bored in the Netherlands in 1997 and 1998. The main purpose of the experiments was to investigate the seismic energy generated by the TBM itself. If the tunnelling machine emits controllable seismic waves, the cost and development of an active source that could be installed on the head of the TBM could be avoided. In that case, the TBM could be used as a seismic source for monitoring ahead of the tunnel face. In chapter 2, all energy emitted by the TBM is analyzed. It is shown that the machine emits shear waves. The hydraulic jacks at the end of the shield are identified as the source of these seismic signals in chapter 3. Next, the applicability of the TBM as a seismic source is tested in chapter 4. The best location for installing seismic receivers is at the head of the TBM on the cutter wheel. Therefore, the ability of shear waves to penetrate the bentonite slurry at the tunnel face is investigated. Furthermore, the performance of the seismic signals is tested by trying to detect a second tunnel tube situated next to the tunnelling machine.

---

The next chapters of this thesis describe a synthetic study. Since the TBM, as a seismic source, turned out to be difficult to control, a configuration with an active source and receivers on the cutter wheel of the TBM is suggested. It is shown that traditional data processing techniques have to be adjusted for tunnelling applications in chapter 5. New asymmetric short spatial extrapolation operators are designed, based on a weighted least-squares optimization method, so that they are accurate and stable in a recursive extrapolation scheme. The performance of these new operators in both forward and inverse extrapolation is tested and compared with similar symmetric short extrapolation operators in chapter 6. Finally, in chapter 7 reflection data sets for some typical tunnelling configurations are modelled. They are processed using different recursive migration methods, including migration with symmetric and asymmetric operators.

The conclusions and a discussion based on the research described in the thesis are set out in chapter 8.



## TBM, a Seismic Source

---

*Performing seismic investigations requires the presence of a source and receivers. This source is preferably active and controllable. For tunnelling applications, source and receivers would be best installed on the TBM instead of the earth surface so that the use of the seismic system is not dependent on external factors above ground. This chapter investigates if any element of the TBM itself generates seismic energy that would be useful as a source for imaging the subsurface. If this source is controllable, costs for the development and installation of seismic transducers for tunnelling applications can be avoided.*

### 2.1 Generation of seismic signals

The presence of a seismic source generating energy from a TBM into the subsurface can be determined with a small preliminary survey. At the start of the construction of the Second Heinenoord Tunnel, the TBM passed underneath the Test Field North. A few lines with 3-component geophones were set up above the trajectory of the TBM. These geophones were firmly attached to the ground, and they registered any seismic energy coming from the subsurface. A localized source will be very clearly visible in a time-distance plot of the recordings on one geophone line. The emitted wave will be registered first by the geophone directly above the source since it is at the shortest distance. The wave will have to travel a longer path to reach the other geophones. In the time-distance plot, this will give rise to a hyperbolic event.

The recordings at the Test Field North showed a very low-frequency signal that could not originate from the TBM since no hyperbolic events could be spotted. This noise was traced back to a separation plant used to separate the excavated soil from

the bentonite slurry. During acquisition, it could be filtered out of the data. Several filters were tested and finally a 50 Hz 12 dB/octave low-cut filter was used in all further measurements. Once the filter was applied, the recordings show pulse-like signals with a hyperbolic time-distance dependency. Based on the approximate position of the TBM during the measurements, it can be concluded that these waves were actually generated by the machine. These results give a convincing reason to extend the research on the use of the TBM as a seismic source.

A more elaborate set of measurements was performed when the TBM reached the other bank of the Oude Maas, on the Test Field South. The set-up for these seismic recordings is described in detail in Appendix A. Measurements were taken on several lines on the earth surface, depending on the position of the TBM. Two geophone lines were laid out perpendicular to the axis of the tunnel. On these so-called cross-lines, 3-component geophones were used. An in-line with 1-component geophones was placed parallel to the tunnel axis. Although only limited distortion from the separation plant was expected on this side of the river, all the recordings were filtered in the field with the same 50 Hz 12 dB/octave low-cut filter.

Figure 2.1 shows time-distance plots of the three components, one vertical and two horizontal, of a recording on a line of geophones, perpendicular to the axis of the TBM (cross-line 1 in Figure A.1). Of the horizontal components, the in-line component is recorded parallel to the axis of the tunnel; the cross-line component lies perpendicular to that axis. At the time of this measurement, the TBM was drilling at a horizontal distance of 24 m from the recording line. Except for the low-cut filtering in the field, no processing has been performed on the data.

Despite the small signal-to-noise ratio, hyperbolic events are visible in the data, mainly in the horizontal components. The vertical energy is also registered, but recording of this component contains more noise; the events are much weaker. Similar measurements while the TBM was idle show no hyperbolic events at all. Therefore, it can be said that the TBM is a source of seismic waves; it generates pulse-like signals that can be registered by the geophones.

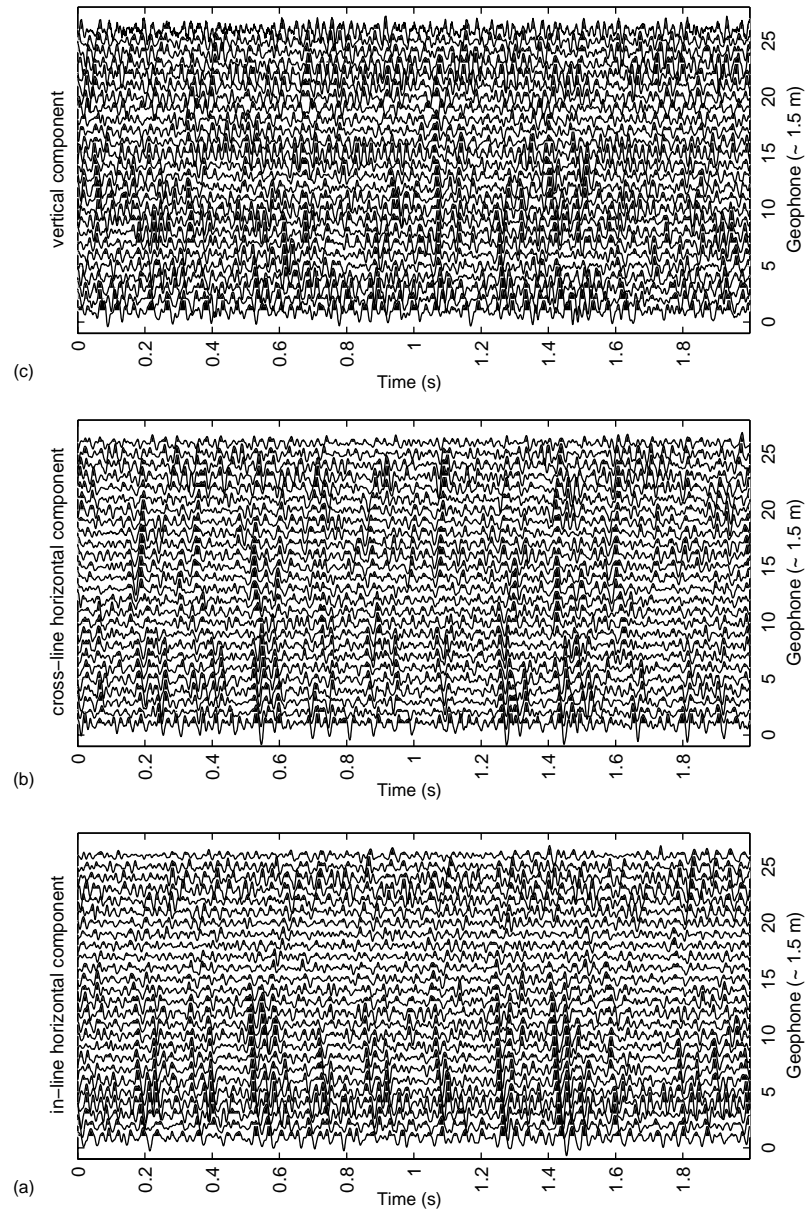


**Figure 2.1:** Time-distance plot of the 3 components of the signals generated by the TBM recorded on cross-line 1, in-line horizontal component (a), cross-line horizontal component (b), vertical component (c)

## 2.2 Properties of the signal

Figure 2.1 indicates that the recorded signals contain more horizontal than vertical energy. The vertically polarized waves are very weak. To determine exactly which type of wave is emitted by the TBM, the energy content of the different components is compared. The normalized energy content  $E_i$  of component  $i$  is calculated as

$$E_i = \frac{1}{N_s N_t} \sum_{n_s=1}^{N_s} \sum_{n_t=1}^{N_t} A_i^2(n_t, n_s). \quad (2.1)$$

$N_s$  represents the number of samples,  $N_t$  represents the number of traces, and  $A_i$  represents the amplitude of component  $i$ . This energy is determined for all components of several measurements, all recorded by the same geophone line but with the TBM at three different lateral positions. The results are shown in Figure 2.2.

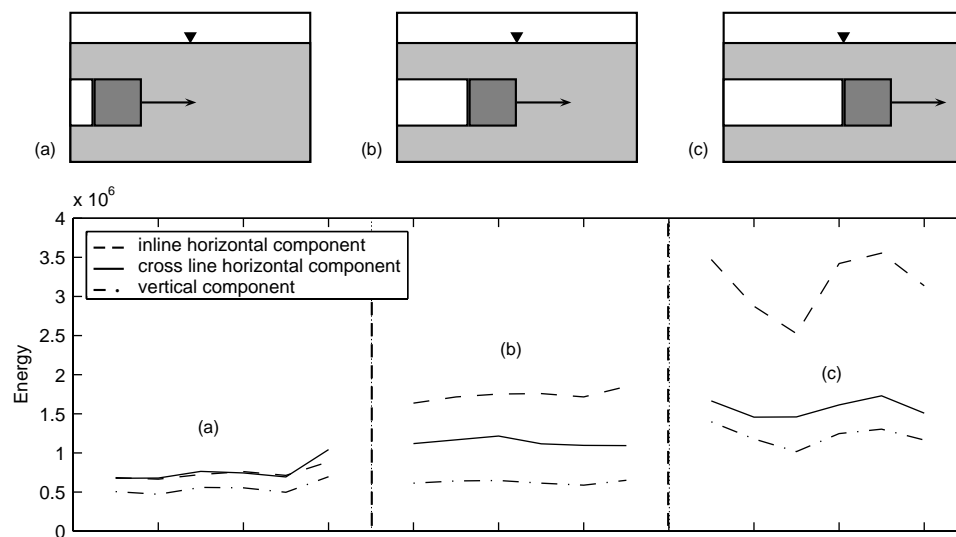


**Figure 2.2:** Energies of the different components of the recorded signals at cross-line 2 at different positions of the TBM, position of the head of the TBM compared to geophone line: 8 m in front (a), directly below (b), 8 m behind (c)

The sketches at the top of Figure 2.2 indicate the three different positions of the

TBM when measurements are made: (a) when the head of the TBM is about 8 m in front of the geophone line, (b) when the head is directly below the geophone line, and (c) 8 m behind the head of the TBM after it has passed the geophone line. Each of the three sets contains six recordings. During the different measurements of each set, the TBM moves forward a few centimetres, but not enough to distort the results. When the TBM is still in front of the geophone line (set (a)), the energy content of both horizontal components is almost the same; the vertical energy is slightly less. When the TBM has reached the point where the head is directly below the geophone line (set (b)), the vertical energy is still at the same level as before, the energy content of the cross-line horizontal component has increased slightly, and the in-line horizontal component has become stronger. When the head is about 8 m behind the geophone line (set (c)), the tail of the TBM is directly below this line since the machine has a length of 8 m. The energy content of the vertical and the cross-line horizontal component is slightly higher than that of the previous position, and the in-line horizontal component shows a significant increase. Over all recordings, the vertical component contains less energy than the horizontal component. Therefore, it can be assumed that horizontal shear waves are generated. When the TBM approaches the geophone line, the in-line component, which is parallel to the axis of the TBM, becomes dominant.

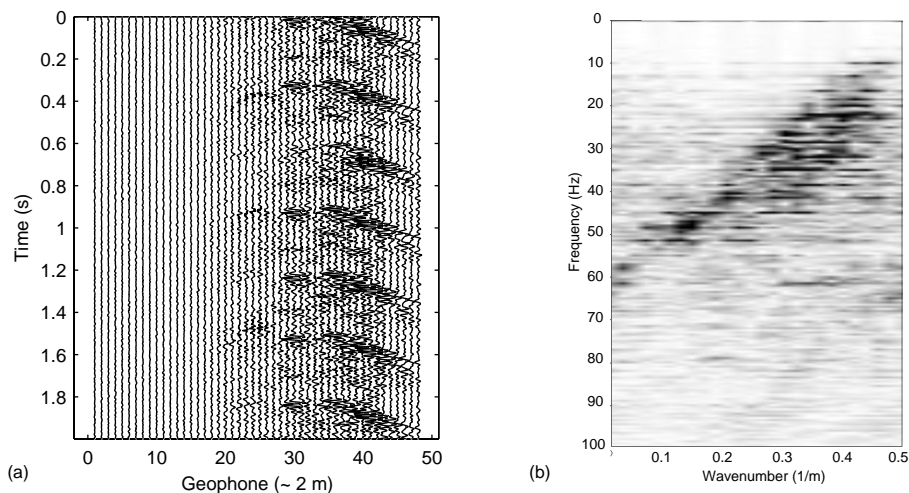


**Figure 2.3:** Vertical component of the signals recorded on the in-line (a) with its matching spectrum in the frequency-wavenumber domain (b)

The average wave speed, with which the disturbance propagates through the medium, is an important property of a seismic wave. The wave speed gives a clear indication of the wave type as it is related to the soil types that the wave travels through. The wave speed is determined from measurements of a geophone line parallel to the tunnel axis (in-line in Figure A.1). This line consists of 1-component geophones that only register the vertical component of the seismic energy. The time-distance plot of Figure 2.3a, shows hyperbolic events that indicate the presence of the seismic source near the geophone line.

The spectrum in the frequency-wave number domain of the recording shown in Figure 2.3a, is plotted in Figure 2.3b. This so-called  $(f, k)$  spectrum is the 2D Fourier-transform both in time and in distance. All energy generated by events with the same wave speed is represented by one line in this spectrum; the slope of the line indicates the wave speed,  $v = f/k$ . In Figure 2.3b, one main event can be detected with a wave speed of  $v = 100$  m/s. Similar processing of the data recorded on Test Field North resulted in a wave speed of  $v = 200$  m/s. Cone penetration tests (CPTs) have shown that the subsurface of Test Field North consists mainly of sand. At Test Field South, the subsurface is more heterogeneous, and a higher peat and clay content is found. Waves that travel through peat and clay

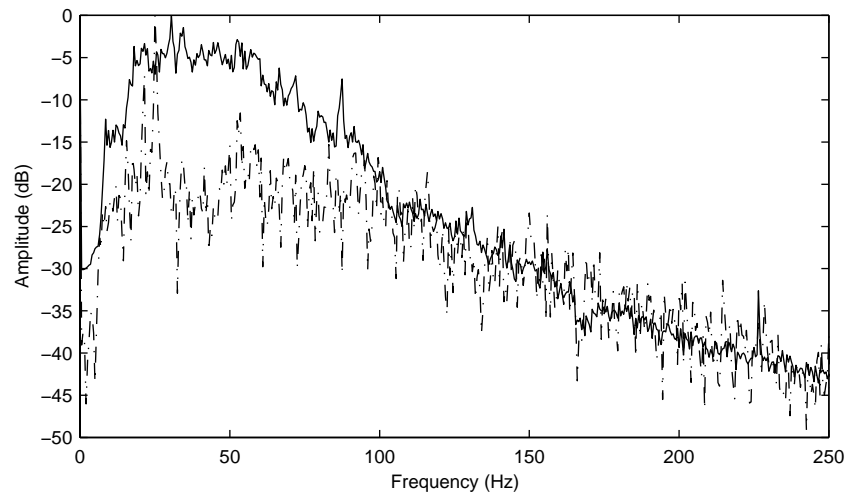


**Figure 2.4:** Average amplitude spectra of the horizontal in-line component of the signal (solid line) and the noise on cross-line 2 (dashed line)

have a lower seismic wave speed, which explains the lower average wave speed of the waves in Test Field South. The wave speeds measured on both test fields are in the characteristic range of shear waves in soft soils. Compressional wave speeds of water-saturated soft soils are dominated by the water-wave speed of 1500 m/s. Therefore, these waves would travel much faster in this shallow subsurface with a ground water level at 3 to 4 m below the earth surface. Thus, the measured wave-speed values support the assumption that the TBM generates shear waves and not compressional waves.

In Figure 2.4 the frequency content of a recording made on cross-line 2 is plotted. At the time of the recording, the TBM has passed the geophone line and the head is located 8 m behind the geophones. Figure 2.2c shows that, at this point, the energy content of the signals is high. All the plots shown so far are made while the TBM is drilling. It is only then that the events can be seen in the data. When the TBM is idle, no subsurface source is detected in the data and only background noise is registered. The frequency content of such a noise measurement on the same geophone line is also plotted in Figure 2.4.

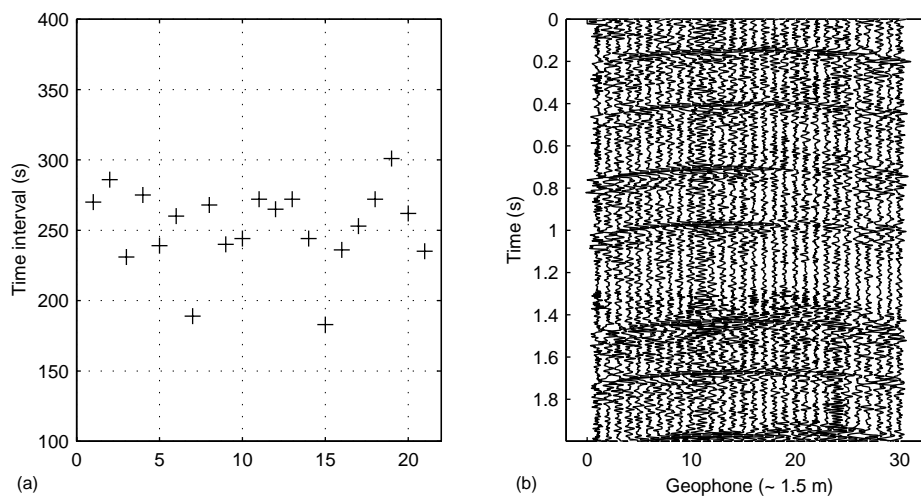


**Figure 2.5:** (a) Time-shifts between subsequent signals for recordings on cross-line 2, (b) Horizontal in-line component of a signal with clearly varying periods recorded on cross-line 2

Below 100 Hz, the signals have a stronger frequency spectrum than the noise. Above 100 Hz, both spectra mainly coincide. For these higher frequencies, any signals are dominated by the background noise. The useful frequency spectrum of the signals is situated in the band between 5 and 100 Hz where the signals are stronger than -20 dB. The same behaviour can be seen in frequency spectra of measurements that are made when the TBM is at different positions relative to the geophone line. Therefore, it can be concluded that the seismic waves generated by the TBM have a frequency range between 5 and 100 Hz.

In combination with the wave speed, the resolution can be calculated. The wavelength, at an average frequency of 50 Hz, is  $\lambda = v/f = 2.2$  m. This gives a resolution of  $\lambda/2 = 1.1$  m.

For all recordings, an average of eight signals is registered during a period of two seconds. The period between these signals also provides information about the source. For several measurements, the exact time shifts between subsequent arrivals of the signals are determined using autocorrelation. The results are plotted in Figure 2.5a. It shows that the period varies significantly. There is an average value of 250 ms, but periods of 300 and 180 ms are also registered. A clear example of these large variations is given in Figure 2.5b.

## The Source Inside the TBM

---

*In the previous chapter, it was shown that seismic signals are generated in the subsurface while the TBM is drilling. To use these signals for imaging the area in front of the TBM, it is necessary to define their exact source; it is vital to know where the source is located and what triggers it. The emission of the signals should be controllable to make the measurements reliable. Therefore, the working principles of the source have to be determined.*

### 3.1 Position of the source

Defining the position of the source is the first step in determining the origin of the seismic signals. The machine occupies a large volume in which the source can be situated. In Figure 3.1, a time-distance plot of both an in-line and a cross-line geophone line is shown. These measurements were made during the same experiments as described in Chapter 2. In the in-line direction (Figure 3.1a), the TBM is parallel to the geophone line, moving from geophone 48 towards geophone 1. The vertical component of the seismic waves is plotted, since this is the only component measured by the 1-component geophones on this line. The apex of the hyperbola indicates the horizontal position of the source in the subsurface. The geophones directly above the source register its sound first. The apex can be located approximately at geophone 35. From the data recorded by the contractor inside the TBM, the exact position of the TBM in the subsurface at each moment can be determined. At the time of the recording of Figure 3.1a, the foremost point of the TBM is situated between geophone 31 and 32. The arrow indicates this point. This means that the sound is not generated at the front of the TBM near the cutting wheel, but about 8 m behind the front. The energy curves in Figure 2.2 confirm this result. The energy

of all components increases significantly when the TBM has passed the geophones line by a few metres.

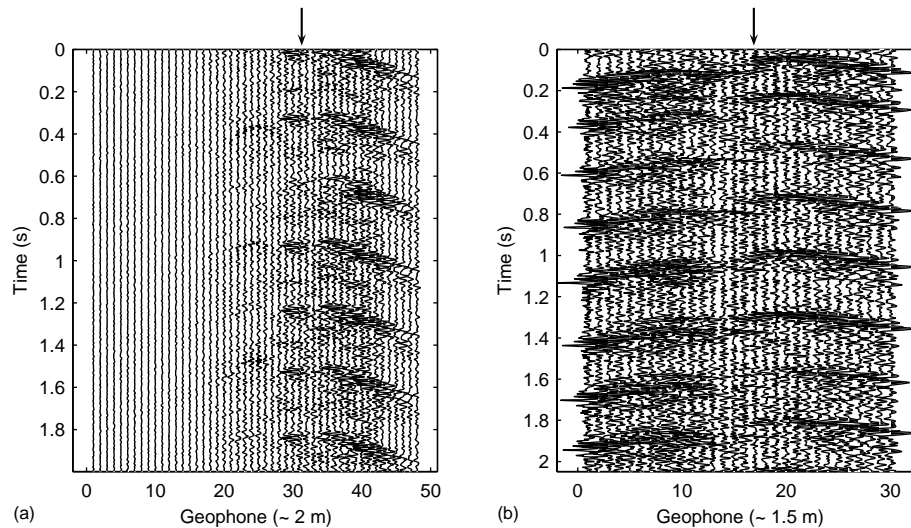


**Figure 3.1:** Localisation of the TBM in the vertical component of the signal recorded on the in-line (a), the horizontal cross-line component on cross-line 2 (b)

The cross-line geophones record all components of the signals. In Figure 3.1b, the cross-line horizontal component is plotted because it is stronger than the vertical component. The TBM passes perpendicularly beneath the geophone line. In this case, the arrow indicates the axis of the TBM at geophone 17. It is more difficult to pinpoint the exact position of the apex of the hyperbola. It appears that the left side of the hyperbola has undergone a time shift with respect to the right side around geophone 15. As the TBM has a diameter of 8.3 m this shift appears near the east wall of the tunnel tube. This indicates that the sound is unlikely to be coming from the top of the TBM. The time shift might be caused by a source that is not located on the axis or by a distributed source.

During a recording of 2 s, about eight events arrive at a particular geophone. Comparison of these events will give information about the possible distribution of the source. If the source is moving, or if there are different sources in the TBM that emit waves separately, the signals will not necessarily look the same. A single located

source, on the other hand, will most probably generate the same signal every time.

In Figure 3.2, this is investigated for a recording by one geophone. The first trace of this figure shows the entire 2 s of the measurement. The arrival at approximately 100 ms is considered. A positive time shift is then applied to the trace to bring the arrival registered at approximately 300 ms to the same time instant as the first pulse. This time shift is calculated by means of autocorrelation. The trace is muted for negative times and zeros are added at the end until 2 s. The second trace in Figure 3.2 shows the result of this operation. The same procedure is performed for all subsequent arrivals in the recording. Traces 2 to 8 are the shifted versions of trace 1. It is clear that the 150 ms of each shifted trace are very similar, especially the pulses themselves. Therefore, it can be assumed that the source is at a fixed position.

By stacking these eight traces, the signal itself is amplified. All the arrivals on later times are suppressed. The stacked result is shown as the last trace in Figure 3.2. Here the source signal can be clearly distinguished from the surrounding noise. From this figure, the irregular period of the signal generation can again be seen. If the period was constant, not only would the first pulses of each trace line up, but so would the later arrivals. All these pulses would be visible in the stacked trace,

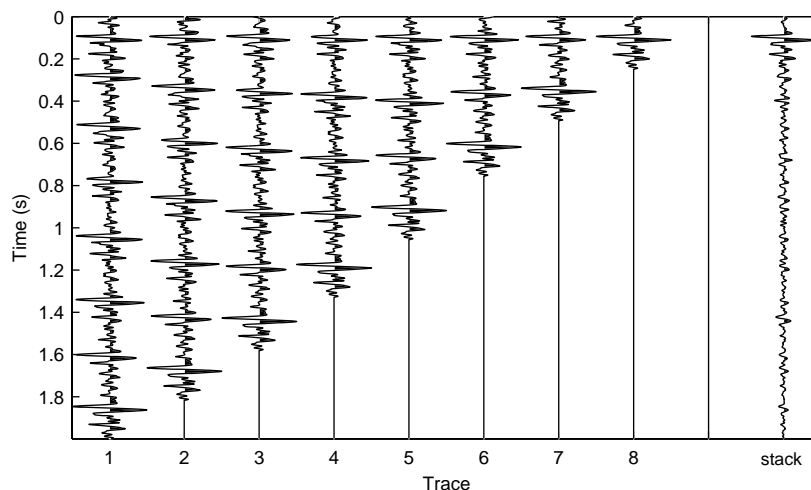


**Figure 3.2:** (1-8) Time-shifted trace to line up the pulses, stacked to give the source signal recorded at the surface

although with decreasing amplitude in time. However, only the first pulses are perfectly added and the other pulses are spread over the stacked trace as noise.

### 3.2 Determination of the source

The most important problem is determining which element of the TBM acts as the seismic source. Its position along the axis of the TBM is known approximately. However, its location along the circumference of the TBM is unknown. Engineers on site suggested that a possible source of the recorded signals could be the hydraulic jacks at the end of the TBM. These jacks are indicated in the profile of the TBM in Figure 3.3a. The hydraulic jacks push the TBM forward against the lining of the tunnel behind the machine while excavation is in progress. There are seven groups of hydraulic jacks, equally spread over the circumference of the shield. Each group consists of two pairs of jacks. Figure 3.3b shows a picture of one hydraulic jack pair. On the left side of this picture, a part of the tunnel ring that was last put in position is visible. The feet of the jacks are placed onto this ring. When the jacks are extended, the TBM is pushed forward. After the length of one ring is bored, the jacks are relaxed and the next ring installed. Since the TBM itself is 8 m long, the location of these jacks is in accordance with the position of the source as determined in Figure 3.1. The different jack pairs and their position inside the TBM would explain the results in Figure 3.1b, indicating a distributed source. Earlier

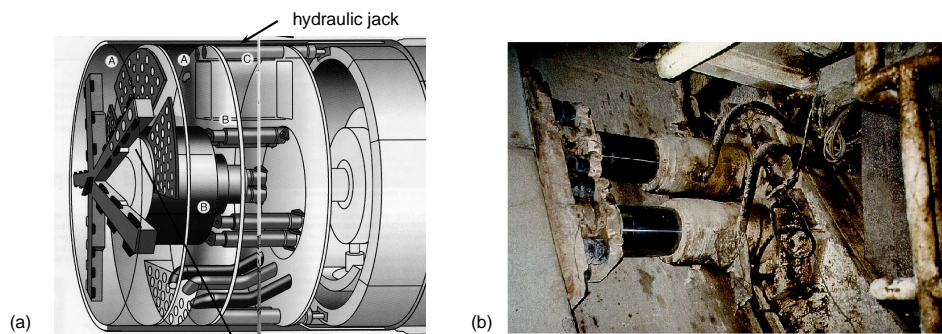


**Figure 3.3:** Schematic profile of the TBM (a), detailed picture of hydraulic jacks inside the Second Heineoord Tunnel (b)

vibration measurements carried out by Fugro Ingenieursbureau BV show periodic signals emitted by the jacks. To investigate these findings, new experiments were set up. The detailed description is given in Appendix B.

Three-component geophones were attached to four of the hydraulic jacks, the horizontal components parallel and perpendicular to the axis of the tunnel. If the jacks are the source, these geophones will directly register the source signal. Figure 3.4 shows a representative measurement on two jacks, made during excavating. The jack in Figure 3.4a is located on the west wall of the TBM, the one in Figure 3.4b is located on the east wall. The plots show the horizontal component parallel to the jack (trace 1), the horizontal component perpendicular to the jack (trace 2), and the vertical component (trace 3).

The horizontal component parallel to the jacks shows clear, distinct signal bursts. Pulses are also present in the other two components, but they are much less distinct and are hidden in other events and noise. This is in accordance with the energy distribution of the earlier measurements made at the earth surface as seen in Fig-

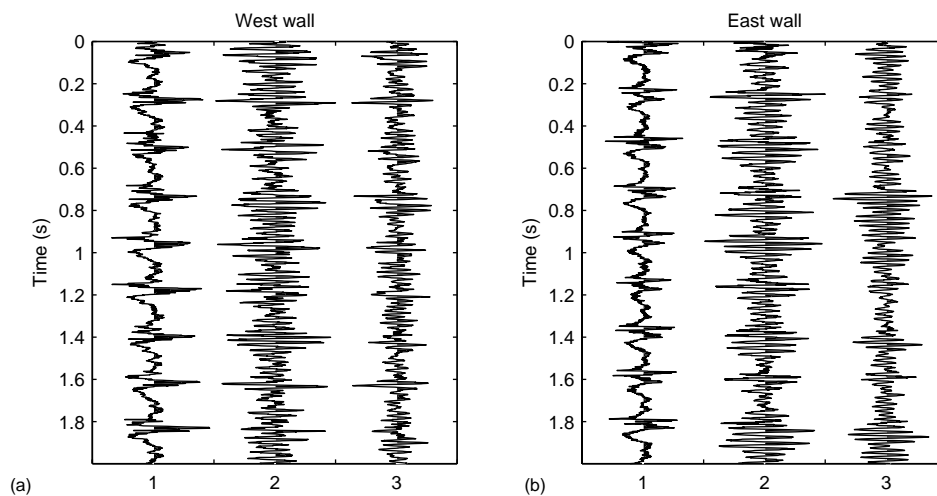


**Figure 3.4:** Three components of the signals recorded on hydraulic jacks on the West wall (a) and on the East wall (b), horizontal component parallel to the jack (1), horizontal component perpendicular to the jack (2), vertical component (3)

ures 2.1 and 2.2. Therefore, this horizontal component parallel to the jack will be considered in future analysis.

All traces in Figure 3.4 are measured simultaneously. The arrival times of the pulses are the same, but the signature of the signals shows a difference. For this measurement, the jacks on the west wall generate a single pulse. However, the energy emitted by the jacks on the east wall seems divided over two smaller pulses. This is probably influenced by the mechanism that generates the signals, which will be discussed later in this chapter.

To confirm whether there is a relationship between the signals that are generated by the hydraulic jacks and those discussed in Chapter 2, the signals on the jacks have to be linked with the measurements made simultaneously at the earth surface. In Figure 3.5 a recording of the horizontal in-line component on a geophone line located on the earth surface is plotted. The geophones at the earth surface are put on a cross-line compared with the axis of the TBM. Their spatial distance is not constant. The exact set-up is explained in Appendix B. The recordings at the earth surface again contain the hyperbolas that indicate the presence of the source. They show correlation with pulses that are registered on the hydraulic jacks during the same measurement.

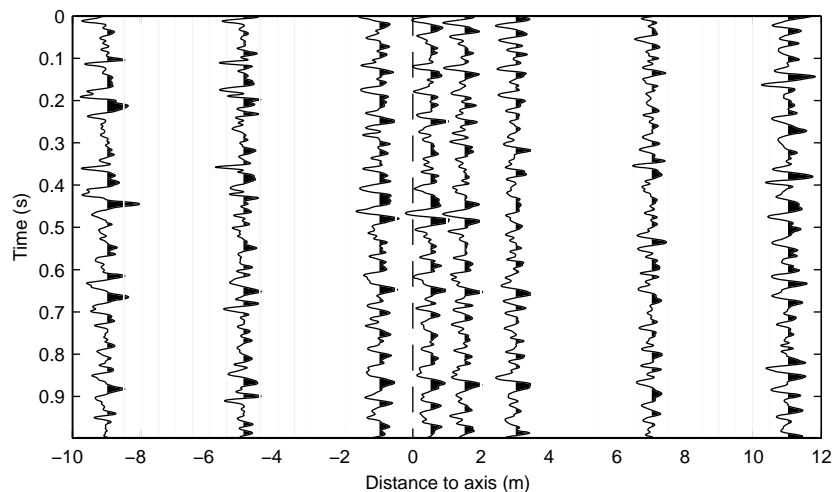


*Figure 3.5: Horizontal in-line component of the signal recorded by a geophone line on the surface*

Although there is strong evidence that the jacks are the seismic source, the influence of other mechanical instruments inside the TBM was also investigated. Separate 3-component geophones were attached to several elements of the machine. They were all installed in the same direction for easy comparison of the recordings. One geophone was tied to the axis that controls the cutter wheel. A second geophone was tied to a hydraulic engine. Both machine elements are located in the front of the TBM. Based on their position, these elements can already be excluded as the source because this does not agree with the location of the source as determined in Figure 3.1. Two more geophones were put on the U-profiles that are fixed to the shield of the TBM, one on the west wall and the other on the east wall of the TBM. Their lateral position is similar to that of the hydraulic jacks.

In Figure 3.6, the signals measured on these mechanical elements can be compared. As explained previously, only the horizontal components parallel to the jacks are considered here. They are all plotted on the same amplitude scale. The first two traces repeat the measurements on the hydraulic jacks from Figure 3.4. In addition, the simultaneous recordings on the axis, the hydraulic engine and the U-profiles are plotted.

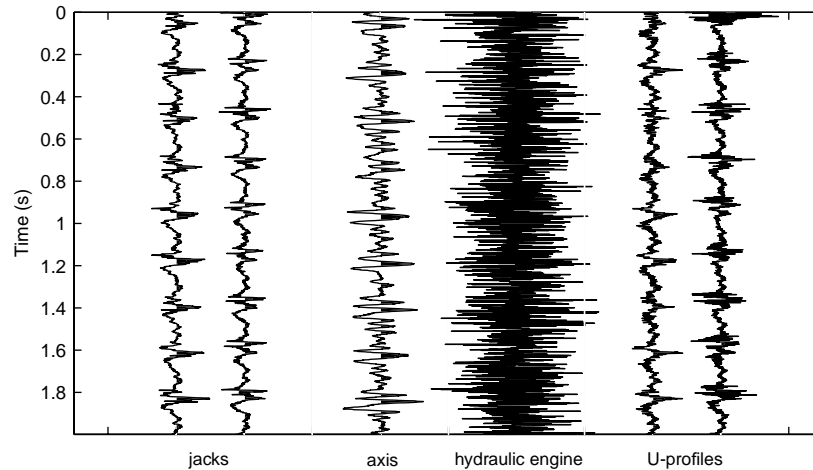


**Figure 3.6:** Horizontal component parallel to the jacks of signals recorded inside the TBM on two hydraulic jacks, on the axis of the cutter wheel, on the hydraulic engine and on two U-profiles

The pulses generated by the jacks can be traced back in the recordings from the other geophones. The trace recorded on the axis of the TBM still clearly shows the signals, although the pulses have been smoothed by the time they reach the axis. The measurement also contains more noise. The hydraulic engine only appears to generate noise. The signal coming from the jacks is present in the data, but extensive filtering is needed to make it visible. The pulses are most obvious, and with the least deformation, in the recordings on the U-profiles. They are clearly related to the signals generated by the jacks. The signal-to-noise ratio is the highest in the measurements on their neighbouring hydraulic jacks. The dependency between the signals registered on the U-profile and those on the hydraulic jacks is discussed later in this chapter.

### **3.3 Cause of the shear waves**

The shear waves are recorded most distinctly and strongly on the hydraulic jacks. For the source to be controllable, it is important to know the cause of the signals. The hydraulic jacks are mechanical elements of the TBM that are constructed out of several mechanical and electrical parts. They are also connected to several other elements of the TBM. These can all contribute in some way to the generation of the seismic signals. Several possibilities are investigated thoroughly.

#### **3.3.1 Engines and pumps**

A number of recordings were made with geophones inside the TBM to test the possible effects of various pumps and engines on the measurements on the hydraulic jacks. Periodicity of the seismic signals is a typical property of engines or pumps. The tests were done during an idle period of the TBM to avoid disturbance to the drilling process. The machines were activated separately for a few seconds to register their seismic energy. None of them shows a clear effect on the recordings on the hydraulic jacks.

### 3.3.2 The measuring equipment

During excavation, the hydraulic jacks push the TBM forward. The jacks are extended proportionally to the progress of the machine. A Temposonics measuring system, the Temposonics II Linear Displacement Transducer constructed by MTS Sensor Technology [Sensor Technology GmbH & Co. KG, 1994], was installed in every jack. This system determines the incident length of the jack each second. The Temposonics II position sensor measures the time interval between an interrogating pulse and a return ultrasonic pulse on a magnetostrictive wave-guide system. This determines the position of a movable magnet that passes along the outside of the sensor tube. In the case of the hydraulic jacks, the magnet is at a fixed position, while the tube passes through it when the jack is moving, thus determining the length of the jack.

The company, MTS Sensor Technology, was contacted to discuss the possibility of this system being the source of seismic shear waves. Its engineers were convinced that the operation of the Temposonics II could not generate these kinds of signals.

### 3.3.3 Friction effects

The tests on the mechanical parts of the TBM in the previous section confirm the seismic source to be the hydraulic jacks. Figure 3.6 also shows a large resemblance between the signals measured on the jacks and those on the U-profiles. To investigate them more thoroughly, the traces are replotted in Figure 3.7. Figure 3.7a shows the recordings on the west wall of the TBM, while those in Figure 3.7b are made on the east wall. The wavelets look very similar for measurements on the same side of the TBM. The amplitudes of the signals are in the same range. The signal-to-noise ratio for the signals on the hydraulic jacks is much better. It can be concluded that the signals recorded on the hydraulic jacks and on the U-profile have the same source. The attenuation between both elements is negligible, since the distance between them is very small and they are firmly coupled.

The U-profiles are solidly attached to the shield of the TBM. This suggests interaction between the hydraulic jacks and the shield that is in direct contact with the soil around the TBM. To gain more insight into this interaction, the traces in Figure 3.7a are processed in more detail. Figure 3.8a, shows a small time window ranging from 236 ms to 360 ms. There is ample noise in the data. To suppress this noise, a high-cut filter is applied. The smoothed result for the same time window is plotted in Figure 3.8b.

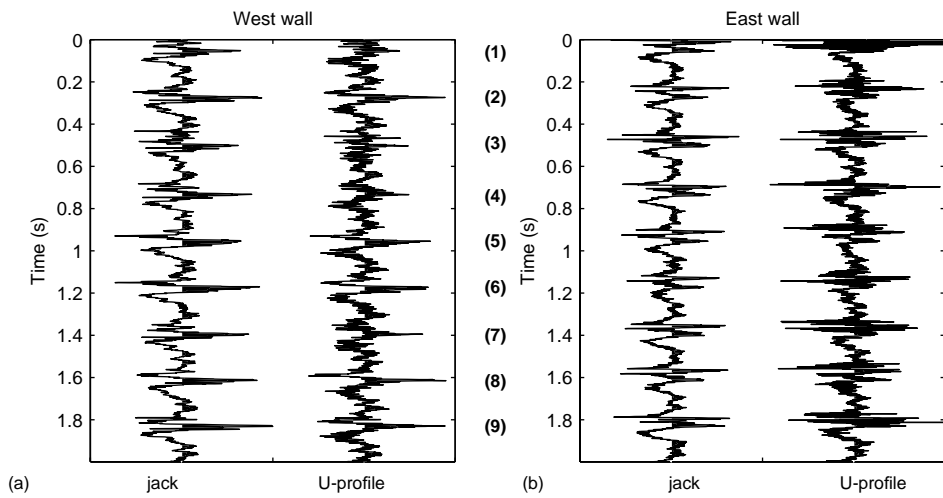


**Figure 3.7:** Horizontal component parallel to the jacks of the signal recorded on an hydraulic jack and on a U-profile on the West wall (a) and on the East wall (b)

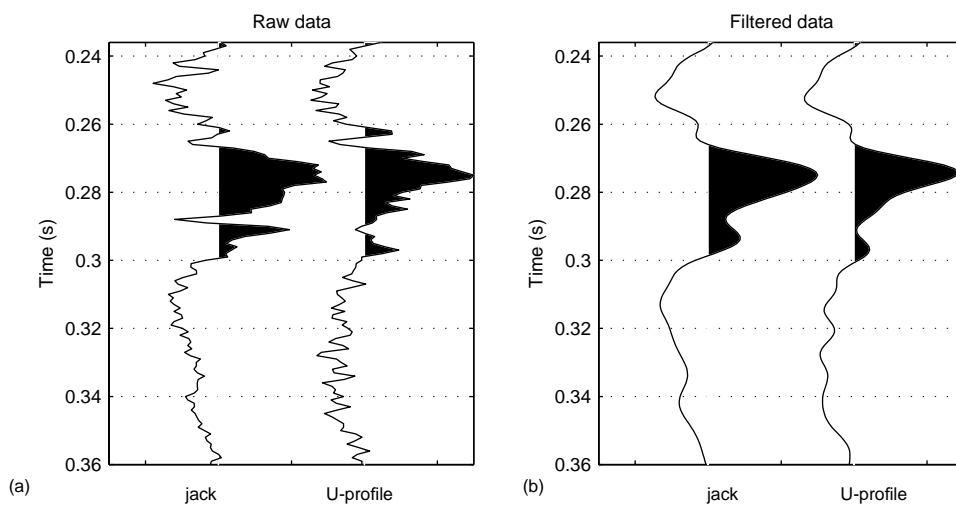


**Figure 3.8:** Time window 2 (Figure 3.7) of the horizontal component parallel to the jacks of signal recorded on an hydraulic jack and on a U-profile on the West wall, raw data (a), after applying a high-cut filter (b)

In a similar way, the data in Figure 3.7a are divided into nine small time-windows around the different pulses. The numbers 1 to 9 indicate the intervals. The exact intervals are listed in Table 3.1. For both the raw data and the filtered data, the cross-correlation between the signal at the U-profile and the signal at the jack in each time-window is calculated. From this, the difference in arrival time between both signals can be determined. The results are set out in Table 3.1.

Pulse	Interval	Time difference Raw data	Time difference Filtered data
1	1 - 120 ms	+1 ms	+0 ms
2	236 - 360 ms	+1 ms	+1 ms
3	471 - 560 ms	+0 ms	+0 ms
4	661 - 800 ms	+0 ms	+2 ms
5	921 - 1040 ms	+0 ms	+0 ms
6	1141 - 1240 ms	+0 ms	+0 ms
7	1372 - 1450 ms	+1 ms	+2 ms
8	1576 - 1700 ms	+1 ms	+1 ms
9	1801 - 1910 ms	+1 ms	+1 ms

**Table 3.1:** Time differences between signals recorded at the hydraulic jacks and the U-profiles on the west wall, calculated from the cross-correlation of small time windows in the raw and the filtered data

The calculated time differences for the raw data and the filtered data are not always the same. This is a consequence of inaccuracies introduced by under-sampling and by noise in the raw data on one hand, and by smoothing of the filtered data on the other hand. An important observation is that the trend of the results is the same for both data sets. All signals show a small positive time difference. A positive time difference indicates an earlier arrival of the signals on the jack than on the U-profile. For certain intervals, the signals at the jack and the U-profile appear to coincide. For other intervals, the signal at the jack is recorded 1 ms earlier, or even 2 ms earlier in the case of the filtered data. Existence of a constant time difference between the two measurements is uncertain. It is possible that there is a constant interval smaller than 1 ms that cannot be defined correctly because of the low sample rate and other inaccuracies. Most importantly, it can be concluded that the signals at the U-profile are never registered earlier than those at the hydraulic jack. This is logical since the signals are generated at the hydraulic jacks.

The similarity of the signals recorded on the hydraulic jacks and the U-profiles, and the positive time differences, indicate an interaction between the hydraulic jacks and the shield to which the U-profiles are solidly attached. The jacks are responsible for the progress of the TBM through the subsurface. The machine does not slide forward smoothly at a constant rate. When the machine is forced through the ground, friction develops between the shield and the soil surrounding it, thus holding back the TBM. The friction increases until a critical value is reached. Then, the TBM slides forward and friction starts building up again. The critical value depends on the soil type. It is larger for clay than for sand, and even larger for peat. This cycle is controlled by a feedback system between the movement of the shield and the force of the hydraulic jacks. It is assumed that the generation of seismic shear waves is caused by this soil-dependent progressing mechanism. Therefore, this mechanism will also influence the amplitude and the periodicity of the generated shear waves. This explains the variation in the measurements at different positions along the tunnel axis. The TBM will move more smoothly through sand than through clay. Often the TBM will not be surrounded by only one single soil type, based on the thickness of the geological layers and the presence of soil lenses such as peat. The variety of soil types also explains the difference in signature on opposite walls of the TBM and why pulses in the measurements are sometimes less distinct.

To understand completely the mechanism that generates the shear waves, further investigation is required. From the present observations, it appears to be difficult to control the source mechanism, which is necessary if it is to be used for imaging in front of the TBM. To interpret measurements, full knowledge of the source is necessary. Installing a controllable source on the TBM could solve this. The advantage of an active source is that its properties can be set so that they are optimal for the application. In this case, it is still important to know as much as possible about the seismic energy that is being generated by the TBM. The active source should have properties that clearly differ from those of the TBM source, to enable both waves in the data to be distinguished easily and to filter out the unwanted TBM energy. In addition, Falk [1998] has shown, in experiments with an active source on a TBM at Duisburg-Meinderich, that the interfering signals were richer in energy than the active signals by more than an order of magnitude. Interfering signals comprise electric service voltages and mechanical background noise from pumps and engines. Therefore, a study of all energy sources on and around the TBM is necessary for developing a source that will image the subsurface in front of the TBM.

## Imaging around the TBM

---

*The earth surface measurements shown in the previous chapters only show the direct waves. Reflections from heterogeneities and boundaries of geological layers that are present in the data, are not visible in the figures because their energy content is much smaller. Further processing of the data is necessary. However, in most tunnelling projects, it is inefficient to put geophone lines at the earth surface. It would not be cost effective to perform these kinds of measurements for a tunnel several kilometres long. Furthermore, it is not always possible to set up a survey at the earth surface. It would be more convenient if receivers could be installed on the TBM itself. Different experiments are described in this chapter. They all aim to test the usefulness of the hydraulic jacks as a seismic source from a different approach. Both the source signal and the source position are evaluated.*

The main purpose of this thesis is to investigate possibilities to image the subsurface right in front of the TBM and to detect heterogeneities. This section focusses on the application of shear waves in a reflection mode.

In all measurements, a good position of source and receivers is decisive. While the source in these experiments (the hydraulic jacks) is fixed, the position of the receivers can be influenced. It would be best to install them on the head of the TBM, at the bore front, so that all reflections initiating in front of the machine are registered. The seismic penetrability of the bentonite at the bore front is a crucial for the succes of such a configuration. For the first experiments, external sources are used to exclude any uncontrollable effects from a passive source like the TBM.

Secondly, the performance of the hydraulic jacks as reflection source is tested. Geophones are installed inside the tunnel, behind the TBM. In this situation, the problems introduced by the bentonite slurry are not present, and only the usefulness of the source itself can be investigated.

## 4.1 Imaging in front of the TBM using external sources

### 4.1.1 Experiments

The experiments in this section were performed in combination with the measurements of Chapter 3. The set-up is also described in detail in Appendix B. The optimal position of the receivers for imaging in front of the TBM would be the cutter wheel itself or the diaphragm. The diaphragm is situated approximately 1 m behind the cutter wheel. It separates the internal part and the external part of the TBM at the bore front. The cutter wheel is the closest to the soil. The ever-changing geometry of the bore front owing to the rotation of the cutter wheel makes analysis of the data more difficult. On the other hand, this rotation creates many more spatial receiver positions in the plane of the cutter wheel with only a small number of receivers actually installed. The available space on the cutter wheel is limited, and it is further restricted because installation of several other instruments for controlling the excavation process is necessary. The changing geometry is not present at the diaphragm, which has a much larger available surface. However, the rotation of the cutter wheel disturbs registration on the diaphragm if the rotating arms intercept the waves. These issues of rotation of the receivers and irregular data acquisition can be taken into account during processing of the data to produce a reliable image of the subsurface.

A more important problem could be caused by the bentonite. To keep the bore front stable during drilling, bentonite slurry is pumped into the chamber in front of the diaphragm. The pressure and composition of this slurry are adjusted depending on the soil properties at the bore front. A small layer of this slurry builds up between the cutter wheel and the soil, and forms a cake. The slurry pressure is applied to this cake and prevents the soil from collapsing. When the cutter wheel turns, the cutter teeth scrape the cake locally. The pressure on the ground water changes and causes the bentonite to repair the slurry cake. This is a continuous process. It is only during idle periods of the TBM that the cake has time to rebuild completely [Peters and Plekkenpol, 1997]. To reach receivers at either the cutter wheel or the diaphragm, seismic waves have to travel through the slurry. In theory, shear waves do not propagate in fluids. For shear waves that are emitted by the hydraulic jacks to reach receivers at the bore front, a direct contact between the soil and the receivers should exist. The bentonite is a viscous, thixotropic mud slurry. When agitated, it will behave as a fluid, but will become a gelled, more solid structure over time when not subject to shearing. It might be possible for shear waves to travel through this slurry, more probably when the TBM is not active. However,

if they do, they will be extinguished rather quickly. At the cutter wheel, the slurry cake is not very thick, so enough energy might still be present to be registered by the receivers. Shear waves can also be converted into compressional waves at points of transition between solids and fluids. The compressional waves would propagate into the bentonite slurry and reach the receivers on the TBM. Both seismic waves induce pressure changes in the subsurface. If any seismic energy is left, it should be noticeable on the recordings of the pressure sensors. On the cutter wheel and the diaphragm, pressure sensors are installed to monitor the soil pressure at the bore front every second. Changes indicate a change of the soil properties to which the bentonite composition should be adjusted. The registration system of one pressure sensor at the cutter wheel was temporarily adapted to measure at a higher frequency of 400 Hz, necessary for seismic applications (Appendix B). Five pressure sensors on the diaphragm were connected to the seismic recording system during the time of the experiments. The results will give an impression of the ability of shear waves to travel through the bentonite slurry, or to be converted into compressional waves.

The hydraulic jacks, which are considered the seismic source, are located at the end of the TBM. To be used for imaging in front of the TBM, the signals have to pass around the shield of the machine. This leads to an area close to the cutter wheel that will be hard to image, a so-called blind zone. To test the extension of this zone, 3-component geophones were buried at the depth of the TBM, some right on its trajectory (Appendix B). With these geophones, the signals generated by the TBM can be registered directly in front of the machine. Since the distance between the TBM and the geophones decreases, an indication of the damping of the source signals, and thus a range for imaging in front of the TBM, will be given. These geophones were positioned below the 3-component geophones that are located at the earth surface and that were also used as described in Chapter 3.

Because the signals have to pass round the shield, it is possible that the pressure sensors do not record the waves coming from the TBM, although the bentonite slurry does transfer shear waves. The signals could have become too weak by the time they reach the slurry cake. To exclude this possibility, active shear and compressional sources were triggered during an idle period of the TBM. Appendix B shows the source positions. A shear wave vibrator sent shear waves into the subsurface. Explosives generated compressional waves. Even if the conversion of shear to compressional energy at the point of transition between the soil and the bentonite is limited, it should still be possible to record the compressional waves

generated by the explosives with the pressure sensors on the TBM. To combine all source and receiver equipment into one single system with one trigger would be too complicated at this stage. Therefore, explosives were also detonated for the synchronization of the combined data set.

#### 4.1.2 Results

The ability of seismic waves to travel through the bentonite slurry is the most important issue in these experiments. Shear waves cannot propagate through non-viscous fluids. Even if the waves penetrate the slurry, they will be greatly attenuated, or possibly extinguished, before they reach the cutter wheel. The recordings of the pressure sensors have to indicate whether the shear waves generated by the hydraulic jacks can reach the cutter wheel or the diaphragm. The pressure sensors at the cutter wheel are only a few centimetres from the soil, while for the diaphragm, a distance of approximately 1 m has to be crossed.

It was expected that the pressure pulse from the explosives would be recognized on the recordings of the pressure sensors. Unfortunately, this signal could not be detected above the noise level. It is not registered either by the pressure sensor at the cutter wheel or by those at the diaphragm. This is rather unexpected since the blast from the explosives has a high energy content.

On simultaneous recordings by 3-component geophones at the earth surface, the explosion is clearly visible. On the measurements by the 3-component geophones at depth, the signal is less distinct. The compressional energy can be recognized, but there is a low signal-to-noise ratio. It appears that the waves have been greatly attenuated in the soft soil. Therefore, it is difficult to draw conclusions about the penetration of seismic energy in the bentonite slurry. Furthermore, it is possible that the pressure sensors installed on the TBM are simply not suited for these kinds of seismic applications. However, if the bentonite is responsible for the results, special hardware adjustments are necessary to ensure that there is direct coupling between the receivers at the TBM and the non-excavated soil. This coupling would improve the registration of seismic waves at the head of the TBM. Obviously, these results hold when using a slurry shield TBM. Another type of TBM uses an earth-pressure-balance shield to sustain a stable bore front. It is possible that shear waves do propagate through the bentonite, but are not able to travel through the foam that is used in these tunnelling machines. In this case, direct coupling is a crucial factor in the imaging process.

## 4.2 Imaging around the TBM using shear waves emitted by the jacks

### 4.2.1 Experiments

The Second Heinenoord Tunnel consists of two tunnel tubes, bored separately under the river Oude Maas. The west tube was excavated first, from north to south. The TBM was then turned around and put in position for excavation of the east tunnel tube. In the middle of the tunnel, the tubes are at the greatest distance from each other, equal to the tunnel diameter of 8.3 m. The experiments described in this section were performed inside the east tunnel tube of the Second Heinenoord Tunnel. Embedded in the soft soil, the concrete lining of the other tube serves as a perfect reflector. Its known position makes the experiments reliable and controllable. The hydraulic jacks emit the source signal during excavation of the east tunnel tube. The receivers are 1-component geophones attached in the lining of the west wall behind the TBM. They are fixed horizontally with their polarization parallel to the main energy component of the source signal. The receivers are on a horizontal line with a 3 m spacing (irregularities because of practical problems inside the tunnel are taken into account during processing). A top view of this experiment can be seen in Figure 4.1. A detailed description of the position of the geophones and the way they are attached to the lining is given in Appendix C. For synchronization with the source signal, geophones were again put on the hydraulic jacks.

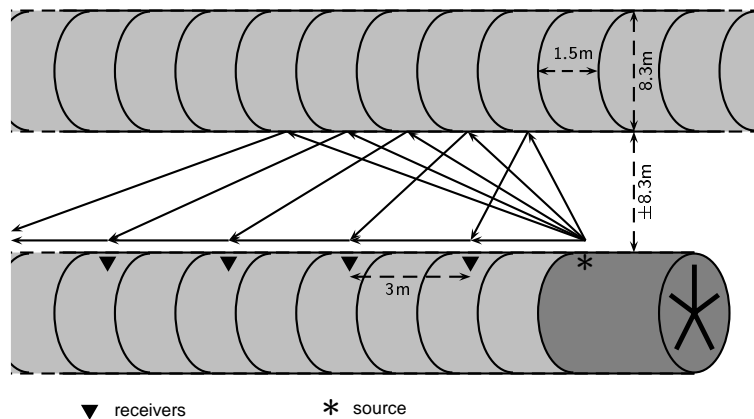


Figure 4.1: Topview of the tunnel tubes with source and receiver positions

These experiments are comparable with seismics-while-drilling measurements that are performed in vertical bore holes for oil production [Rector and Marion, 1991]. In that case, the sound generated by the drill bit is used as a seismic source for imaging deeper into the earth and into the surroundings of the bore hole. In similar measurements, the geophones are placed down a second vertical bore hole to image the subsurface between the bore holes. In horizontal hard rock tunnels, Petronio et al. [2000] used the noise generated by the drill bits of the TBM as a seismic source for seismics-while-drilling measurements. Ashida et al. [2002] shows similar experiments in hard rock. Both the tunnel blasting and the TBM are used as seismic sources and recordings are made by 3-component geophones on the tunnel walls.

#### 4.2.2 Results

Apart from some noise, two main forms of seismic energy will be registered by the geophones in the east tube. They are both indicated in Figure 4.1. The strongest signals are the direct waves. These travel from the source in a straight line to the receivers. In this case, they propagate through the reinforced concrete tunnel lining. The shear wave velocity in the concrete is approximately 2200 m/s, which is much higher than that of the soft soil. The direct waves will arrive at the geophones before any other events. Compared with the soft soil, the concrete causes a much smaller attenuation of the energy. Combined with the fact that the direct waves have the shortest travel path, they will have the highest amplitude of all events present in the measurements. As a result of the constant velocity of the direct waves in the concrete and the fixed spacing of the geophones, these direct waves will appear in a time-distance  $(t, x)$  plot as linear events. Figure 4.2a is a clear example of their predominance. The irregularity of the amplitude and periodicity of the direct waves in Figure 4.2a gives an idea of the complexity of the source signals at the time of this measurement.

Because the direct waves are linear events, they can be removed from the data by simple processing. All these events have the same slope in the time-distance  $(t, x)$  domain. By applying a linear time shift to each trace, they become horizontal events. By stacking the traces a reference trace is created; the horizontal events adds up to a strong signal, while the rest of the energy in the data gets cancelled. For each data trace, the amplitude of the reference trace is scaled to minimise the energy difference with the data trace. The scaled reference trace is then subtracted from the

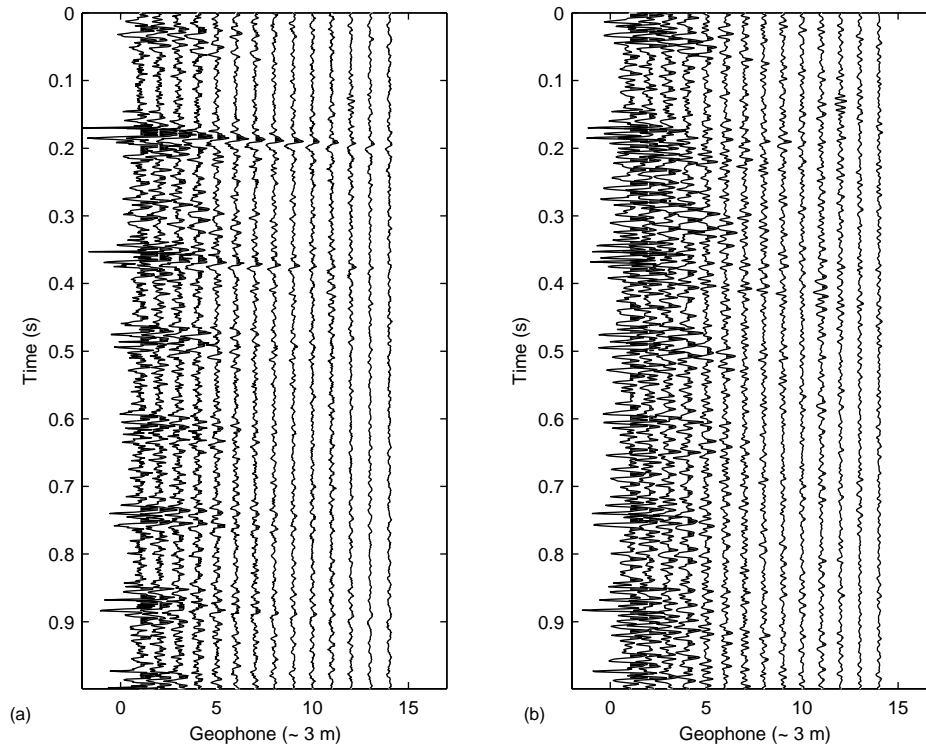


**Figure 4.2:** Raw data recorded on the West wall of the East tube showing the linear direct arrivals of the signals emitted by the hydraulic jacks (a), data after removal of direct waves, showing reflections and refractions of the energy in the soft soil (b)

data trace, thus removing the energy in the horizontal events. After applying the reverse time shift, the original data without the direct energy is obtained. The result is plotted in Figure 4.2b. Some direct energy still remains, mainly in the first traces. But the reflections and refractions of the waves around the tunnel are better visible in the filtered data set. The data in Figure 4.2b is plotted with a high amplitude scaling factor, the high attenuation of the soft soil causes these events to be much weaker than the direct waves. The reflections have a completely different slope to the direct waves in Figure 4.2a. The waves have travelled much slower, with velocities ranging between 200 and 400 m/s. This is higher than the average soft soil velocity of 150 m/s that was measured in chapter 2. The waves recorded at the surface travelled directly from the TBM to the receivers. However, the subsurface between the tunnels is much more complicated and compacted. Grout surrounds the tunnel elements. Back-grouting at the tail side of the TBM has to prevent soil

subsidence around the tunnel ([Bakker et al., 1996]). Directly after injection, the grout is still liquid, and it hardens with time. The penetration of the grout into the soil depends on the soil type and the grouting procedure. Both of these aspects will influence the behaviour of the seismic waves. Apart from the grout, the energy will have to travel through the 20 cm thick tunnel wall before it reaches the receivers installed on the inside of the tunnel. This explains the high wave speed of the recorded reflections.

In addition to the reflections of the east tunnel tube, the data set in Figure 4.2b also contains noise or multiple energy. Multiples have been reflected by the west tube back to the east tube. The concrete lining of the east tube is an almost perfect reflector, and part of the energy will be bounced back into the soil towards the west tube. Multiples will have travelled several times between both tubes before being registered by the geophones. Because of their longer propagation in the soft soil, they will be weaker by the time they are recorded. In order to show that the main events in Figure 4.2b are reflections from the other tunnel tube and to demonstrate the influence of the multiples on the data, a simplified 2D model of the situation is made. A sketch is shown in Figure 4.3a. The top and bottom layers represent the two tunnel walls, with a wave speed of 2200 m/s and at a distance of 8.3 m. To include the influence of the grout, these layers are extended both over 20 cm. In the middle layer, the wave speed is set at 200 m/s. A seismic source is located on the tunnel boundary. The receivers are at the inside of the tunnel wall, therefore they are 20 cm from the boundary in the model. The receivers have a spacing of 3 m, with the first receiver situated at a distance of 10 m from the source. As a source, a Ricker wavelet with a centre frequency of 80 Hz is used. This is the strongest frequency in Figure 4.2b. The source is triggered only once, as opposed to the hydraulic jacks, which are a continuous source. The result of the modelling is plotted in Figure 4.3b. The direct wave is removed from the data, only the direct reflection and its multiples are shown. Real data will contain more multiples than the simplified model because of the complexity of the soil and grout in between the tunnels.

In Figure 4.3c, a 3 s time frame from Figure 4.2b is plotted. To make the reflections more visible at higher distances from the source, the data is not plotted with true amplitude but each trace is scaled to its maximal amplitude. In the modelled data set, energy further from the source is stronger than in the measured data set because no damping factor is included in the model. Of course the trace scaling also makes the noise appear stronger. The event indicated by the arrows in Figure 4.3c shows the same behaviour as the main reflection in Figure 4.3b. This similarity indicates that real data contains reflections from the east tunnel tube. The multiples that are

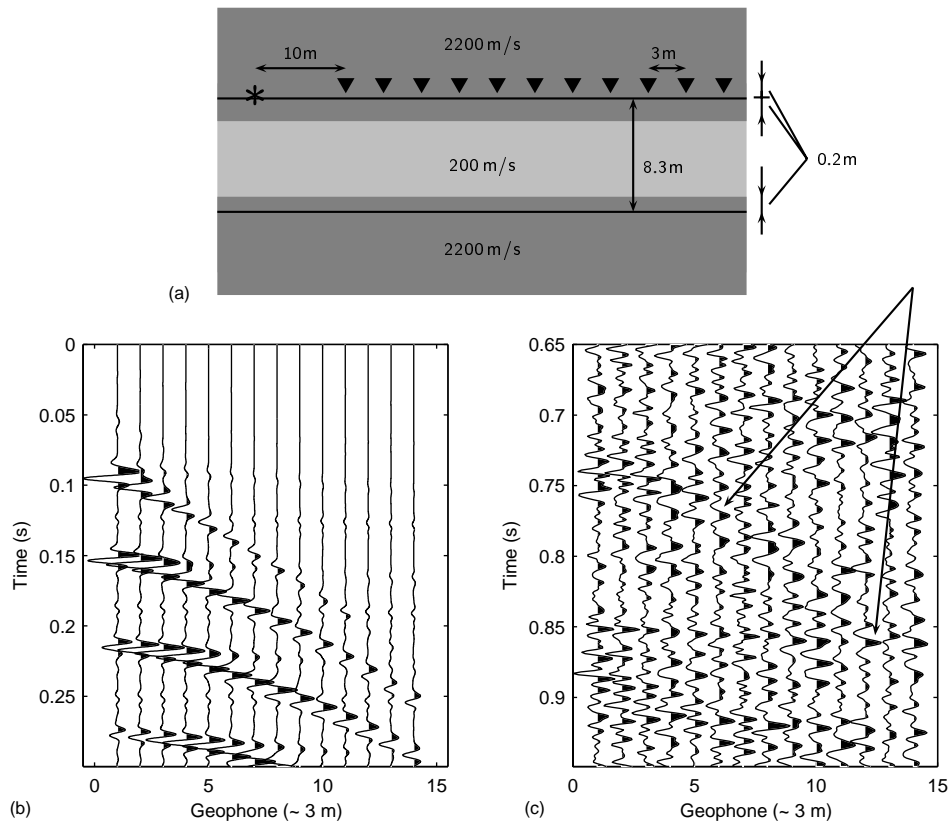


**Figure 4.3:** Sketch of model (a) for modelled data set with source and receivers on tunnel wall showing reflections and multiples (b), zoomed view of filtered data recorded on the West wall of the East tunnel tube (c)

clearly present in the modelled data are weaker and hidden in the noise in the real data. However, they will influence the real data and consequently the processing.

Figure 4.2a, shows that the signals emitted by the hydraulic jacks at this point are not distinct and regular pulses. As pointed out in Chapter 3, the irregularity of the source is due to the soil type surrounding the TBM, which is rather heterogeneous in the area where the seismic experiments were performed. The data also have a high signal-to-noise ratio because of heterogeneities in the soil causing scattering of the waves. The properties of the recorded reflections are also influenced by the

grout that surrounds the tunnel elements. The modelling in Figure 4.3b shows the influence of the multiples. As a result, the direct waves and the reflections cannot always be unambiguously recognized in the data recorded on the tunnel lining, especially the reflections from the other tunnel tube are weak. These aspects make further analysis of the data difficult. The examples do give an indication that it is certainly worthwhile to do more research on the use of shear waves for reflection measurements in tunnelling. The hydraulic jacks are probably not the preferred source. Reflections from around the tunnel appeared only weakly in the recorded data, reflections in front of the tunnel will be even harder to register.

### 4.3 Passive vs. active seismic source

The analysis of the seismic energy generated by the TBM indicates that it is difficult to control the emission and properties of the signals. The reflection experiment shows how the data are influenced by several internal and external factors. There are still many uncertainties when using the TBM itself as a seismic source for imaging around the tunnel face. Implementing this as a reliable system would require more research to understand fully how the seismic signals are generated. When imaging ahead of the tunnel face, the position of the hydraulic jacks at the end of the TBM will require special attention in processing.

Installing an active source on the tunnelling machine can be used as an alternative to the TBM. This source could be designed with properties optimal for the local soil conditions. Also the properties of energy sources in and around the TBM could be taken into account in the design to make separation of the desired reflections during processing easier. The optimal position for such a source, and also for the receivers, is at the cutter wheel, because this part of the TBM is closest to the soil face. Seismic waves from transducers on the diaphragm would still be scattered by the rotating cutter wheel in front of it.

The installation of transducers on the cutter wheel will cause several practical problems. One of the main issues to be considered is the coupling between the transducers and the soil. As the soil is scraped by the teeth of the cutter wheel, there is always a small gap between the soil face and the blades of the cutter wheel where the transducers would be placed. For a Bentonite Slurry Shield, this gap is filled with viscous bentonite; for an Earth Pressure Balance Shield there is a soil-foam mix. In both cases, the filling is more liquid than solid. The measurements in chapter 4 have already shown that shear waves will not easily penetrate the bentonite.

The experiments with compressional waves did not give convincing results. To ensure reliable data, there should be close contact between the soil and the transducers. Therefore, the practical aspects of this system require more research, which falls outside the scope of this thesis.

When installing seismic sources and receivers on the head of the TBM, the design of the cutter wheel and the presence of other sensors constrain the possible configurations. It is not realistic to put a large number of transducers on the arms. The rotation of the wheel provides an advantage here. During the time of one complete rotation, the TBM has only moved forward a few centimetres, a small distance compared with the resolution of the shear waves in soft soil. This means that during one rotation, several measurements can be made and assumed to be taken at the same position of the TBM. Therefore, a large set of measurements can be made with only a limited number of receivers positioned at different distances from the axis. The relative position of the source and receivers does not change, but each recording will provide another illumination of the reflectors ahead of the TBM, thus providing new information to obtain a more complete image.

The progression of the TBM also creates the possibility of obtaining many images from the same reflectors. Measurements at different distances from an obstacle will all give a similar image. Combination of the information in these data sets will result in a more accurate definition of the obstacle the TBM will encounter.

In seismic surveys for oil and gas exploration, thousands of receivers are spread over a large area on the earth surface. In these tunnelling applications, the number of receivers and their aperture is restricted by the diameter of the TBM. Traditional data processing techniques, such as phaseshift migration, are optimized for a large number of data points. The special configuration on the head of a TBM requires adjustment of the existing processing methods. The next chapters of this thesis describe the theoretical aspects for the development of short extrapolation operators that are accurate and stable in a recursive migration scheme.



## WLSQ Optimization of Extrapolation Operators

---

*The data recorded on the head of a TBM has to be migrated to make an image of the investigated area of the subsurface in front of the tunnelling machine. The specific configuration of the measurements in these tunnelling applications, requires that the standard data migration techniques need to be improved. New asymmetric extrapolation operators, designed with a weighted least-squares approximation, will be developed to improve the migration results and give a more accurate image.*

### 5.1 Phaseshift extrapolation and imaging

A traditional imaging method in seismic data processing is phaseshift migration. This is a migration that is performed in the  $(\mathbf{k}, j\omega)$  domain, in which wavefield extrapolation is a simple multiplication. The equations for this type of migration for the set-up in tunnelling applications are derived in this section. They are based on the Kirchhoff integral.

#### 5.1.1 The Kirchhoff integral

The Kirchhoff integral can be obtained using Rayleigh's reciprocity theorem [Rayleigh, 1945, Fokkema and van den Berg, 1993]. A time-invariant, bounded domain  $\mathbb{D}$  in space is considered, in which two non-identical acoustic states  $A$  and  $B$  can occur. Each state is characterised by its acoustic wavefield with  $\hat{p}$ , the acoustic pressure, and  $\hat{v}_k$ , the particle velocity. The properties of the fluids in these states are

given by the volume density of mass  $\rho$  and the compressibility  $\kappa$ . Each state has its source distributions  $\hat{q}$ , the volume source density of injection rate, and  $\hat{f}_k$ , the volume source density of volume force. The reciprocity theorem describes the interaction between the two states.

$$\int_{\mathbf{x} \in \partial \mathbb{D}} \left( \hat{p}^A \hat{v}_k^B - \hat{p}^B \hat{v}_k^A \right) v_k dA = \int_{\mathbf{x} \in \mathbb{D}} \left[ j\omega(\rho^B - \rho^A) \hat{v}_k^A \hat{v}_k^B - j\omega(\kappa^B - \kappa^A) \hat{p}^A \hat{p}^B \right] dV + \int_{\mathbf{x} \in \mathbb{D}} \left( \hat{f}_k^A \hat{v}_k^B + \hat{q}^B \hat{p}^A - \hat{f}_k^B \hat{v}_k^A - \hat{q}^A \hat{p}^B \right) dV. \quad (5.1)$$

For the derivation of the Kirchhoff integral, state A represents the actual wavefield generated by a source located outside a bounded homogeneous domain  $\mathbb{D}$ . Inside  $\mathbb{D}$ , state A is source free. State B is generated by a point source of volume injection at  $\mathbf{x}'$  inside  $\mathbb{D}$ . Both states are listed in Table 5.1.

	State A	State B
Field State	$\{\hat{p}, \hat{v}_k\}(\mathbf{x}, j\omega)$	$\{\hat{p}^q, \hat{v}_k^q\}(\mathbf{x} \mathbf{x}', j\omega)$
Material State	$\{\rho, \kappa\}(\mathbf{x})$	$\{\rho, \kappa\}(\mathbf{x})$
Source State	$\{0, 0\}$	$\{\hat{q}^B(j\omega)\delta(\mathbf{x} - \mathbf{x}'), 0\}$

**Table 5.1:** States in Rayleigh's reciprocity theorem: Actual wavefield vs. volume injection Green's function

Applying the reciprocity theorem to the domain  $\mathbb{D}$ , results in

$$\int_{\mathbf{x} \in \partial \mathbb{D}} \left[ \hat{p}(\mathbf{x}, j\omega) \hat{v}_k^q(\mathbf{x}|\mathbf{x}', j\omega) - \hat{p}^q(\mathbf{x}|\mathbf{x}', j\omega) \hat{v}_k(\mathbf{x}, j\omega) \right] \nu_k dA = \hat{q}^B(j\omega) \hat{p}(\mathbf{x}', j\omega), \quad (5.2)$$

with  $\nu_k$  being the outward pointing normal on  $\partial \mathbb{D}$ . In order to obtain the incident wavefield, the Green's functions for the pressure and the particle velocity,  $\hat{G}^q$  resp.  $\hat{\Gamma}_k^q$  are used. They are defined as

$$\left\{ \hat{p}^q, \hat{v}_k^q \right\}(\mathbf{x}|\mathbf{x}', j\omega) = \hat{q}^B(j\omega) \left\{ \hat{G}^q, -\hat{\Gamma}_k^q \right\}(\mathbf{x}'|\mathbf{x}, j\omega). \quad (5.3)$$

The acoustic pressure in the observation point  $\mathbf{x}'$  becomes

$$\hat{p}(\mathbf{x}', j\omega) = \int_{\mathbf{x} \in \partial \mathbb{D}} \left[ -\hat{G}^q(\mathbf{x}'|\mathbf{x}, j\omega) \hat{v}_k(\mathbf{x}, j\omega) - \hat{p}(\mathbf{x}, j\omega) \hat{\Gamma}_k^q(\mathbf{x}'|\mathbf{x}, j\omega) \right] \nu_k dA. \quad (5.4)$$

The medium inside the domain  $\mathbb{D}$  is homogeneous. Therefore  $\hat{G}^q$  and  $\hat{\Gamma}_k^q$  can be replaced by the Green's function for a homogeneous medium  $\hat{G}$  [Fokkema and van den Berg, 1993], based on the following equations

$$\hat{G}^q(\mathbf{x}'|\mathbf{x}, j\omega) = j\omega\rho\hat{G}(\mathbf{x}'|\mathbf{x}, j\omega) \quad (5.5a)$$

$$\hat{\Gamma}_k^q(\mathbf{x}'|\mathbf{x}, j\omega) = \partial_k \hat{G}(\mathbf{x}'|\mathbf{x}, j\omega). \quad (5.5b)$$

This leads to the Kirchhoff integral:

$$\hat{p}(\mathbf{x}', j\omega) = \int_{\mathbf{x} \in \partial \mathbb{D}} \left[ -j\omega\rho\hat{G}(\mathbf{x}'|\mathbf{x}, j\omega) \hat{v}_k(\mathbf{x}, j\omega) - \hat{p}(\mathbf{x}, j\omega) \partial_k \hat{G}(\mathbf{x}'|\mathbf{x}, j\omega) \right] \nu_k dA. \quad (5.6)$$

The Kirchhoff integral expresses that if the pressure  $\hat{p}$  and the time derivative of the normal component of the particle velocity  $\hat{v}_k$  on a closed surface  $\partial \mathbb{D}$  are known, the pressure  $\hat{p}$  in every point inside  $\mathbb{D}$  can be determined. The Green's function  $\hat{G}$  describes the wavefield propagation from any point  $\mathbf{x}$  on the boundary  $\partial \mathbb{D}$  to the observation point  $\mathbf{x}'$ .

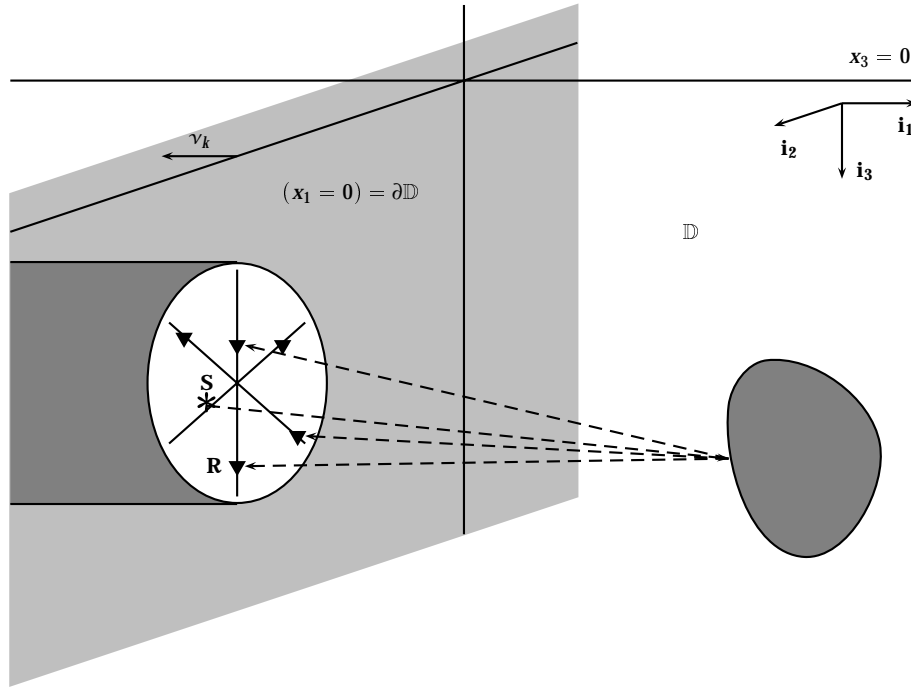


**Figure 5.1:** TBM configuration with source (S) and receivers (R) on the cutter wheel, to which the Kirchhoff integral should be applied

The Kirchhoff integral should be applied to the configuration used on the TBM which can be seen in Figure 5.1. The source and receivers are distributed over the different arms of the cutter wheel. During most of the trajectory of the TBM, it can be assumed that the cutter wheel is located in a vertical plane. For each measurement, this is considered to be the  $x_1 = 0$  plane. The domain  $\mathbb{D}$  in which the imaging takes place is the half sphere where  $x_1 > 0$ . When the radius of this half-sphere goes to infinity, the contribution of the Kirchhoff integral in Equation (5.6) vanishes due to causality and  $\partial\mathbb{D}$  can be limited to the plane  $x_1 = 0$ .

The boundary conditions for the half space of the Kirchhoff integral are implemented directly in the Green's function so that the background can be considered to be an unbounded homogeneous medium. In this case an image source with respect to the plane  $x_1 = 0$  should be considered. This results in the following Green's function

$$\hat{G}(\mathbf{x}'|\mathbf{x}, j\omega) = \frac{\exp(-\hat{\gamma}|\mathbf{x} - \mathbf{x}'|)}{4\pi|\mathbf{x} - \mathbf{x}'|} - \frac{\exp(-\hat{\gamma}|\mathbf{x} - \mathbf{x}^{g'}|)}{4\pi|\mathbf{x} - \mathbf{x}^{g'}|}, \quad (5.7)$$

with

$$\mathbf{x}^g = (-x'_1, x'_2, x'_3) \quad (5.8)$$

the mirror image point of the observation point  $\mathbf{x}'$  with respect to the plane  $x_1 = 0$  and

$$\hat{\gamma} = j\omega(\kappa\rho)^{\frac{1}{2}} = \frac{j\omega}{c}. \quad (5.9)$$

By using the half space Green's function, the first term of the Kirchhoff integral on the boundary vanishes. For the second term, the gradient of the Green's function has to be calculated on the plane  $x_1 = 0$ .

$$\partial_k \hat{G}(\mathbf{x}'|\mathbf{x}, j\omega) \nu_k \Big|_{x_1=0} = -\partial_1 \hat{G}(\mathbf{x}'|\mathbf{x}, j\omega) = -2\partial_1 \frac{\exp(-\hat{\gamma}|\mathbf{x} - \mathbf{x}'|)}{4\pi|\mathbf{x} - \mathbf{x}'|}. \quad (5.10)$$

Because  $x_1$  only appears in the combination  $(x_1 - x'_1)$ ,  $\partial_1$  can be replaced by  $-\partial'_1$ . This results in the following expression for the acoustic pressure  $\hat{p}$ :

$$\hat{p}(\mathbf{x}', j\omega) = -\frac{1}{2\pi} \partial'_1 \int_{x_1=0} \left[ \hat{p}(\mathbf{x}, j\omega) \frac{\exp(-\hat{\gamma}|\mathbf{x} - \mathbf{x}'|)}{|\mathbf{x} - \mathbf{x}'|} \right] dA. \quad (5.11)$$

This expression is called the Rayleigh II integral [Berkhout and Wapenaar, 1989]. It states that the acoustic pressure of the wavefield can be calculated in any point of the subsurface where  $x_1 > 0$  from the acoustic pressure  $\hat{p}(\mathbf{x}, j\omega)$ , recorded at a plane reference level  $x_1$ . If recordings at this level are made over an infinitely large plane, this Rayleigh II integral gives the exact solution. With a limited number of recording channels, approximation errors will be introduced into the calculations.

### 5.1.2 Forward wavefield extrapolator

The Rayleigh II integral equation can be rewritten as a two-dimensional convolution over  $x_2$  and  $x_3$  since the integral occurs in combination of  $\mathbf{x}$  and  $|\mathbf{x} - \mathbf{x}'|$  only. To indicate that it involves forward extrapolation of a wave propagating in the positive  $x_1$  direction,  $\hat{p}$  is replaced by  $\hat{p}^+$ , resulting in

$$\hat{p}^+(x'_1, x_2, x_3, j\omega) = -\hat{p}^+(0, x_2, x_3, j\omega) * \frac{1}{2\pi} \left( \partial'_1 \frac{\exp\left(-\hat{\gamma} \sqrt{(\Delta x_1)^2 + x_2^2 + x_3^2}\right)}{\sqrt{(\Delta x_1)^2 + x_2^2 + x_3^2}} \right) \Big|_{x_1=0}, \quad (5.12)$$

where  $\Delta x_1 = x'_1 - x_1$ . This equation calculates the forward propagation of the wavefield through the subsurface from the plane  $x_1 = 0$  to a plane  $x_1 = x'_1$ . The operator for the forward propagation is called  $\hat{W}$ :

$$\hat{W}(\Delta x_1, x_2, x_3, j\omega) = -\frac{1}{2\pi} \partial'_1 \frac{\exp\left(-\hat{\gamma} \sqrt{(\Delta x_1)^2 + x_2^2 + x_3^2}\right)}{\sqrt{(\Delta x_1)^2 + x_2^2 + x_3^2}}. \quad (5.13)$$

In the  $(x_1, k_2, k_3, j\omega)$  domain, this convolution turns into a simple multiplication. The operator for forward propagation thus becomes

$$\tilde{W}(\Delta x_1, k_2, k_3, j\omega) = \exp(-jk_1 \Delta x_1), \quad (5.14)$$

with

$$k_1 = \begin{cases} \sqrt{k^2 - (k_2^2 + k_3^2)} & k_2^2 + k_3^2 \leq k^2, \\ -j\sqrt{(k_2^2 + k_3^2) - k^2} & k_2^2 + k_3^2 > k^2, \end{cases} \quad (5.15)$$

and  $k = \omega/c$ . This operator is called the phaseshift operator [Gazdag, 1978] since the extrapolation of the wavefield only affects the phase of the wavefield in the  $(x_1, k_2, k_3, j\omega)$  domain for  $(k_2^2 + k_3^2) \leq k^2$ . Outside this range, the wavefield becomes evanescent. Forward wavefield extrapolation from a plane  $x_{1,i-1}$  to a subsequent plane  $x_{1,i}$  can be described by

$$\tilde{p}^+(x_{1,i}, k_2, k_3, j\omega) = \tilde{W}((x_{1,i} - x_{1,i-1}), k_2, k_3, j\omega) \tilde{p}^+(x_{1,i-1}, k_2, k_3, j\omega). \quad (5.16)$$

This expression can be applied in a recursive extrapolation scheme. If the wavefield is known at level  $x_{1,0}$ , the wavefield at every  $x_{1,i}$  level can be calculated from the result at the previous level. By choosing  $\Delta x_1 = x_{1,i} - x_{1,i-1}$  small enough, the background medium in each recursive step can be considered homogeneous over  $\Delta x_1$ .

### 5.1.3 Inverse wavefield extrapolator

The inverse extrapolation operator calculates the back propagation of the wavefield through the subsurface. It is determined by

$$\tilde{F}(\Delta x_1, k_2, k_3, j\omega) \tilde{W}(\Delta x_1, k_2, k_3, j\omega) = 1. \quad (5.17)$$

The amplitude of  $\tilde{F}$  is also constant for  $(k_2^2 + k_3^2 \leq k^2)$  but exponentially growing outside this range. This gives an unstable operator that can not be used in recursive schemes. In order to obtain a stable inverse operator, an approximation is made by taking the complex conjugate of the forward operator, i.e.:

$$\tilde{F}(\Delta x_1, k_2, k_3, j\omega) \approx \tilde{W}^*(\Delta x_1, k_2, k_3, j\omega) = \exp(jk_1^* \Delta x_1). \quad (5.18)$$

This operator is equal to the exact inverse for  $(k_2^2 + k_3^2 \leq k^2)$ . Outside this range, the inverse operator is also exponentially decaying and therefore stable. The inverse extrapolation of the wavefield from the plane  $x_1 = 0 (= x_{1,0})$  back to a plane  $\Delta x_1$  can be written in the  $(x_1, k_2, k_3, j\omega)$  domain as

$$\tilde{p}^-(\Delta x_1, k_2, k_3, j\omega) \approx \tilde{F}(\Delta x_1, k_2, k_3, j\omega) \tilde{p}^-(0, k_2, k_3, j\omega). \quad (5.19)$$

$\tilde{p}^-$  denotes a wave propagating in the negative  $x_1$  direction. Recursive inverse wavefield extrapolation from  $x_{1,i-1}$  to a subsequent plane  $x_{1,i}$  can be described by

$$\tilde{p}^-(x_{1,i}, k_2, k_3, j\omega) \approx \tilde{F}(x_{1,i} - x_{1,i-1}, k_2, k_3, j\omega) \tilde{p}^-(x_{1,i-1}, k_2, k_3, j\omega). \quad (5.20)$$

### 5.1.4 Imaging

With the phaseshift operator and a given velocity model of the subsurface, the wavefield at any plane  $x_{1,i}$  can be calculated from the response that is recorded at  $x_{1,0}$  [Berkhout, 1985]. To get a migrated section of a recorded data set, the reflectivity at different  $x_{1,i}$  planes has to be determined. The step size  $\Delta x_1$  depends on the required accuracy of the final image. On each  $x_{1,i}$  plane, the inverse extrapolated recorded wavefield  $\tilde{p}^-$  and the forward extrapolated source wavelet  $\tilde{p}^+$  have to be calculated using Equations 5.16 and 5.20. Both wavefields are transformed back to the  $(\mathbf{x}, j\omega)$  domain and correlated with each other [Berkhout, 1985].

$$\hat{X}(x_{1,i}, x_2, x_3, j\omega) = \hat{p}^-(x_{1,i}, x_2, x_3, j\omega) [\hat{p}^+(x_{1,i}, x_2, x_3, j\omega)]^* . \quad (5.21)$$

The inverse Fourier transform at  $t = 0$  gives an estimate of the desired reflectivity at level  $x_{1,i}$ . This Fourier transform thus reduces to summing  $\hat{X}$  over all frequencies:

$$\langle R(x_{1,i}, x_2, x_3) \rangle = \frac{1}{\pi} \Re \int_0^{\infty} \hat{X}(x_{1,i}, x_2, x_3, j\omega) d\omega. \quad (5.22)$$

With this recursive extrapolation of the data and the source signal through the sub-surface, the imaged data set can be built. It will show all reflectors and diffractors in their correct position if the velocity model is correct.

## 5.2 Extrapolation operator optimisation in 2-D

When installing seismic sources and receivers on the head of the TBM, the design of the cutter wheel puts constraints on the possible configurations. It is not realistic to put a large number of transducers on the arms. The rotation of the wheel provides an advantage here. In the time lapse of one complete rotation, the TBM has only moved forward a few centimetres, a small distance compared to the resolution of the shear waves in soft soil. This means that during one rotation, several measurements can be made for which it can be assumed that they are all taken at the same position of the TBM. Therefore, a large set of measurements can be made with only a limited number of receivers, which are all positioned at a different distance from the axis.

In the remainder of this thesis, only 2-D examples are discussed where  $x_2 = 0$  and wave propagation is calculated in the  $(x_1, x_3)$ -plane. A vertical line of receivers at a constant spacing and a source that coincides with the middle receiver represents the transducers on the head of the TBM. This configuration will rarely occur in reality. Because of the rotation of the cutter wheel this is still a realistic assumption. If all receivers are placed on the arms of the wheel at a different distance to the axis, then each one will cross one of the implied positions at some point during one rotation while the horizontal progress of the TBM is negligible.

The derivation of the imaging scheme as performed in the previous section is based on compressional or P-waves. The experiments described in Part I of this thesis

have shown that the TBM emits shear waves and that those are favourable for propagation in the soft soils of the shallow subsurface. The water that is present in the pores would affect the compressional waves too much. In the 2-dimensional case, the same derivation holds for horizontally polarized shear or SH-waves. Table 5.2 shows the corresponding field quantities, medium parameters and source function.

	wave fields			medium parameters		sources
P (fluids)	$p$	$v_1$	$v_3$	$\kappa$	$\rho$	$q$
SH (solids)	$v_2$	$-\tau_{21}$	$-\tau_{23}$	$\rho$	$1/\mu$	$f_2$

**Table 5.2:** Overview of field quantities, medium parameters and source functions for compressional and shear waves in 2-D (pressure  $p$ , particle velocity  $v_i$ , stress  $\tau_{ij}$ , compressibility  $\kappa$ , mass density  $\rho$ , shear modulus  $\mu$ , source of volume injection  $q$ , source of volume force  $f_i$ )

### 5.2.1 Phaseshift operator

Phaseshift migration has the advantage of using simple multiplications of the data with the phaseshift operator in the wavenumber-frequency domain and therefore the data should be transformed from the spatial domain to the wavenumber domain. Because of the specific limitations in tunnelling applications, there are only a few receivers and their total aperture is limited. A spatial Fourier transform will introduce large artefacts into the data. Another disadvantage of this phaseshift operator is that the medium in which the operator is applied should be laterally invariant. In traditional seismic applications where receivers are placed on the surface, lateral invariance means horizontal homogeneous layers. In the tunnelling configuration, the receivers are located in a vertical plane and thus depth invariance is required, which means that the TBM should be completely located in one horizontal layer. During the construction of a tunnel however, the TBM will often move into more than one horizontal layer. The assumption of depth invariance is clearly rather unrealistic. In the space frequency domain, lateral variations of the subsurface can be taken into account. The properties of the operator can be ad-

justed based on the soil parameters at the different input points of the extrapolation.

A space-frequency operator is obtained by an inverse Fourier transform of the phaseshift operator in the wavenumber-frequency domain, back to the space-frequency domain. For the 2-dimensional situation, the phaseshift operator, derived from Equation (5.14) with  $k_2 = 0$ , becomes [Gazdag, 1978]:

$$\tilde{W}(\Delta x_1, k_3, j\omega) = \exp(-jk_1 \Delta x_1), \quad (5.23)$$

in which  $k_1$  is defined as

$$k_1 = \begin{cases} \sqrt{k^2 - k_3^2} & k_3^2 \leq k^2, \\ -j\sqrt{k_3^2 - k^2} & k_3^2 > k^2. \end{cases} \quad (5.24)$$

If the spatial operator has to be used in a recursive extrapolation scheme, transforming this equation to the space-frequency domain has to be done in an optimal way so that the result is a stable spatial convolution operator. Analytically, the inverse Fourier transform of Equation (5.23) is a scaled Hankel function [Berkhout, 1984]

$$W(\Delta x_1, x_3, j\omega) = \frac{-jk\Delta x_1}{2r} H_1^{(2)}(kr), \quad (5.25)$$

with  $r = \sqrt{(\Delta x_1)^2 + x_3^2}$  and  $H_1^{(2)}(kr)$  the first order Hankel function of the second kind. The amplitudes of both the phaseshift operator and of its analytical inverse Fourier transform are plotted in Figure 5.2 for a situation with the values of the parameters comparable to circumstances of shear waves for tunnelling in soft soil as listed in Table 5.3. This results in  $k = \omega/c = 4\pi/3$ . The amplitude of the phase-shift operator equals unity for  $k_3^2 \leq k^2$  and is exponentially decaying outside this interval.

The Hankel function gives a very long spatial operator because the amplitude decreases with  $r^{-3/2}$  in the far field. This long operator has several disadvantages. The main concern is spatial operator aliasing. Secondly, a long spatial operator loses the flexibility for application in lateral varying media. Also, for configurations with a large number of geophones it is rather inefficient to use this operator

frequency $f$	100 Hz
receiver spacing $\Delta x_3$	0.5 m
extrapolation step $\Delta x_1$	0.1 m
velocity $c$	150 m/s
number of samples $N_s$	512

**Table 5.3:** Parameters of phaseshift operator

since convolution with this operator will require long computation times. To reduce computation times, the spatial operator could be truncated to a more suitable length. In case of a situation with a small number of receivers on the other hand, there is no data available outside the range of the receivers and the operator will automatically be truncated during the application of the convolution. The influence of this simple shortening of the Hankel function on the amplitudes of the wavenumber spectrum is demonstrated in Figure 5.3 for several operator lengths. The spatial operator as given in Figure 5.2b is cut off symmetrically around  $x_3 = 0$  (giving an odd number of points) at four different operator lengths and transformed to the wavenumber domain. The number of samples  $M_s$  of the operator decreases from  $M_s = 125$  in Figure 5.3a, to  $M_s = 75$  in Figure 5.3b,  $M_s = 35$  in Figure 5.3c and  $M_s = 15$  in Figure 5.3d. All plots are zoomed in on the phaseshift operator (dashed line) around 1 since this area determines the stability of the operator. For easy comparison, all axes are on the same scale.

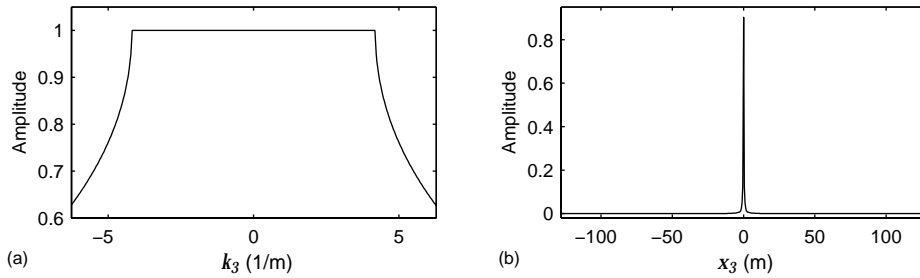


**Figure 5.2:** Phaseshift operator for  $f(= \omega/2\pi) = 100$  Hz,  $\Delta x_3 = 0.5$  m,  $\Delta x_1 = 0.1$  m,  $c = 150$  m/s and  $N_s = 512$  (resulting in  $k = \omega/c = 4\pi/3$ ), in the wavenumber domain (a) and the spatial domain (b)

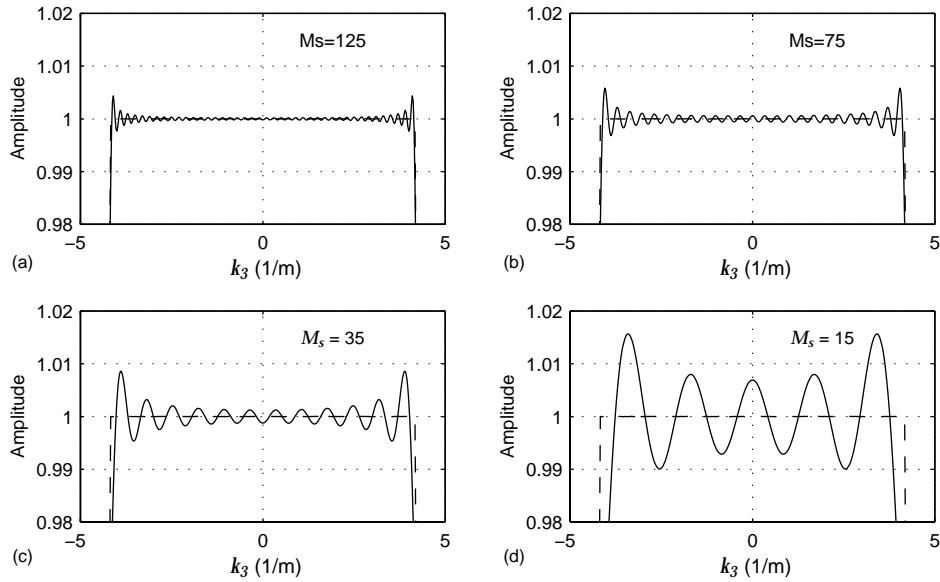


**Figure 5.3:** Wavenumber spectrum after truncation of the spatial phase shift operator to 125 samples (a), 75 samples (b), 35 samples (c) and 15 samples (d) (solid line = truncated operator, dashed line = phase shift operator)

In a recursive extrapolation scheme, the wavefield at wavenumbers where the amplitude is larger than 1 will be amplified in each extrapolation step and will cause the data to blow up. The more extrapolation steps have to be calculated, the larger the error will become. It is obvious from Figure 5.3 that the operator becomes more unstable when its length decreases, especially for waves travelling at high angles and  $k_3$  approaching  $k$ . In this example for an operator of 125 samples, a maximum amplitude of 1.0043 is reached. After 50 extrapolation steps (= 5m), this will already cause a total deviation of 24% at this particular  $k_3$ . The operator truncated to 75 samples gives a maximum amplitude of 1.0058 (34% total error). For 35 samples, this increases to 1.0086 (53% total error) and cutting the operator to 15 samples introduces a maximum amplitude of 1.0157 which will lead to an error of even 117% after 50 extrapolation steps. This will clearly have an extremely negative effect on the migration result of the data. Stability is therefore a crucial factor in operator design.

An optimal operator needs to be accurate in the wavenumber range of interest and

stable within the whole range. Holberg [1988], Blacqui re et al. [1989], Hale [1991], Nautiyal et al. [1993] and Thorbecke [1997] have done research on the development of unconditionally stable, short spatial operators. Thorbecke [1997] gives an extended comparison of these methods and describes a weighted least-squares operator optimisation, which will be expanded in this thesis.

### 5.2.2 Weighted least-squares approximation

The discrete spatial Fourier transform of a spatial extrapolation operator  $W$  is defined as

$$\tilde{W}(\Delta x_1, n\Delta k_3, j\omega) = \Delta x_3 \sum_{m=M_1}^{M_2} \exp(jn\Delta k_3 m\Delta x_3) W(\Delta x_1, m\Delta x_3, j\omega) \quad \text{for } N_1 \leq n \leq N_2. \quad (5.26)$$

$\tilde{W}$  is an approximation of the exact phase-shift operator in the wavenumber domain, while  $W$  is the desired short spatial operator. The length of the spatial operator is determined by  $M_1$  and  $M_2$ .  $N_1$  and  $N_2$  set the length of the Fourier transform. In matrix notation this becomes

$$\tilde{\mathbf{W}} = \Gamma \mathbf{W} \quad (5.27)$$

or

$$\begin{bmatrix} \tilde{W}(\Delta x_1, N_1\Delta k_3, j\omega) \\ \vdots \\ \tilde{W}(\Delta x_1, 0, j\omega) \\ \vdots \\ \tilde{W}(\Delta x_1, N_2\Delta k_3, j\omega) \end{bmatrix} = \Gamma \begin{bmatrix} W(\Delta x_1, M_1\Delta x_3, j\omega) \\ \vdots \\ W(\Delta x_1, 0, j\omega) \\ \vdots \\ W(\Delta x_1, M_2\Delta x_3, j\omega) \end{bmatrix}, \quad (5.28)$$

with

$$\Gamma = \Delta x_3 \begin{bmatrix} \exp(jN_1 \Delta k_3 M_1 \Delta x_3) & \cdots & 1 & \cdots & \exp(jN_1 \Delta k_3 M_2 \Delta x_3) \\ \vdots & & \vdots & & \vdots \\ 1 & & \cdots & 1 & \cdots & 1 \\ \vdots & & \vdots & & \vdots & \\ \exp(jN_2 \Delta k_3 M_1 \Delta x_3) & \cdots & 1 & \cdots & \exp(jN_2 \Delta k_3 M_2 \Delta x_3) \end{bmatrix}. \quad (5.29)$$

The wavenumber sampling is given by

$$\Delta k_3 = \frac{2\pi}{(N_2 - N_1 + 1)\Delta x_3}. \quad (5.30)$$

To make sure that the spatial operator is zero outside its working length, the number of samples in the wavenumber-frequency domain must be greater than or equal to the number of receivers, thus  $N_s \geq M_s (= M_2 - M_1 + 1)$ . This means that Equation (5.28) has more equations than unknowns and should be solved using an approximation procedure like the weighted least-squares method.

To determine the optimal solution of Equation (5.28), the difference between the optimised operator  $\tilde{\mathbf{W}}_{opt}$  and the desired operator  $\tilde{\mathbf{W}}_{des}$  has to be considered:

$$\tilde{\mathbf{E}} = \tilde{\mathbf{W}}_{opt} - \tilde{\mathbf{W}}_{des} = \Gamma \mathbf{W}_{opt} - \tilde{\mathbf{W}}_{des}. \quad (5.31)$$

Based on the difference  $\tilde{\mathbf{E}}$ , an error function  $\tilde{\varepsilon}$  is defined by

$$\tilde{\varepsilon} = \tilde{\mathbf{E}}^H \tilde{\Lambda} \tilde{\mathbf{E}}, \quad (5.32)$$

where  $\tilde{\Lambda}$  is a diagonal weight matrix defined by

$$\tilde{\Lambda}_{mn} = w(n\Delta k_3) \delta_{mn} \quad \text{with} \quad N_1 \leq n \leq N_2. \quad (5.33)$$

The weight function  $w(n\Delta k_3)$  is defined in such a way that the desired part of the wavenumber spectrum gets a weight of one. Outside this interval, a low weight factor gives the approximation more freedom to result in a less accurate but stable operator. By changing the parameters of the weight function, the operator can be

designed in an optimal sense.

For the design of the optimal spatial operator, the error function has to be minimized. The solution of the weighted least-squares operator is given by Thorbecke [1997]

$$\mathbf{W}_{opt} = [\Gamma^H \tilde{\Lambda} \Gamma]^{-1} \Gamma^H \tilde{\Lambda} \tilde{\mathbf{W}}_{des}. \quad (5.34)$$

If the weight matrix  $\tilde{\Lambda}$  is replaced by the unit matrix  $\mathbf{I}$ , then the right hand side of Equation 5.34 is an inverse Fourier transform which is truncated to  $M_s$  points in the spatial domain. In this case no optimisation is performed in the operator design.

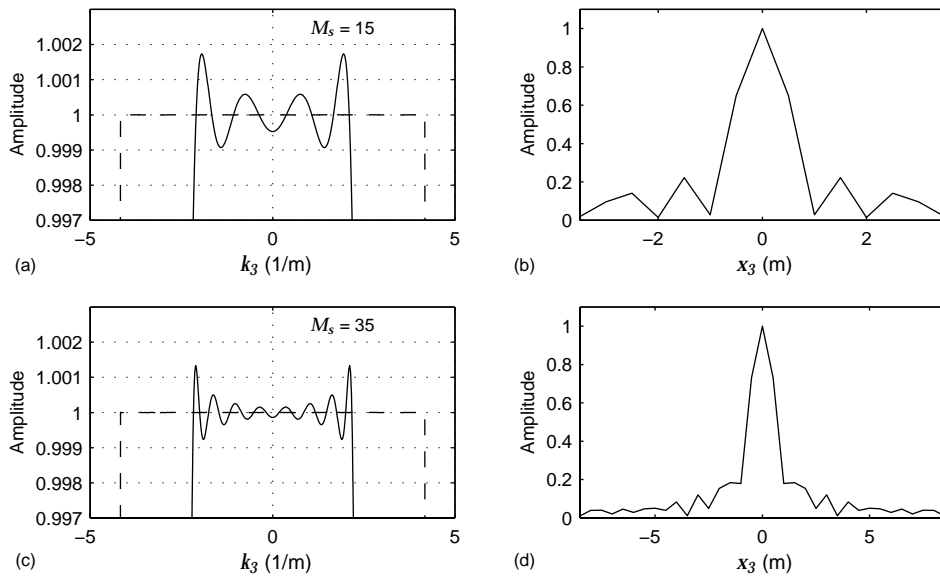


**Figure 5.4:** Short operators designed with weighted least-squares optimisation: 15-points operator in wavenumber domain (a) and in spatial domain (b), 35-points operator in wavenumber domain (c) and in spatial domain (d) (solid line = optimised operator, dashed line = phase shift operator)

The weighted least-squares optimisation is performed for operators with the same parameters as used for the phaseshift operator in Figure 5.2. Figure 5.4 gives the results in the  $k_3$  and the  $x_3$ -domain for two cases, operator length  $M_s = 15$  and

operator length  $M_s = 35$ , keeping the spacing  $\Delta x_3$  identical. In the optimisation it holds that  $|M_1| = |M_2|$ . Figure 5.4a shows the amplitude of the wavenumber spectrum for the 15-points operator (solid line) compared to the exact phaseshift operator (dashed line), Figure 5.4b is the amplitude of the designed spatial operator. In Figure 5.4c and d, the results for the 35-points operator are given. For both operator lengths, the optimisation range in the wavenumber domain is set from  $k_3^- = -2.25$  to  $k_3^+ = 2.25$ , with  $k_3^-$  the negative and  $k_3^+$  the positive limit of the wavenumber range. This corresponds with an operator angle of approximately  $32^\circ$  ( $= \arcsin(k_3^+/k)$ ). Inside this interval, the wavenumber spectrum of the operator has to be as accurate as possible. Outside the interval, the only demand is that the operator is stable, meaning an amplitude less than one. To achieve this, the weight function is set very low, at a value of  $5 \cdot 10^{-5}$ , to give the least-squares algorithm freedom in this range.

The wave spectrum of the optimised operators should be compared with that of the truncated spatial operators, Figure 5.4a with Figure 5.3d for  $M_s = 15$  and Figure 5.4c with Figure 5.3c for  $M_s = 35$ . To examine the stability of the operators, all plots are zoomed in around amplitude 1. Take notice though that the range of the vertical axis is much smaller in Figure 5.4. There is a remarkable decrease in amplitude peaks after optimisation, both for  $M_s = 15$  and  $M_s = 35$ . The 15-points operator now reaches a maximum amplitude of 1.0017 compared to 1.0157 for its truncated equivalent. After 50 extrapolation steps, the total deviation is now only 9%. The maximum amplitude of the 35-points operator decreases from 1.0086 to 1.0013, giving a total error of 7% after 50 extrapolation steps. Compared to the truncated operators, this is a large improvement.

### 5.2.2.1 Desired operator

The shape of the desired operator  $\tilde{W}_{des}$  has a large influence on the result of the optimisation. In Thorbecke [1997], a simple block-filtered phaseshift operator was used. The effect of smoothing the desired operator is discussed in this section.

In Figure 5.5, the entire amplitude range of the wavenumber spectrum of the short operators is shown. Again the dashed line represents the exact phaseshift operator, the solid line is the optimised operator. The third (dashed - dotted) curve is the desired operator. Just like the weight function, the desired operator is a block-filtered phaseshift operator which is equal to the phaseshift operator in the given wavenumber range and zero outside this range. This operator is used as input for

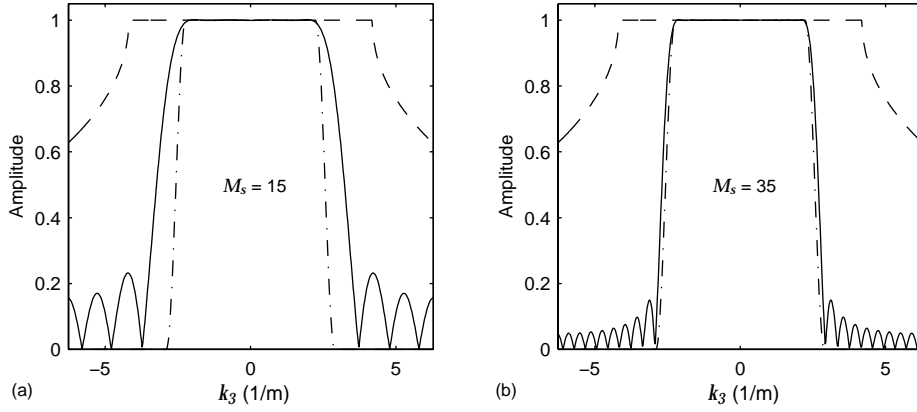


**Figure 5.5:** Amplitude of wavenumber spectrum for 15-points operator (a) and 35-points operator (b) designed with weighted least-squares optimisation (solid line = optimised operator, dashed line = phase shift operator, dashed-dotted line = desired operator)

the optimisation procedure. Figure 5.4 already showed that both approximations are accurate in the wavenumber range between  $k_3^- = -2.25$  and  $k_3^+ = 2.25$ . In Figure 5.5 it can be seen that the requirement of stability outside this range is also fulfilled with an amplitude smaller than one. The shape of the desired operator makes the amplitude decrease to zero in the evanescent field. As a result of the least-squares approximation, the optimised operator oscillates around the desired operator. For the amplitude spectrum, the oscillation happens around one in the  $(k_3^-, k_3^+)$  interval, while in the region with low weight factors, it results in the lobes that are clearly visible in both plots of Figure 5.5. The total number of oscillations over the entire  $k_3$  axis increases with the length of the operator  $M_s$ . If, for a certain  $M_s$ ,  $k_3^+ (= |k_3^-|)$  is set larger, there will be more oscillations in this interval and therefore less lobes outside the optimised  $k_3$  range.

The influence of the oscillating behaviour of the optimised operator can be tracked in Figure 5.6 for a 15-points operator. Two criteria are set up to investigate the quality of the operator, meaning its accuracy and stability, as a function of  $k_3^+ (= |k_3^-|)$ , the wavenumber range of interest. Figure 5.6a shows the energy difference  $E_{diff}$  between the desired operator  $\tilde{W}_{des}$  and the optimised operator  $\tilde{W}_{opt}$  within the wavenumber range  $(k_3^-, k_3^+)$ , defined as

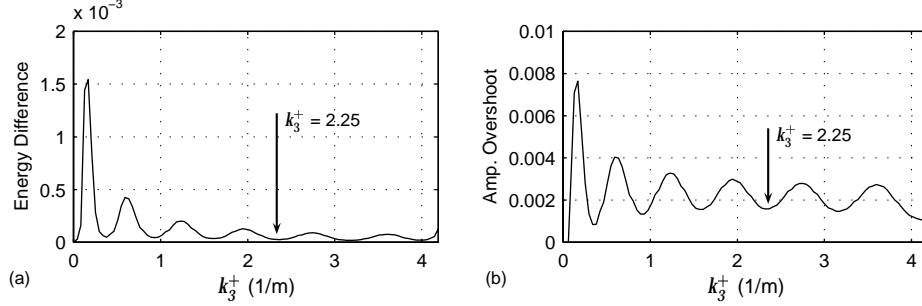


**Figure 5.6:** Energy difference (a) and maximal amplitude overshoot (b) in function of wavenumber optimisation interval for 15-points operator ( $k_3^+ = 2.25$ : wavenumber range of Figure 5.4)

$$E_{diff} = \frac{1}{(k_3^+ - k_3^-)} \sum_n |\tilde{W}_{des}(n\Delta k_3) - \tilde{W}_{opt}(n\Delta k_3)|^2 \quad \text{for } k_3^- \leq n\Delta k_3 \leq k_3^+. \quad (5.35)$$

In this range, the desired operator  $\tilde{W}_{des}$  is equal to the phaseshift operator. The energy difference  $E_{diff}$  gives an indication of the accuracy of the operator in the desired wavenumber range where the least-squares procedure has a weight of one. The curve in Figure 5.6b represents the maximum amplitude larger than one in the entire wavenumber spectrum of the optimised short operator  $\tilde{W}_{opt}$ :

$$A_{max} = \max (|\tilde{W}_{opt}(n\Delta k_3)| - 1) \quad \text{for } N_1 \leq n \leq N_2. \quad (5.36)$$

The amplitude overshoot  $A_{max}$  indicates the expected stability of the operator, also in the evanescent field since the amplitudes over the entire wavenumber domain is considered. The undulating behaviour of both the energy difference  $E_{diff}$  and the maximum amplitude overshoot  $A_{max}$  is caused by the oscillations of the optimised operator  $\tilde{W}_{opt}$ . The transition of energy of a new side lobe into the optimised range interval which occurs when this range is increased, causes amplitude peaks around  $k_3^-$  and  $k_3^+$ . These cause the local maxima in the energy difference  $E_{diff}$  and the maximum amplitude overshoot  $A_{max}$  of Figure 5.6. Therefore the behaviour of both curves is very parallel. The 15-points optimised operator with  $k_3^+ = 2.25$  which was shown in Figure 5.4 is located in one of the local minima as indicated in Figure 5.6. Not taking the smallest wavenumbers into consideration, the overshoot can become even higher than 0.003 for other  $k_3$  values. A good choice of the

wavenumber range for the short operator is therefore crucial.

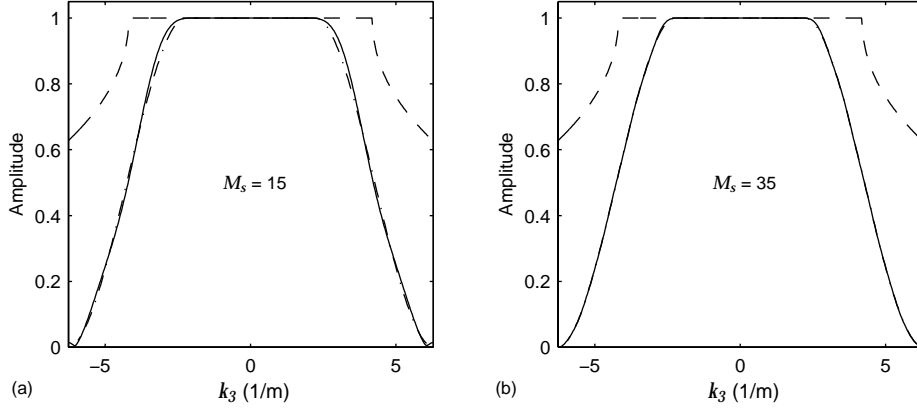


**Figure 5.7:** Amplitude of wavenumber spectrum for 15-points operator (a) and 35-points operator (b) designed with weighted least-squares optimisation using a smoothed desired operator (solid line = optimised operator, dashed line = phase shift operator, dashed-dotted line = desired operator)

The shape of the desired operator  $\tilde{W}_{des}$  in the wavenumber domain has a large influence on the optimisation. The block-filtered phaseshift operator used in the previous examples has a very abrupt transition from a value of one in the optimisation range to zero in the evanescent field. This causes the amplitude peaks in the wavenumber spectrum. Choosing a smoother desired operator might also smooth the behaviour of the optimised operator. The wavenumber spectrum of the desired operator should always be equal to that of the phaseshift operator in the wavenumber range  $(k_3^-, k_3^+)$ . In the evanescent field, both amplitude and phase of the new desired operator  $\tilde{W}_{des}$  are defined by a cubic spline  $s(k_3)$  which smoothly goes to zero for  $|k_3| = \pi/\Delta x_1$ . So the next equations hold:

$$\| \tilde{W}_{des}(\Delta x_1, k_3, j\omega) \| = \begin{cases} 1 & |k_3| \leq k_3^+, \\ \| s(k_3) \| & |k_3| > k_3^+, \\ 0 & |k_3| = \pi/\Delta x_1, \end{cases} \quad (5.37)$$

$$\arg(\tilde{W}_{des}(\Delta x_1, k_3, j\omega)) = \begin{cases} -jk_3\Delta x_3 & |k_3| \leq k_3^+, \\ \arg(s(k_3)) & |k_3| > k_3^+, \\ 0 & |k_3| = \pi/\Delta x_1. \end{cases} \quad (5.38)$$

At  $|k_3| = \pi/\Delta x_1$ ,  $s(k_3)$  has a first derivative of zero, at  $|k_3| = k_3^+$  the first derivative is equal to that of the exact phase shift operator for this  $|k_3|$ .

Figure 5.7 shows the amplitude of the wavenumber spectrum of this new desired operator  $\tilde{W}_{des}$  (dashed-dotted line) and its 15 (Figure 5.7a) and 35-points (Figure 5.7b) optimised equivalents  $\tilde{W}_{opt}$  (solid line) for the same wavenumber range as was used in Figure 5.4 ( $-k_3^- = k_3^+ = 2.25$ ). The optimised operators are excellent approximations of the desired wavenumber spectrum for both operator lengths. For  $M_s = 35$  in Figure 5.7b, the difference between both curves is not even visible. The side lobes in the evanescent field have disappeared. The operator is still stable and its general behaviour is much smoother.

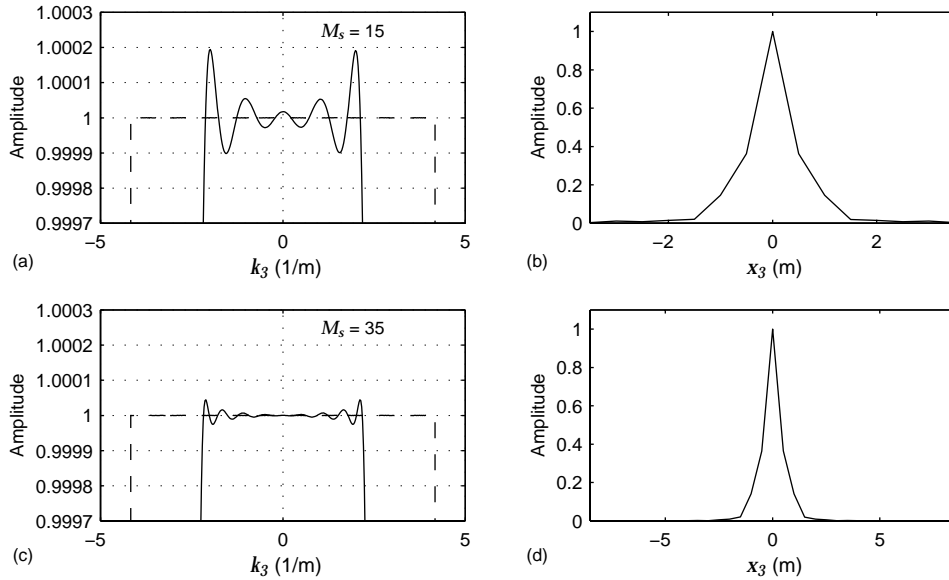


**Figure 5.8:** Short operators designed with weighted least-squares optimisation using a smoothed desired operator: 15-points operator in wavenumber domain (a) and in spatial domain (b), 35-points operator in wavenumber domain (c) and in spatial domain (d) (solid line = optimised operator; dashed line = phase shift operator)

Besides stability, accuracy is the main requirement. The plots in Figure 5.8a and c zoom in on the operators around amplitude one. Note that the vertical scale on these plots is 10 times smaller compared to Figure 5.4a and c, which did not have

the smoothed desired operator. The approximation of the phaseshift operator has improved. With a maximum amplitude of 1.00019, application of the 15-points operator for 50 recursive extrapolation steps will give an error of only 0.98%. An even larger effect can be seen for the 35-points operator where the maximum amplitude of the wavenumber spectrum has decreased to 1.00004, leading to a deviation of 0.22% after 50 extrapolations.

The smoothing of the desired operator also has a positive effect on the spatial operator that will be used in the extrapolation. Figure 5.8b and d show the respective 15 and 35-points spatial operators that are designed in this weighted least-squares scheme. Compared to the results in Figure 5.4b and d where the block spectrum was approximated, these operators also behave much smoother.

The influence of this smoothed desired operator also has a major influence on the phase of the wavenumber spectrum of the operator. This is shown in Figure 5.9. In Figure 5.9a and b, an approximation of the wavenumber spectrum is calculated for the 15 and 35-points operator where the desired operator  $\tilde{W}_{des}$  is a block function (dashed-dotted line). It is cut off at  $k_3^- = -2.25$  and  $k_3^+ = 2.25$  and equals zero outside this range. The optimised operator  $\tilde{W}_{opt}$  (solid line) is very accurate in the wavenumber range of interest. Going to the region with low weight however, the optimisation result fluctuates strongly along the desired operator. The wrapping of the phase indicates a large overshoot.

Much improvement can be seen in Figure 5.9c and d for the same operators where the desired operator has been changed into a more smoother version, using the cubic spline given in Equation (5.43). The accuracy in the  $(k_3^-, k_3^+)$  range is much higher and the behaviour of the phase outside this range is much better. Just like for the amplitude, the phase of the wavenumber spectrum for the 35-points operator fit the desired operator almost perfectly. The 15-points operator deviates a little bit in the evanescent field but it is still an excellent optimisation.

Using the exact unfiltered phaseshift operator as desired operator  $\tilde{W}_{des}$  would have a similar effect on the optimisation as the block-filtered function. The behaviour of its wavenumber spectrum around  $k$  is not smooth and will cause similar overshoots both in amplitude and in phase. It also implies that the optimisation wavenumber range is equal to the interval  $(-k, k)$  and therefore the optimised operator  $\tilde{W}_{opt}$  would have to be accurate over this entire interval which leaves less freedom for

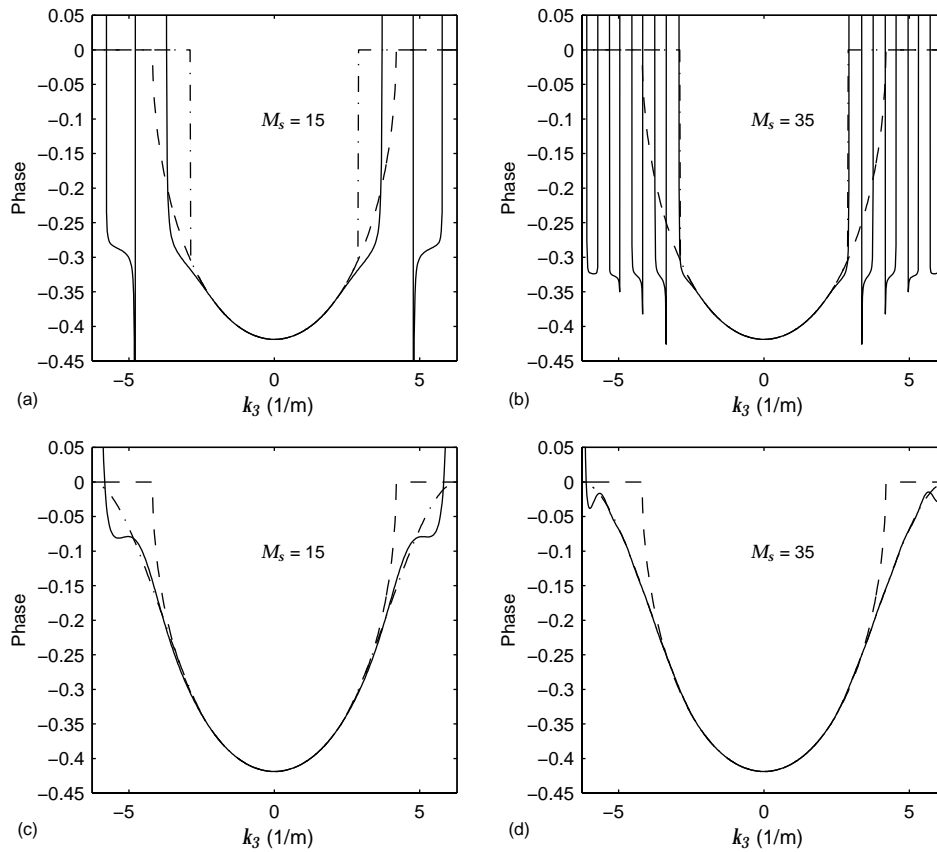


**Figure 5.9:** Phase of wavenumber spectrum for 15-points operator designed with weighted least-squares optimisation using a block-filtered desired operator (a) and a smoothed desired operator (c), for 35-points operator designed with weighted least-squares optimisation using a block-filtered desired operator (b) and a smoothed desired operator (d) (solid line = optimised operator, dashed line = phase shift operator, dashed-dotted line = desired operator)

the least-squares approximation.

For the rest of the discussion in this thesis, the smoothed desired operators will be used because they have a more stable behaviour than the blocked operators.

### 5.2.2.2 Wavenumber range

In the previous section it was already indicated how the wavenumber range of interest of the desired operator has an influence on the optimised result. A more elaborated discussion for the smoothed desired operator is given in this section.

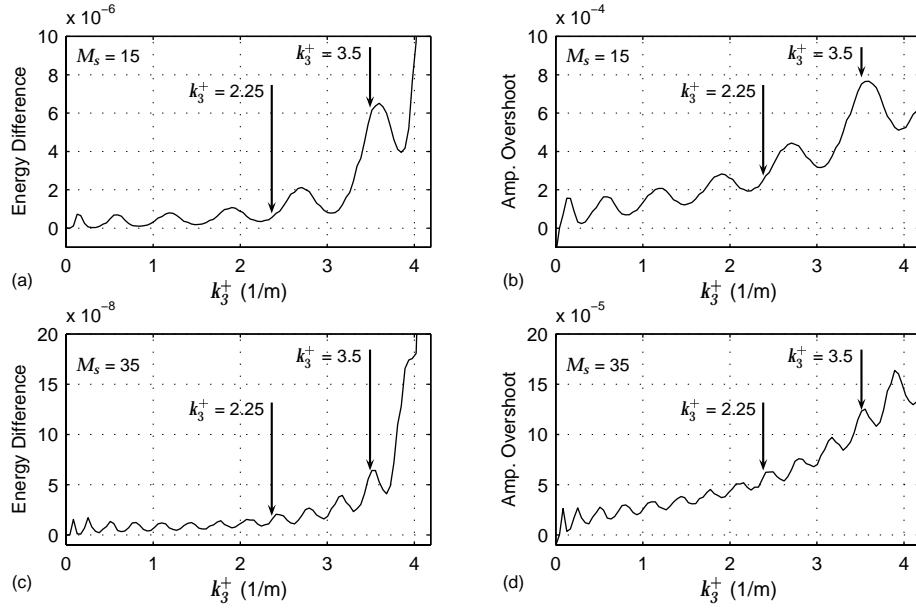


**Figure 5.10:** Energy difference (a) and maximal amplitude overshoot (b) for 15-points operator and energy difference (c) and maximal amplitude overshoot (d) for 35-points operator, in function of wavenumber optimisation interval ( $k_3^- = 2.25$ : range of wavenumber Figure 5.8,  $k_3^+ = 3.5$ : wavenumber range of Figure 5.11)

Just like in Figure 5.6, the energy difference  $E_{diff}$  and the maximum amplitude overshoot  $A_{max}$  in the wave spectrum for the smoothed operators is determined as a function of the wavenumber range ( $k_3^-, k_3^+$ ). Figure 5.10a and b show the result for the 15-points operator. The same undulating behaviour as in Figure 5.6 can be observed in these curves, with minima and maxima for the same wavenumbers. This indicates that the energy is still divided over lobes. As a result of higher accuracy of the smoothed operator, there is a large increase in energy difference and maximum amplitude.

The energy difference  $E_{diff}$  and maximum amplitude  $A_{max}$  for the smoothed 35-points operator are determined and plotted in Figure 5.10c and d. In Figure 5.8,

and especially in Figure 5.5, it was clearly visible that the number of oscillations increase with the number of samples in the spatial operator. This is reflected back in the energy difference and the maximum amplitude where the number of undulations increases proportionally.

The general trend of the curves has changed significantly though with smoothing of the desired operator. For the blocked operator (Figure 5.6) both energy difference  $E_{diff}$  and maximum amplitude increased for a smaller  $k_3^+$ -range while for the smoothed operator (Figure 5.10) the opposite behaviour for both properties can be seen. Intuitively, this trend is more logical. Both the energy difference and the maximum amplitude  $A_{max}$  give an indication of the error in the optimisation. When a smaller wavenumber range is proposed, an accurate wavenumber spectrum is required over a smaller interval. This means that the conditions of the optimisation are less strict and therefore should be fulfilled more easily, with a smaller error. Clearly the approximation of a blocked function has such a large influence on the conditions for the optimisation that this general trend gets overruled.

The exact phaseshift operator is defined by the spatial sampling of the receivers  $\Delta x_3$ , the extrapolation step  $\Delta x_1$  and the frequency  $f$  and the background velocity  $c$  as  $k = \omega/c = 2\pi f/c$ .  $k_3^+$  determines the interval where the optimised operator should be accurate to the phaseshift operator. Depending on the application,  $k_3^+$  can vary between zero and  $k$ . Different criteria could be used to determine the best wavenumber range for the application. External circumstances imposed by the tunnelling application will also be important. The energy difference with the exact phaseshift operator in the wavenumber spectrum and the maximum amplitude of the wavenumber spectrum of the optimised operator as shown in Figure 5.10 are two possible criteria based on theoretical rules of thumb. Both are considered in this thesis.

The operators in Figure 5.8 were designed for  $k_3^+ = 2.25$  which is indicated in Figure 5.10. The energy difference for the 15-points operator equals  $3.5 \cdot 10^{-7}$ , its amplitude overshoot is  $1.9 \cdot 10^{-4}$ . The 35-points operator is much more accurate with an energy difference of  $8.9 \cdot 10^{-9}$  and an amplitude overshoot of  $4.5 \cdot 10^{-5}$ . For both criteria, these optimisations are located in a local minimum. An increase of the interval of interest to  $k_3^+ = 3.5$  has a large influence on the design. Not only the increasing general trend has a negative effect on the accuracy, both criteria also show a local maximum for this  $k_3^+$  value as can be seen in Figure 5.10. This results in an energy difference of  $6.1 \cdot 10^{-6}$  and an amplitude overshoot of  $7.5 \cdot 10^{-4}$  for the

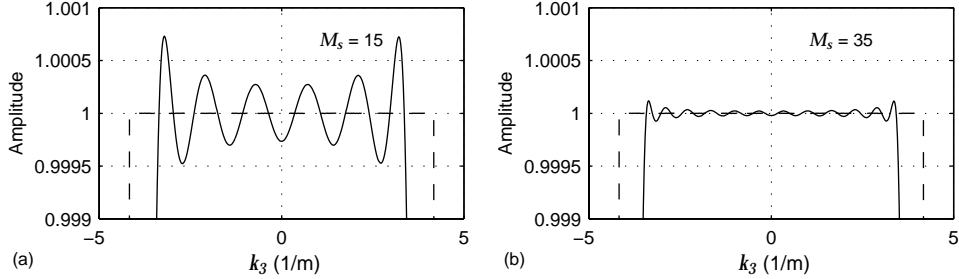


**Figure 5.11:** Influence of the wavenumber optimisation interval on the wavenumber spectrum for 15-points operator (a) and 35-points operator (b) with  $k_3^- = -3.5$ ,  $k_3^+ = 3.5$  (solid line = optimised operator, dashed line = phase shift operator)

15-points operator. The 35-points operator has an energy difference of  $6.4 \cdot 10^{-8}$  and an amplitude overshoot of  $1.2 \cdot 10^{-4}$ . The influence on the operator design can be seen in Figure 5.11. Note that the amplitude scale is more than 3 times larger than for the operators in Figure 5.4 and compared to the plots in Figure 5.4, the accuracy is still much higher.

In practice, the optimal  $(k_3^-, k_3^+)$ -range for the operator should be based on a combination of both external conditions of the application and theoretical criteria like discussed in this section. Influences of both should be weighed against each other. For the general trend, the operator is more accurate for a smaller  $(k_3^-, k_3^+)$ -range. By enlarging the wavenumber range from 2.25 to 3.5, the operator angle grows from  $32^\circ$  to  $57^\circ$ . Depending on the circumstances, a lower accuracy could be accepted in return for a larger operator angle.

### 5.2.2.3 Weight

Another parameter that determines the optimisation procedure is the weight factor. It influences both the accuracy and the stability as will be shown in this section.

The weight factor indicates the freedom given to the weighted least-squares procedure. Within the interval  $(k_3^-, k_3^+)$ , the weight will always be set to one which means that the approximation in this range should be as good as possible. The weight factor outside this range is adjustable. The lower its value is chosen, the more flexible the approximation in the evanescent field is allowed to be. The wavenumber spec-

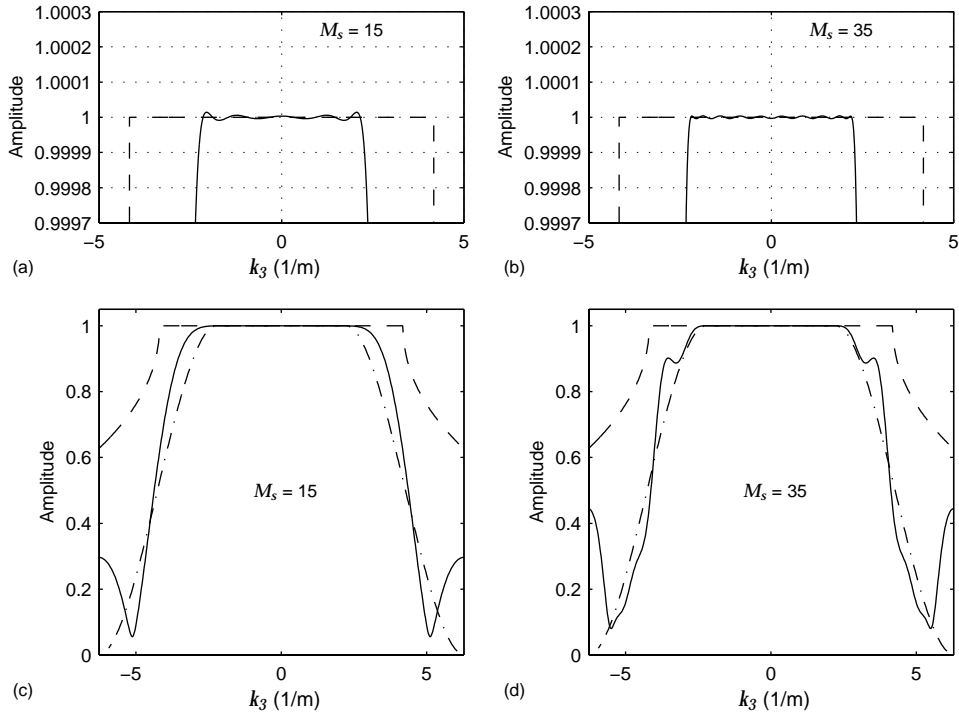


**Figure 5.12:** Influence of the weight factor  $5.10^{-8}$  on the accuracy of the wavenumber spectrum for 15-points operator (a) and 35-points operator (b) and on the evanescent field for 15-points operator (c) and 35-points operator (d) (solid line = optimised operator; dashed line = phase shift operator; dashed-dotted line = desired operator)

trum of the optimised operator can deviate from the desired operator as long as its behaviour is stable. If the weight is set to one for the entire wavenumber domain ( $\tilde{\Lambda} = \mathbf{I}$ ), no optimisation is performed, which results in the simple truncation of the spatial operator as was shown in Figure 5.3.

The weight has an influence both inside and outside the  $(k_3^-, k_3^+)$  range though. If a smaller weight is chosen, allowing more freedom in the approximation in the evanescent field, the accuracy of the wavenumber spectrum inside the optimisation interval increases. This can be seen in Figure 5.12a for the 15-points operator and in Figure 5.12b for the 35-points operator where a weight factor of  $5.10^{-8}$  is used. The amplitude axis has the same scale as in Figure 5.8 where a larger weight factor of  $5.10^{-5}$  was applied. The approximation of the phaseshift operator is clearly much better in Figure 5.12. There is however an exchange between accuracy in the

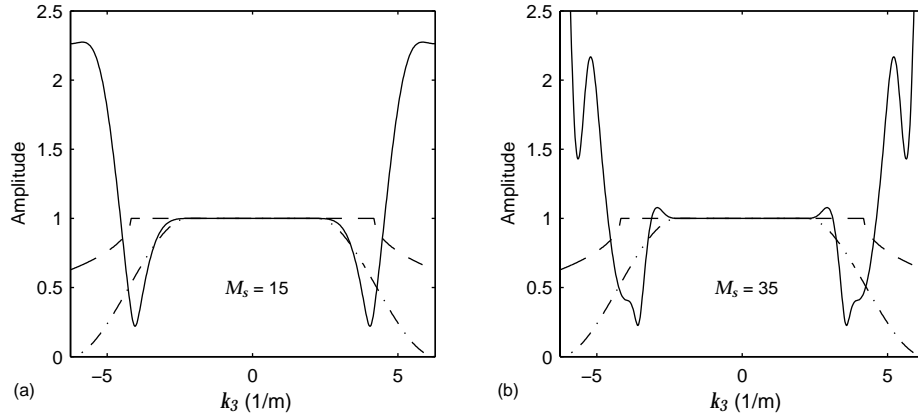


**Figure 5.13:** Influence of a very small weight factor  $5 \cdot 10^{-9}$  on the evanescent field of the wavenumber spectrum for 15-points operator (a) and 35-points operator (b) (solid line = optimised operator, dashed line = phase shift operator, dashed-dotted line = desired operator)

$(k_3^-, k_3^+)$  interval and the stability outside this interval. This can be seen when comparing the entire wavenumber spectrum of Figures 5.12c and 5.7a for the 15-points operator and Figures 5.12d and 5.7b for the 35-points operator. The optimised operator  $W_{opt}$  deviates more from the desired operator  $W_{des}$  when a higher weight is used. Because of allowing more deviation in the evanescent field, the side lobes become visible in the wavenumber spectrum again. Of course the operator is still stable, the amplitude stays well under one. Since there are no propagating waves in this wavenumber range, stability is the only requirement. This behaviour does give a first indication that the optimisation will not keep getting better by decreasing the weight factor until zero. Figure 5.13 gives a very clear example. Here the weight is lowered to  $5 \cdot 10^{-9}$ . Of course the accuracy of the operator has improved again, but the wavenumber spectrum of the operator is no longer stable. In the evanescent field, extremely large amplitude overshoots are present for both operator lengths. Experience has shown that  $5 \cdot 10^{-5}$  is an excellent weight factor, suited for most wavenumber ranges. The accuracy of the operator is high enough and the cubic spline of the desired operator leads to a smooth wavenumber spectrum.

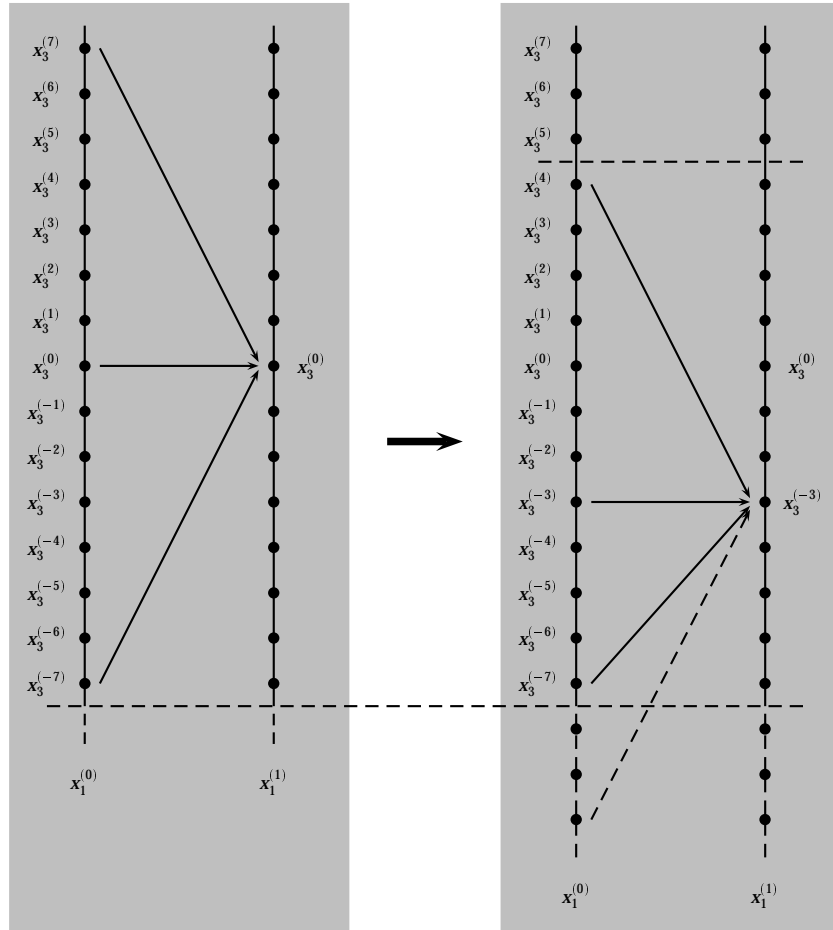


**Figure 5.14:** Use of symmetric extrapolation operator in a symmetric configuration at  $x_3^0$  and an asymmetric configuration at  $x_3^{-3}$

### 5.2.3 Asymmetric operator design

When applying the short spatial operator in a recursive extrapolation scheme where many receivers are available, the operator is shifted over all receiver positions. The wave field in one extrapolation point at a next  $x_1$  level is calculated from the information present at the previous level in the data-points that symmetrically surround the point of interest, based on the operator length. When only a small number of receivers can be installed, an operator with the same length should be designed to

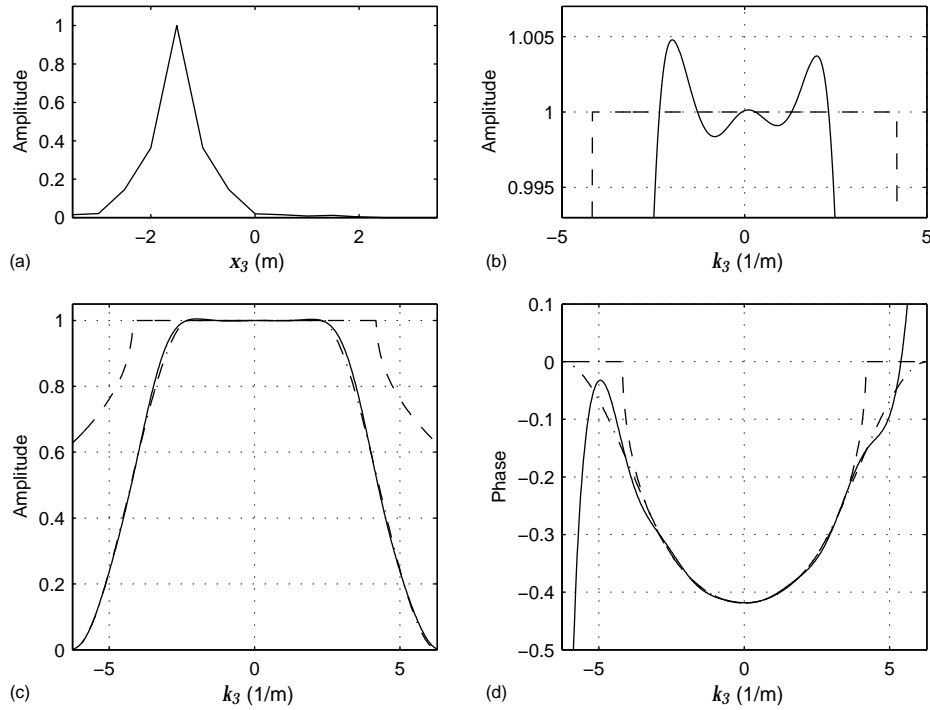


**Figure 5.15:** Truncated 15-points symmetric spatial operator (a) and amplitude (b (zoomed view) and c) and phase (d) of its corresponding wavenumber spectrum at  $x_3^{-3}$  (solid line = optimised operator, dashed line = phase shift operator, dashed-dotted line = desired operator)

make use of all information present in the limited amount of data. A longer operator would only increase computation time but not provide extra information since there is no data outside the range of the receivers. As an example, the 15-points operator designed in a weighted-least-squares approximation with smoothed desired operator (Figure 5.8a and b) is taken. Figure 5.14a sketches the situation where the wave field is extrapolated from 15 data points at level  $x_1^{(0)}$  to the point  $x_3^{(0)}$  at the plane  $x_1^{(1)}$ . Like in the situation with a large number of receivers, the points at the plane  $x_1^{(0)}$  are symmetrically distributed around  $x_3^{(0)}$ . The extrapolation uses all information present at the previous level.

Similar to the situation with a large number of receivers, calculating the extrapolated wave field in any other point requires a shift of the operator over the data set. In Figure 5.14b, the same 15-points operator has moved down to be centred around point  $x_3^{(-3)}$ . Below  $x_3^{(-7)}$  there are no more receivers, so no data either. Therefore

the three deepest points of the spatial operator do not contribute to the extrapolation at all. Since the operator acts outside its array of data points, it seems as if it got truncated after  $x_3^{(-7)}$ . This is indicated by the dashed arrow in Figure 5.14b. Figure 5.15a shows the spatial operator itself. The central point  $x_3^{(0)}$  corresponds with  $x_3 = 0$ . The peak of the operator is located at  $x_3 = x_3^{(-3)}$ . This is the same operator that was designed in Figure 5.8b, shifted 1.5 m and truncated at  $x_3 = x_3^{(-7)}$ .

As a consequence of the shift, the data in points  $x_3^{(5)}$ ,  $x_3^{(6)}$  and  $x_3^{(7)}$  at level  $x_1^{(0)}$  is not taken into consideration during extrapolation of the wavefield to point  $x_3^{(-3)}$  at level  $x_1^{(1)}$ . In Figure 5.15a, zeros are added to the spatial operator from  $x_3 = 2.5$  to 3.5 m. This leads to a first disadvantage of using a shifted short operator in a situation with only a small number of receivers. With every further step from  $x_3^{(0)}$ , less data points are included in the extrapolation. When this few data points are available it would however be inefficient not to include all possible information. It could only improve the extrapolation.

A second disadvantage of applying the shifted and truncated spatial operator in Figure 5.15a can be seen after a Fourier transform to the wavenumber domain. According to Figure 5.15c, the amplitude of the wavenumber spectrum (solid line) is still stable in the evanescent field. In the more detailed plot in Figure 5.15b, it can be seen that the accuracy between  $k_3^- = -2.25$  and  $k_3^+ = 2.25$  has decreased significantly though. The wavenumber spectrum has now a maximum amplitude of 1.0048 compared to 1.0019 before truncation. The more the spatial operator is shifted away from  $x_3^{(0)}$ , the less stable the behaviour of the operator becomes. Because of the recursive extrapolation, this can lead to a blow up of the data. Figure 5.15d shows the phase of the wavenumber spectrum. The accuracy of the phase has decreased also, but truncating the spatial operator has a much smaller effect on the phase than it has on the amplitude.

A solution for both disadvantages is an *asymmetrical* short extrapolation operator that acts on the total array of data points for each output point. This is shown in Figure 5.16a. To determine the wavefield in  $x_3^{(-3)}$  at level  $x_1^{(1)}$ , a 15-points operator should be designed which covers all data points at level  $x_1^{(0)}$ . For each  $x_3^{(i)}$  position, another optimal spatial operator should be found so that shifting and truncation of the operator is no longer necessary. For the design of a weighted least-squares symmetric operator, it holds in Equation (5.28) that

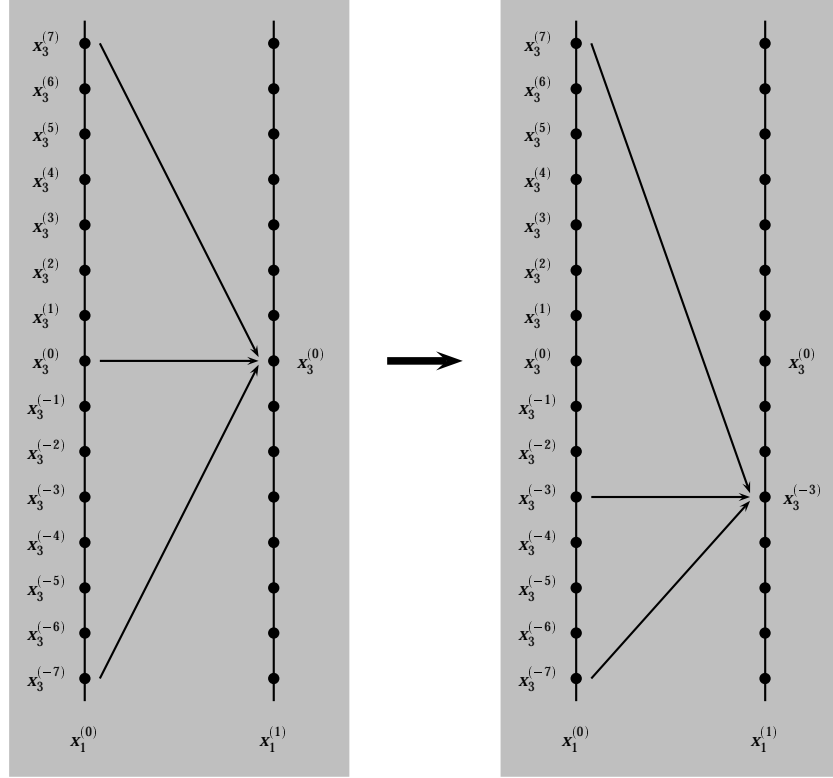


**Figure 5.16:** Use of asymmetric extrapolation operator in an asymmetric configuration at  $x_3^{-3}$

$$M_1 = -M_2, \quad (5.39)$$

$$W(m\Delta x_3) = W(-m\Delta x_3), \quad (5.40)$$

$$\tilde{W}(n\Delta k_3) = \tilde{W}(-n\Delta k_3). \quad (5.41)$$

When the spatial operator is designed asymmetrically, its corresponding wavenumber spectrum will also become asymmetric. In that case, the above requirements will no longer be necessary. This means that the wavenumber range where the operator should be accurate can be chosen asymmetric now, so  $k_3^- \neq -k_3^+$ . The spatial operator for the situation in Figure 5.16 that results from this asymmetric weighted least-squares optimisation is plotted in Figure 5.17a. Its maximum value is located at  $x_3 = -1.5$  m which correspond with  $x_3^{(-3)}$ . The rest of its energy is

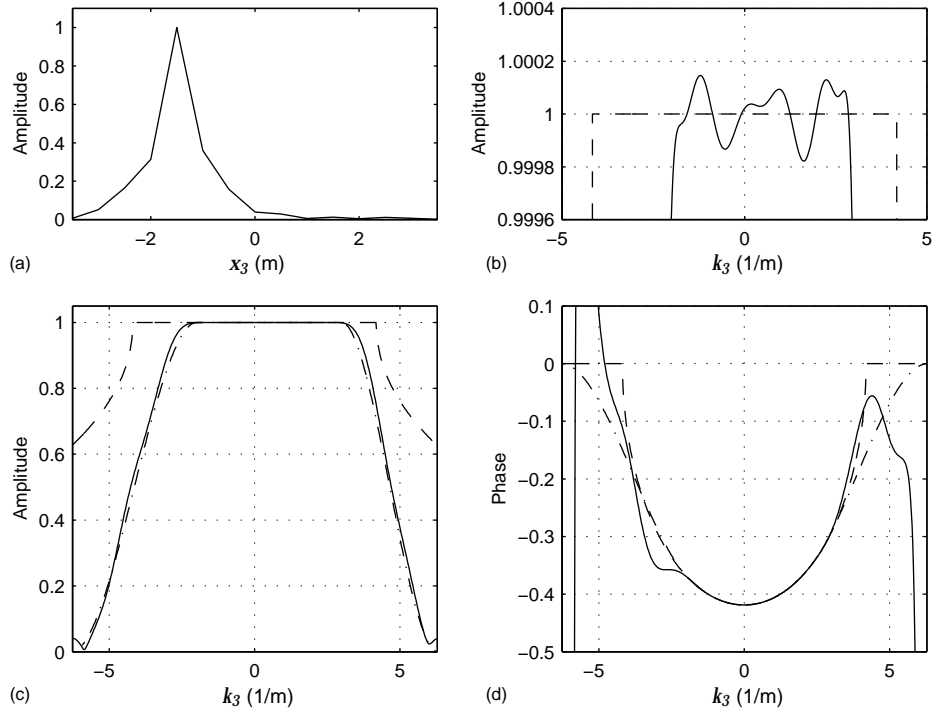


**Figure 5.17:** Asymmetric 15-points spatial operator (a) and amplitude (b (zoomed view) and c) and phase (d) of its corresponding wavenumber spectrum at  $x_3^{-3}$  with  $k_3^- = -2$ ,  $k_3^+ = 3$  (solid line = optimised operator; dashed line = phase shift operator; dashed-dotted line = desired operator)

asymmetrically divided around this maximum with smoothly decreasing amplitude. For the optimisation, the weight factor remained  $5 \cdot 10^{-5}$ . The wavenumber range has been changed to  $k_3^- = -2$  and  $k_3^+ = 3$ . Because of the relative position of the output point, the (minimal) negative extrapolation angle has been chosen smaller while the (maximum) positive extrapolation angle has been set larger. This is reflected back in the operator angles which now vary from  $\arcsin(k_3^-/k) = -29^\circ$  to  $\arcsin(k_3^+/k) = 45^\circ$ . The asymmetry of the wavenumber spectrum can be seen in Figure 5.17c where the desired operator (dashed - dotted line) is tilted more towards the positive wavenumbers. Outside the  $(k_3^-, k_3^+)$  interval, the spectrum of the desired operator is again defined by a cubic spline. Equations (5.42) and (5.43) are now adjusted to

$$\| \tilde{W}_{des}(\Delta x_1, k_3, j\omega) \| = \begin{cases} 1 & k_3^- \leq k_3 \leq k_3^+, \\ \| s_1(k_3) \| & k_3^- > k_3, \\ \| s_2(k_3) \| & k_3 > k_3^+, \\ 0 & |k_3| = \pi/\Delta x_1, \end{cases} \quad (5.42)$$

$$\arg(\tilde{W}_{des}(\Delta x_1, k_3, j\omega)) = \begin{cases} -jk_3\Delta x_3 & k_3^- \leq k_3 \leq k_3^+, \\ \arg(s_1(k_3)) & k_3^- > k_3, \\ \arg(s_2(k_3)) & k_3 > k_3^+, \\ 0 & |k_3| = \pi/\Delta x_1. \end{cases} \quad (5.43)$$

$s_1(k_3)$  and  $s_2(k_3)$  will only have the same shape if the desired operator is symmetric. The weighted least-squares optimised operator (solid line) is a very good approximation of the desired operator, it nicely follows the smooth behaviour. Zooming in around amplitude equal to one in Figure 5.17b, it is clear that this asymmetric operator is much more accurate than its truncated equivalent. The maximum amplitude has been limited to 1.00015, an error that is more than 30 times smaller. The phase of the wavenumber spectrum of the asymmetric operator is shown in Figure 5.17d. The accuracy in the optimised wavenumber range has improved slightly. But since truncation had less effect on the phase, so has the optimisation.

In applications where only a limited number of receivers is available, this asymmetric short spatial operator will certainly improve the results. In cases where a short operator is needed to limit computation time, it can usually be designed symmetrically. However, there are several situations for which asymmetric operators could still be preferred, like anisotropic media with a tilted symmetry axis [Zhang et al., 2001] or elastic wavefield decomposition.

### 5.2.3.1 Wavenumber range

For the symmetric short operators, criteria were proposed to help selecting the best wavenumber range for the application. For asymmetric operators, the same criteria can be applied. There is however a much larger set of possible intervals since both  $|k_3^-|$  and  $k_3^+$  can vary independently from zero to  $k = \omega/c$ , related to the output point of the asymmetric operator. This is shown in Figure 5.18 for spatial operators optimised at  $x_3^{(-3)}$  with the same configuration properties and weight as mentioned before. Notice that on the right horizontal axis  $-k_3^-$  is plotted instead

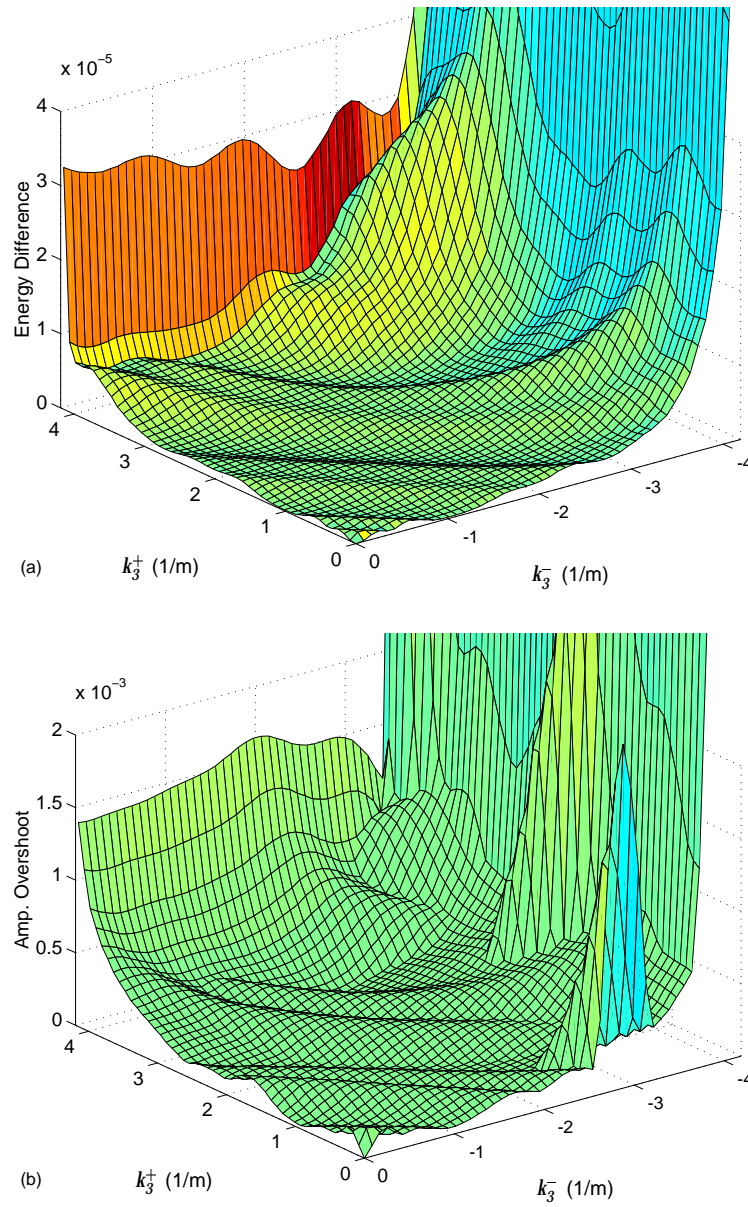


**Figure 5.18:** Energy difference (a) and maximal amplitude overshoot (b) for 15-points operator at  $x_3^{(-3)}$  in function of wavenumber optimisation interval

of  $k_3^-$ . In Figure 5.18a, the energy difference  $E_{diff}$ , defined earlier in Equation (5.35), can be observed. Figure 5.18b shows the maximum amplitude overshoot above one  $A_{max}$ . Except for some peaks in the amplitude plot, both criteria have a similar general behaviour. There is an overall increase towards higher wavenumbers. The undulations that were present in the curves for the symmetric operators on the diagonal line  $-k_3^- = k_3^+$  reappear. The asymmetry of the operator design is visible in these surface plots also. As mentioned before, the negative extrapolation angle has become smaller while the positive angle is now larger compared to the symmetric situation because of the relative position of  $x_3^{(-3)}$ . This is reflected in Figure 5.18. Both the energy difference  $E_{diff}$  and the maximum amplitude  $A_{max}$  increase with decreasing  $k_3^-$  and become relatively high when  $k_3^-$  approaches  $k$ , with values up to  $1.5 \cdot 10^{-4}$  for  $E_{diff}$  and 0.16 for  $A_{max}$ . For the energy difference, it is a smooth increase. The amplitude overshoot stays rather small until  $k_3^-$  comes close to  $-k$  and then it suddenly jumps to the high values. For output points  $x_3^{(i)}$  where  $i < 0$  (points deeper than  $x_3^{(0)}$ ), it would be logical to design an operator with wavenumber range  $|k_3^-| < k_3^+$  and therefore these high values are not considered meaningful. When  $i > 0$  (points above  $x_3^{(0)}$ ) the interval would be such that  $|k_3^-| > k_3^+$ . An operator designed for data point  $x_3^{(i)}$  with a wavenumber interval  $(k_3^-, k_3^+)$  can be obtained by mirroring the operator for data point  $x_3^{(-i)}$  within wavenumber interval  $(-k_3^+, -k_3^-)$ , in  $x_3^{(0)}$ . This means that mirroring the energy difference plot and the maximum amplitude plot for  $x_3^{(-i)}$  in  $|k_3^-| = k_3^+$  will give the results for  $x_3^{(i)}$ .

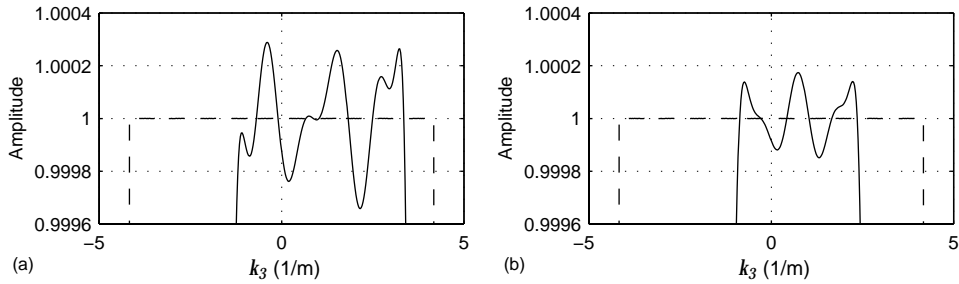


**Figure 5.19:** Influence of the wavenumber optimisation interval on the wavenumber spectrum of a 15-points asymmetric operator:  $k_3^- = -1.2$ ,  $k_3^+ = 3.5$  (a),  $k_3^- = -1$ ,  $k_3^+ = 2.5$  (b) (solid line = optimised operator, dashed line = phase shift operator)

Considering the criteria for  $x_3^{(-3)}$  in Figure 5.18 again, there obviously is a broad

range of acceptable wavenumber intervals. Similar to the symmetric case, an optimal wavenumber range should be decided on, applying a combination of these theoretical criteria and external circumstances of the application. Often, a balance has to be found between accuracy and length of the wavenumber range. The example of Figure 5.17 showed an operator with wavenumber interval ( $k_3^- = -2, k_3^+ = 3$ ). As mentioned before, it has a maximum amplitude overshoot  $A_{max}$  of  $1.5 \cdot 10^{-4}$ . Its energy difference  $E_{diff}$  equals  $1.7 \cdot 10^{-6}$ . To show the influence of the wavenumber range for the asymmetric operator, two other operators are plotted in Figure 5.19. For the plot in Figure 5.19a,  $k_3^+$  has been increased to 3.5 and  $k_3^-$  has been set at -1.2. This operator is located at a local maximum in both selection criteria with an energy difference  $E_{diff}$  of  $3.9 \cdot 10^{-6}$  and a maximum amplitude overshoot  $A_{max}$  of  $2.9 \cdot 10^{-4}$ , both about twice as high as those of the first operator. In Figure 5.19b an operator with a much smaller wavenumber interval is optimised. It goes from  $k_3^- = -1$  to  $k_3^+ = 2.5$ . Its maximum amplitude overshoot  $A_{max}$  of  $1.7 \cdot 10^{-4}$  is a little higher than that of the operator in Figure 5.17d. It does however have a slightly lower energy difference  $E_{diff}$  of  $1.5 \cdot 10^{-6}$ . While  $A_{max}$  gives an indication of the stability of the operator,  $E_{diff}$  tells more about the average accuracy. Not only the amplitudes larger than one have an influence on the energy difference, but also the deviations lower than one. The negative peak in the wavenumber spectrum of Figure 5.17d therefore causes the higher energy difference for this operator. Besides the amplitude, the phase of the wavenumber spectrum also has an influence on the energy difference. These examples show again that different criteria can lead to different wavenumber ranges and therefore it is good to take a combination of criteria to determine the best operator for the application.

### 5.2.3.2 Output points

The examples in the previous section all discussed an asymmetric 15-points operator, designed for output point  $x_3^{(-3)}$ . When processing a data set with 15 receivers, a new operator will have to be designed for each  $x_3^{(i)}$  output point. With each position, new conditions are set for the optimisation. Two short operators, with the same wavenumber range, but another output point will therefore not have the same wavenumber spectrum. This also leads to different results for the energy difference and maximum amplitude criteria. Figure 5.20 shows both plots for operators with output point  $x_3^{(-5)}$ . Its spatial position is indicated in Figure 5.16. The general trend of both criteria is similar to that in Figure 5.18. The main difference is the slope of the increase of both the energy difference and the amplitude overshoot. Apart from the undulations, Figure 5.18a and b have a rather flat surface until a relatively low

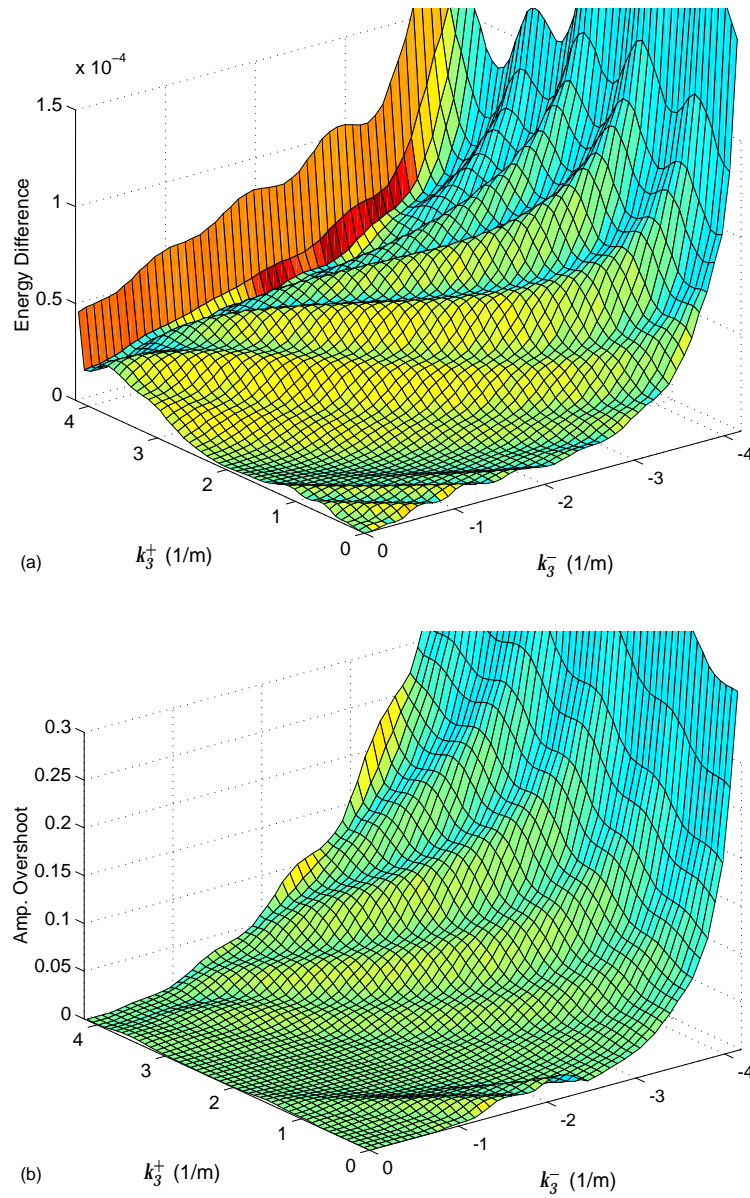


**Figure 5.20:** Energy difference (a) and maximal amplitude overshoot (b) for 15-points operator at  $x_3^{(-5)}$  in function of wavenumber optimisation interval

$k_3^-$ . Since  $x_3^{(-5)}$  is at a larger distance from  $x_3^{(0)}$  than  $x_3^{(-3)}$ , an extrapolation operator would logically be more optimally designed in a wavenumber range that is shifted even more towards positive wavenumbers. This causes the plots in Figure 5.20a and b to start increasing for higher  $k_3^-$  already.

It is also important to notice that the average energy difference and amplitude overshoot for  $x_3^{(-5)}$  are higher than those for  $x_3^{(-3)}$ . The vertical scales in Figure 5.20 are much larger. This indicates that the average stability and accuracy of the short operator decreases with its asymmetry. This is supported by the results in Figure 5.21 which show the energy difference and the maximum amplitude overshoot for output point  $x_3^{(-7)}$ , the most outer point. Operators having a wavenumber range with a high  $k_3^-$  and  $k_3^+$  value will still have a reasonable energy difference with the phase-shift operator. Their amplitude overshoot in that range on the other hand, will be unacceptably large and is even worse for other wavenumber intervals. Besides the common increase towards  $|k|$ , the energy difference also contains rather high peaks for very small intervals around  $k_3 = 0$ . Since the amplitude overshoots decrease in that range, this indicates large negative deviations from the amplitude of the wavenumber spectrum of the phaseshift operator or a bad approximation of the phase.

An example of a short operators for output point  $x_3^{(-5)}$  is given in Figure 5.22. The spatial operator in Figure 5.22a has its peak value at  $x_3 = x_3^{(-5)}$  and goes smoothly to zero. It is designed to have an accurate wavenumber spectrum in the specified interval. The maximum amplitude overshoot of  $9.2 \cdot 10^{-4}$  in Figure 5.22b is higher than for output point  $x_3^{(-3)}$  (see Figure 5.20). The energy difference with the phase-shift operator is  $1.4 \cdot 10^{-4}$ . The weight used in designing this operator is still set at  $5 \cdot 10^{-5}$ . As mentioned before for the symmetric operator, the weight can be varied in the asymmetric case also to control the amplitude. But again the behaviour in the evanescent field has to be monitored to prevent the operator from becoming unstable. The stability of the phase of the wavenumber spectrum in Figure 5.22c remains very high in the specified interval. In the evanescent field, the phase becomes rougher.

While the operator output point  $x_3^{(-5)}$  is still controllable, for point  $x_3^{(-7)}$  the instability of the operator becomes too high. This can be seen in the example of Figure 5.23. As expected, the spatial operator has its peak value at  $x_3 = x_3^{(-7)}$ . This is also the outmost point of the operator, which obviously has a large influence

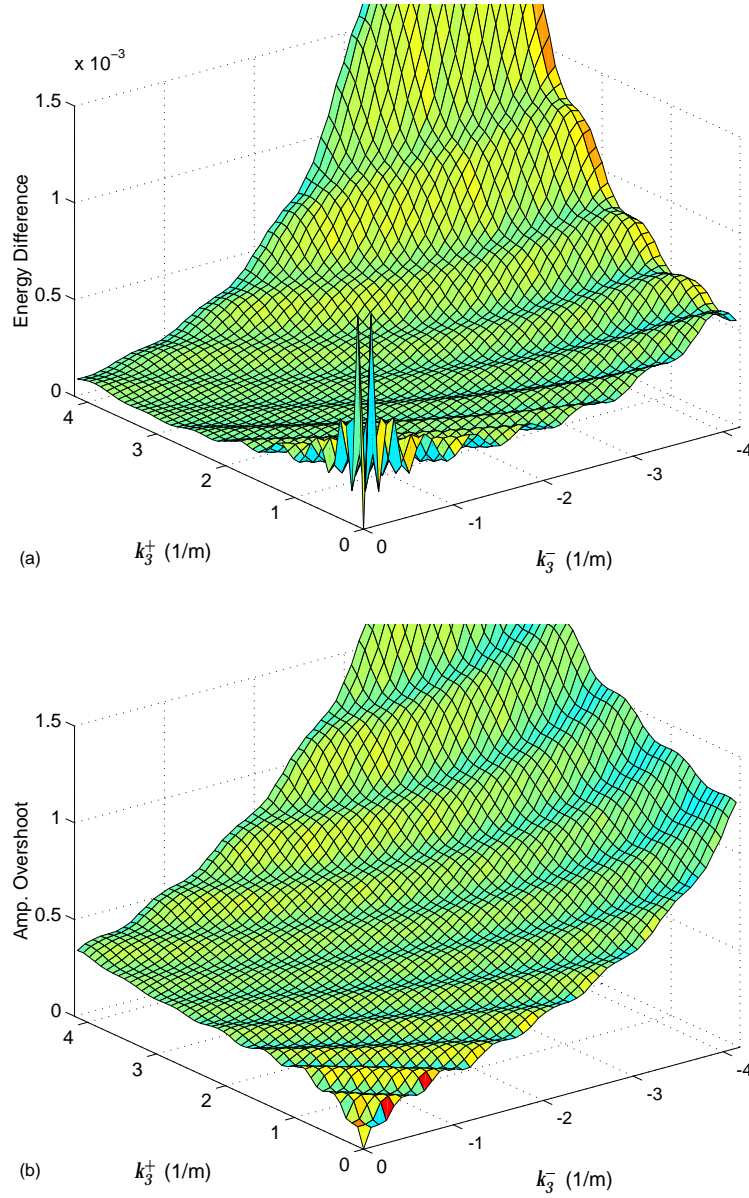


**Figure 5.21:** Energy difference (a) and maximal amplitude overshoot (b) for 15-points operator at  $x_3^{(-7)}$  in function of wavenumber optimisation interval (note scale difference with Figure 5.20)

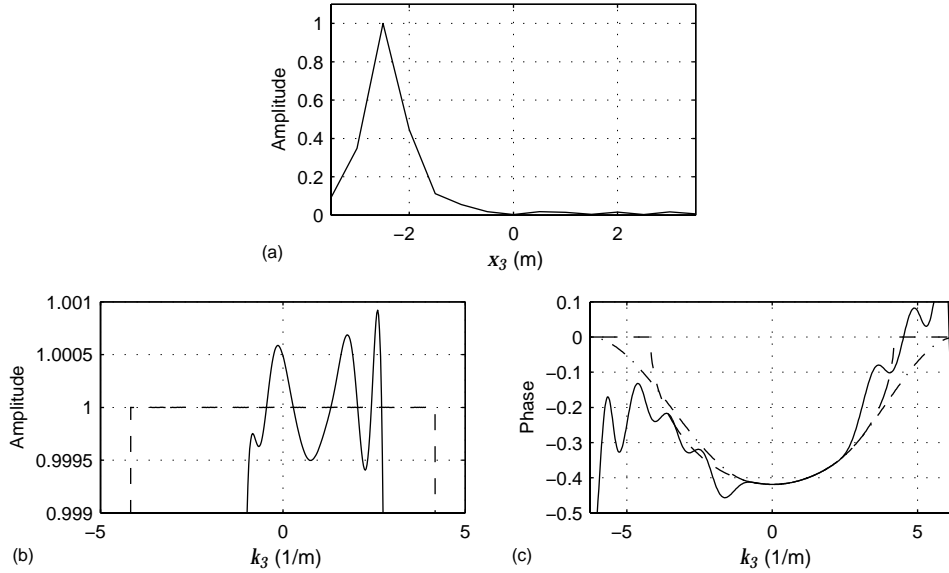


**Figure 5.22:** Asymmetric 15-points operator designed with weighted least-squares optimisation at  $x_3^{-5}$  with  $k_3^- = -0.85$ ,  $k_3^+ = 2.5$  in the spatial domain (a) and amplitude (b) and phase (c) in the wavenumber domain (solid line = optimised operator, dashed line = phase shift operator)

on the transformation to the wavenumber domain. The wavenumber spectrum in Figure 5.23b is rather accurate in the given range. It has an acceptable energy difference of  $2.2 \cdot 10^{-4}$ . But once  $k_3$  is smaller than  $k_3^-$ , a huge overshoot appears in the amplitude, resulting in an operator which is far from stable and would cause large artefacts when applying it in a recursive extrapolation scheme. In this case, the amplitude even goes up to 1.31. Also the phase in Figure 5.23c deviates largely from the desired operator outside the specified wavenumber range.

In a simple example, it can be demonstrated why stable extrapolation of the outmost points of a small data set is not evident. A line of 1000 receivers with a spacing of 0.1 m is considered,  $x_3$  ranging from -50 to 50 m. Figure 5.24a shows the Green's functions which should be used to extrapolate a source signal from a source located at  $x_3 = -40$  over an extrapolation step of  $\Delta x_1 = 0.1$  m. Only the leftmost 30 m and the first 0.1 s of the data are plotted. The left side is cut off at  $x_3 = -50$  m. If the Fourier transform of this Green's function is taken (Figure 5.24b), the wavenumber spectrum for  $f = 100$  Hz clearly resembles the phaseshift operator. This spectrum will be more accurate the more the source position is moved to the middle of the

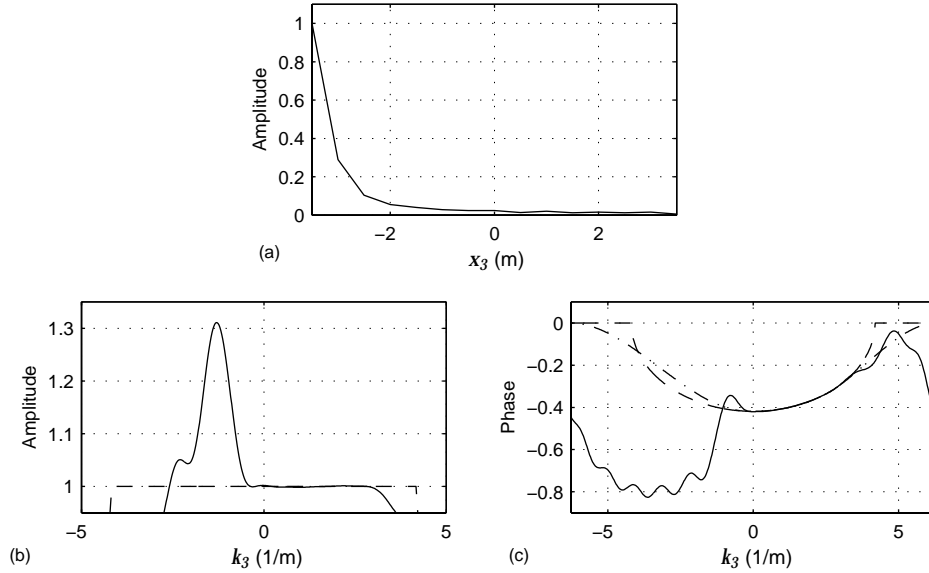


**Figure 5.23:** Asymmetric 15-points operator designed with weighted least-squares optimisation at  $x_3^{-7}$  with  $k_3^- = -0.3$ ,  $k_3^+ = 3.0$  in the spatial domain (a) and amplitude (b) and phase (c) in the wavenumber domain (solid line = optimised operator, dashed line = phase shift operator)

data set.

The same procedure is followed for the plots in Figures 5.24c and d where the source is placed at  $x_3 = -48$ . Since the source is moved more to the side of the data set, the extrapolation hyperbole is truncated more. Its right side is still shown completely, but most part of its left side is no longer present. This has an influence on the wavenumber spectrum. It still looks like the phaseshift operator but has become less stable.

Finally the source is put at  $x_3 = -50$ , at the edge of the data set, coinciding with the outmost receiver. Only the right part of the Green's function is still present in the data of Figure 5.24e. No information of the left part is available. This has an extreme effect on the wavenumber spectrum as can be seen in Figure 5.24f. This is the spectrum of the Green's function that should be used to extrapolate a source signal at this position over  $\Delta x_1 = 0.1$  m. There is no resemblance with the original phase-shift operator at all. This example shows that the phaseshift operator is not a good input for the approximation scheme in order to design an accurate asymmetric extrapolation operator for the outmost points of a data set. However, application of the operator in Figure 5.24f in a recursive extrapolation scheme would also lead to incorrect results. The operator is not unstable but its amplitude is much smaller

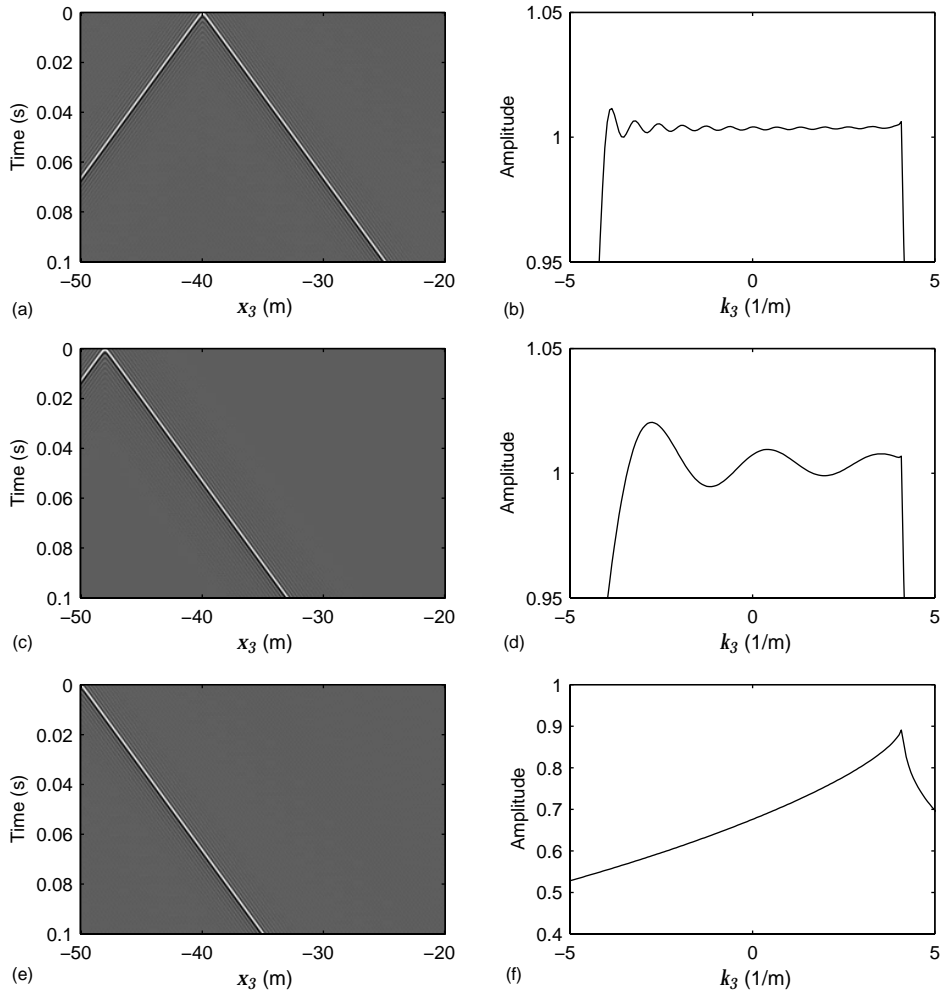


**Figure 5.24:** Influence of source position on the amplitude of the extrapolation operator in the wavenumber domain

than one. In a recursive scheme, this would cause the data to get damped more and more in each extrapolation step. For higher frequencies, the wavenumber spectrum of the Green's function does become unstable which will make the data blow up for these frequencies. The amplitude of one is what makes the phaseshift operator the appropriate input for recursive migration techniques.

In order to reduce the instability of the operator for  $x_3^{(-7)}$  as shown in Figure 5.23,

the weight could be adjusted. A higher weight factor would lower the amplitude peak. At the same time it would however have a negative effect on the accuracy of the operator within the indicated wavenumber range. Any changes in the weight should be carefully monitored in all relevant criteria. Using a constant weight factor for the extrapolation of an entire data set would be the most straightforward approach. But setting different weights depending on the output point will be necessary for the stability of the migration.

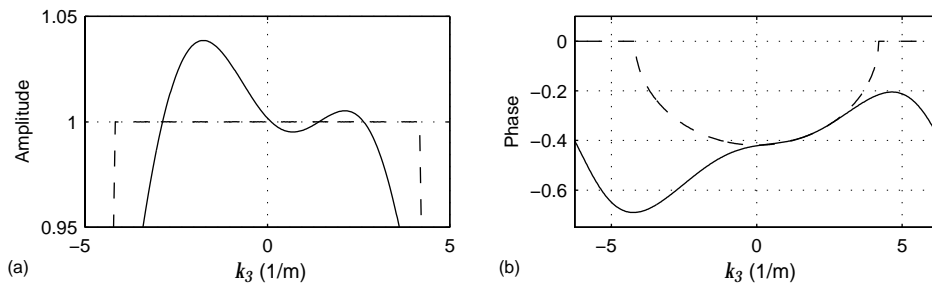


**Figure 5.25:** Amplitude (a) and phase (b) of 3-points asymmetric operator designed with weighted least-squares optimisation at  $x_3^{-1}$  with  $k_3^- = -0.3$ ,  $k_3^+ = 3.0$  in the wavenumber domain (solid line = optimised operator, dashed line = phase shift operator)

Another approach to improve the stability of the migration would be to make extra short operators for the outmost traces of the data set. The amplitude and phase of a 3-points operator, designed with the same parameters as the longer 15-points operator, is plotted in Figure 5.25. The large amplitude peak that was visible in Figure 5.23 has become much smaller. The accuracy in the interval  $(k_3^-, k_3^+)$  has decreased. Applying this operator for the 2 outmost points  $x_3^{(-7)}$  in Figure 5.16, and the symmetric 3-points operator for  $x_3^{(-6)}$ , results in a more stable extrapolation for each subsequent recursion step and therefore a stable overall migrated data set.



## Operator Performance in Recursive Extrapolation

---

*Migration of a data set requires forward extrapolation of the source signal and inverse extrapolation of the recorded data. Short asymmetric spatial extrapolation operators have to take into account the specific situation for tunnelling applications, where only a limited number of receivers is available. Their performance in both forward and inverse extrapolation is investigated and compared with short symmetric spatial extrapolation operators in similar conditions.*

In the previous chapter, short symmetric extrapolation operators were designed to limit computation time. For some special cases, where only a small number of receivers or soil layers with a tilted symmetry axis are present, new asymmetric operators were developed. It was shown how a combination of theoretical and external criteria determine the best wavenumber range of an extrapolation operator for a certain application. Extrapolation is however not performed for one single frequency but for a range of frequencies. In the wavenumber domain, the transition to the evanescent field at  $k$  depends on the frequency as  $k = \omega/c = 2\pi f/c$ . Therefore, instead of setting a wavenumber range  $(k_3^-, k_3^+)$  for each  $x_3$  position, a fixed operator angle range  $(\alpha_3^-, \alpha_3^+)$  is chosen with  $\sin \alpha_3 = k_3/k$ .

In case a symmetric operator is used for the migration of a large data set, only one operator has to be designed for each frequency, meaning only one  $\alpha_3$  has to be set. When asymmetric operators are applied, a range of wavenumbers has to be determined for each  $x_3$  position. This can be done manually by inspecting the behaviour of the operator as function of the maximum propagation angle  $\alpha_3$ . In this thesis is chosen for an automatic method, which takes the requirements of the application

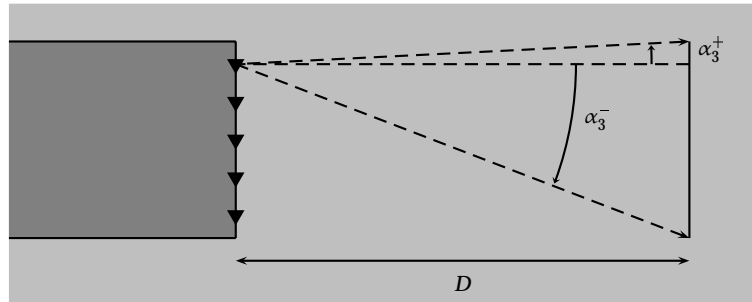


**Figure 6.1:** Determination of optimal angle range  $(\alpha_3^-, \alpha_3^+)$

into account. For example if a set of receivers is installed on the head of a TBM, a minimal distance  $D$  ahead of the system can be determined at which obstacles should be clearly detectable if it is in the path of the TBM, so that measures can be taken with minimal disturbance of the drilling process. This is sketched in Figure 6.1 for a 2-D situation. For each receiver position an angle interval  $(\alpha_3^-$  and  $\alpha_3^+)$  can be calculated so that the entire surface of the tunnel at distance  $D$  of the head is covered. For tunnelling application, it might be useful to choose the angle interval a little bit larger so that not only the exact tunnel surface is considered but also a small area around it. For a regular receiver spacing, there is a sinusoidal dependence between  $\alpha_3$  and  $x_3$ .

The performance in extrapolation of the symmetric and the asymmetric operators is compared for different operator lengths. In a first test, the forward extrapolation is investigated. The inverse extrapolation is analysed in a second test. Both experiments will show different characteristics of the extrapolation operators.

## 6.1 Forward wavefield extrapolation

In the analysis of the forward extrapolation, a source at depth is considered. The source emits a Ricker wavelet, a second derivative of a Gaussian, with a centre frequency of 50 Hz. The Ricker wavelet has a Gaussian frequency spectrum. Both the signal and its amplitude spectrum are shown in Figure 6.2. First, this source signal is extrapolated forward by short symmetric as well as asymmetric spatial operators towards a line with a limited number of receivers. This leads to two different data

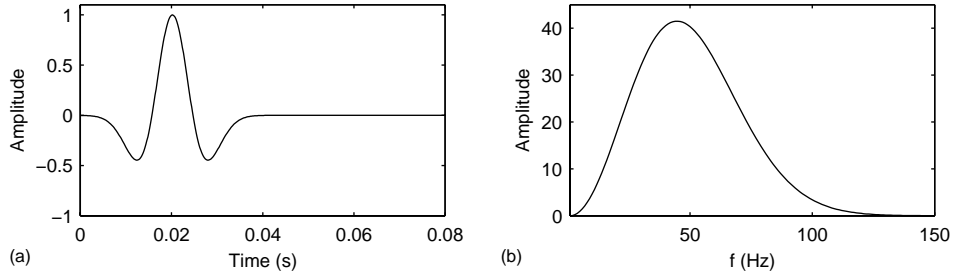


**Figure 6.2:** Source signal: Ricker wavelet (a) and its frequency spectrum (b) with 50 Hz center frequency

sets that could be compared. However, a better indication of the performance of the operators can be given if a comparison could be made with the original input data set, in this case the source wavelet. Therefore, in a second step the extrapolation results are inverse extrapolated, using the same method for both data sets. They are extended with zero traces to large data sets which are then inverse extrapolated with a short symmetric extrapolation operator. Because the inverse extrapolation is carried out in the same way for both data sets, the differences in the final data sets are only due to the forward extrapolation. The final results are compared with the original model, both in the  $(x_3, t)$  and in the  $(k_3, f)$  domain. The accuracy of the reconstructed signals gives an indication of the performance of both the symmetric and the asymmetric operators in the forward extrapolation and shows the effects of the limited number of traces.

The input model for the forward extrapolation is shown in Figure 6.3a. A vertical line of 21 receivers (triangles in Figure 6.3a) with a 0.5 m spacing is considered at  $x_1 = 0$  in a homogeneous background medium which has a wave speed of 150 m/s, a typical shear wave velocity for soft soils. The 21 receivers are placed symmetrically around  $x_3 = 0$ . At this depth, a source (star in Figure 6.3a) is situated at a horizontal distance of 5 m from the receiver line.

Firstly, a forward extrapolation of the source signal is performed with a 21-points asymmetric operator set with extrapolation steps of  $\Delta x_1 = 0.1$  m and the distance  $D$  in front of the TBM (Figure 6.1) set at 5 m. This leads to  $\alpha_3^+ = |\alpha_3^-| = 45^\circ$  for the operator at  $x_3 = 0$ . At the outmost points, the largest operator angle is used,  $\alpha_3^+ = 63^\circ$  at  $x_3 = -5$  ( $\alpha_3^- = -63^\circ$  at  $x_3 = 5$ ). The result is plotted in Figure 6.3b

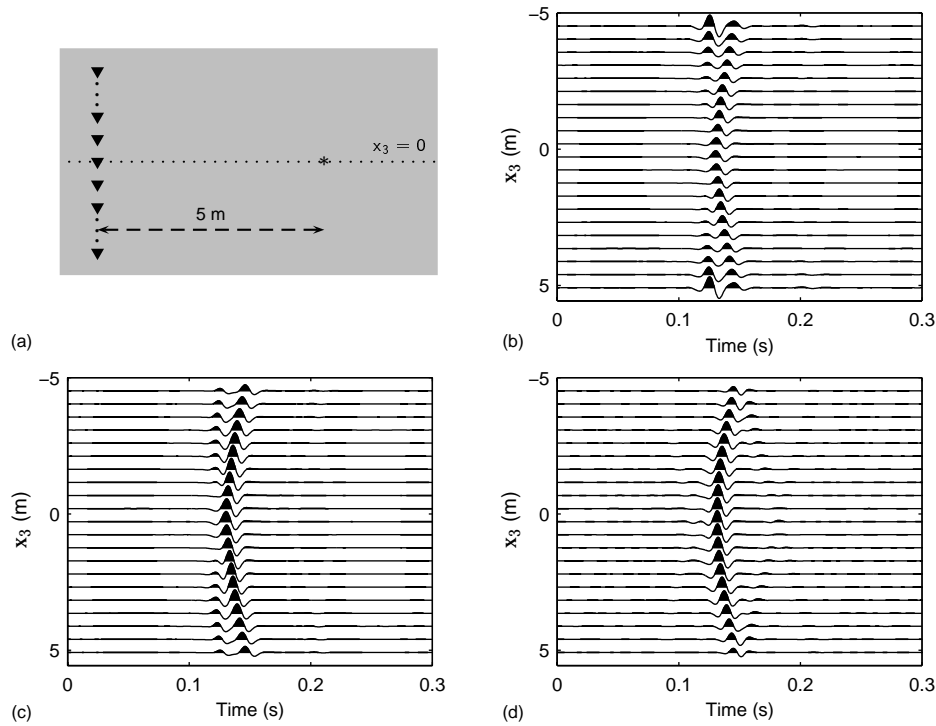


**Figure 6.3:** Input model for forward extrapolation (a), forward extrapolation over 21 traces using 21-points asymmetric operators (b), 21-points asymmetric operators and 3-points operators at edges (c) and 21-points symmetric operators (d)

which clearly shows the effects of the unstable operator for the outmost receivers at  $x_3 = -5$  and 5 m. The artefacts at the edges will be limited after a small number of extrapolation steps but the recursive character of the extrapolation causes them to blow up and penetrate into the data more and more. In this example, the artefacts already have a higher amplitude than the hyperbolic event from the source.

A suggested solution for the instable extrapolation was the use of short operators for the outmost receivers. For the operators that are designed for the traces between  $x_3 = -4$  and 4 m, nothing changes. The operators for  $x_3 = 4.5$  and 5 m, and similarly for  $x_3 = -4.5$  and -5 m, are replaced by 3-points operators centred around  $x_3 = 4.5$  m, with the same design parameters as the original 21-points operators. All other design parameters remain the same. Both sets are much more stable than

the 21-points operators for the respective points. The influence on the forward extrapolation can be seen in Figure 6.3c. There still is some distortion of the data set at the edges, but strongly suppressed compared to the data in Figure 6.3b so that its amplitude is now much smaller than that of the hyperbolic event. It should be mentioned that the amplitude scale in both figures is not equal, all data sets in this chapter are plotted to their maximal amplitude so that the main event can be compared to the noise generated by the extrapolation. The method where the short 3-points operators improve the stability of the extrapolation is applied in all further examples in this thesis.

Figure 6.3d shows the result of forward extrapolation of the source signal with symmetric operators.  $\alpha_3$  is set at  $65^\circ$ , so a larger operator angle than the  $45^\circ$  that is determined for the middle point in case of asymmetric operators, is chosen. This way at least the entire area in front of the TBM is taken into account as was described in Figure 6.1, also for the situation where the outmost points have to be extrapolated. As shown in chapter 5, the symmetric operator will spread over the data and will behave as a truncated operator when it acts outside the range of the 21 traces. In both the asymmetric (Figure 6.3c) and the symmetric (Figure 6.3d) forward extrapolation, the small aperture causes that only the top part of the hyperbolic event is present in the data sets. It appears that the event after symmetric extrapolation gets damped quicker for increasing  $|x_3|$ . By increasing the operator angle, the damping on the hyperbole will decrease. In the symmetric extrapolation, an effect of the limited background model is visible as reflections of the edge of the hyperbole go back into the data.

Since only the effect of the short operators on the forward extrapolation is to be examined in this experiment, both data sets in Figure 6.3 are inverse extrapolated with the same method. On both sides of the data, 190 extra zero traces are added in order to obtain two large data sets with each 401 traces. This avoids that the limited number of traces influences this step of the experiment. In an homogeneous background model, an inverse extrapolation of both data sets is performed, using the 21-points symmetric operator. In the forward extrapolation, a data set of only 21 traces is used as input; outside this range no data is present at all. In the inverse extrapolation, 401 traces are used as input, although most of the traces are zero, and the symmetric operator will spread out the energy over the entire data range. . The inverse extrapolation of the asymmetric and symmetric extrapolated data leads to the results in Figure 6.4 where only the middle 21 traces are plotted. Figure 6.4a shows the inverse extrapolation of Figure 6.3c, where the asymmetric operators

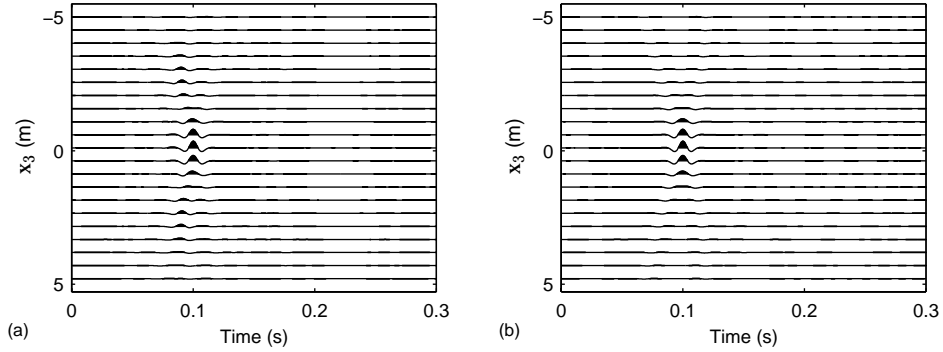


**Figure 6.4:** Inverse extrapolation of data sets in Figure 6.3 extended to 401 traces (asymmetric (a) and symmetric result (b)), with 21-points symmetric operators

were used. The effect on the data in Figure 6.3d, which was obtained with symmetric operators, is plotted in Figure 6.4b. The reconstructed source signal itself is almost equal in the two figures. It does not focus into one single pulse at  $x_3 = 0$ , but the energy is smeared mainly over the three middle traces, due to the limited range of receivers used. The resolution in the  $x_3$  direction will increase with the number of receivers. The side effects of the extrapolation are visible as tails on the reconstructed source signal, which are stronger in the asymmetric case. In both cases however, the average signal-to-noise level is relatively high.

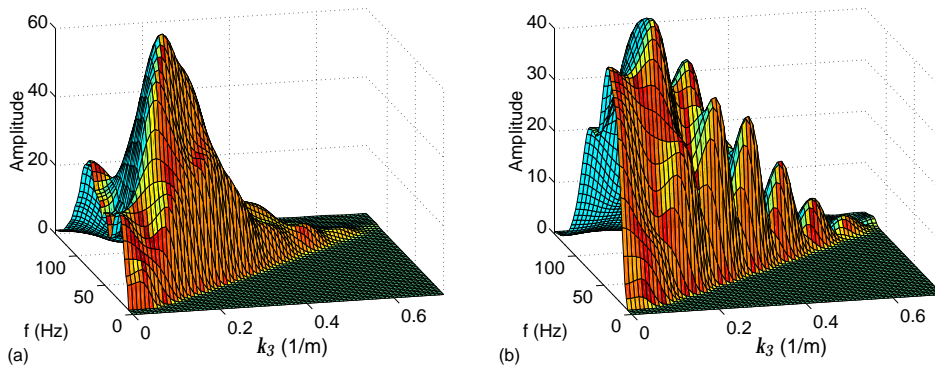


**Figure 6.5:**  $(k_3, f)$  amplitude spectra of the data sets in Figure 6.4 (asymmetric (a) and symmetric (b))

Another way to compare both data sets is by their respective  $(k_3, f)$  spectra in Figure 6.5. Since the  $(k_3, f)$  spectrum is symmetric over  $k_3 = 0$ , only positive wavenumbers are shown. The most obvious difference between both plots is the smooth behaviour of the spectrum in the asymmetric case in Figure 6.5a versus the more irregular spectrum of the symmetric case in Figure 6.5b. In Figure 6.5a, the typical frequency spectrum of a Ricker wave can still be recognized for each wavenumber. The spectrum in Figure 6.5b is much more distorted. It is more irregular and the amplitude decay with  $k_3$  is much less smooth. The symmetric extrapolation also caused a larger overall decrease of the amplitude of the spectrum. Combination of the results in Figure 6.4 and Figure 6.5 shows that after asymmetric and symmetric forward extrapolation the source signal can be very well reconstructed. The symmetric extrapolation introduces more distortion of the spectrum.

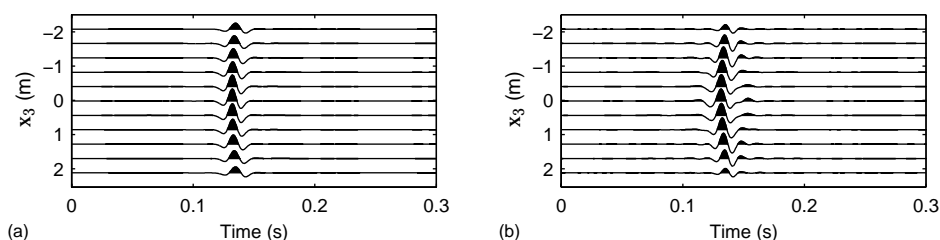


**Figure 6.6:** Forward extrapolation over 11 traces using 11-points asymmetric operators with 3-points operators at edges (a) and symmetric operators (b)

The same experiment is repeated with a line of only 11 receivers that are symmetrically placed around  $x_3 = 0$ . The forward extrapolation is performed with 11-points asymmetric versus symmetric operators. All parameters in the modelling remain the same. In the symmetric case, an operator angle of  $\alpha_3 = 45^\circ$  is used, the maximal angle determined for the asymmetric operators. The 11-points operators for the outmost points will again lead to unacceptable artefacts and therefore 3-points operators are applied in a similar way as described for the previous example. In Figure 6.6, after the forward extrapolation, it can be seen that because of the decrease of the aperture, less of the hyperbolic character of the event is present in either data set. The symmetric extrapolation in Figure 6.6b is again damped stronger as a function of  $|x_3|$ . The side effect of the limited background model distorts the data more than in the example with 21 traces. The asymmetric extrapolation shows fewer artefacts at the outmost traces. The signal-to-noise level is low in both data sets, but smaller for the asymmetric extrapolation.

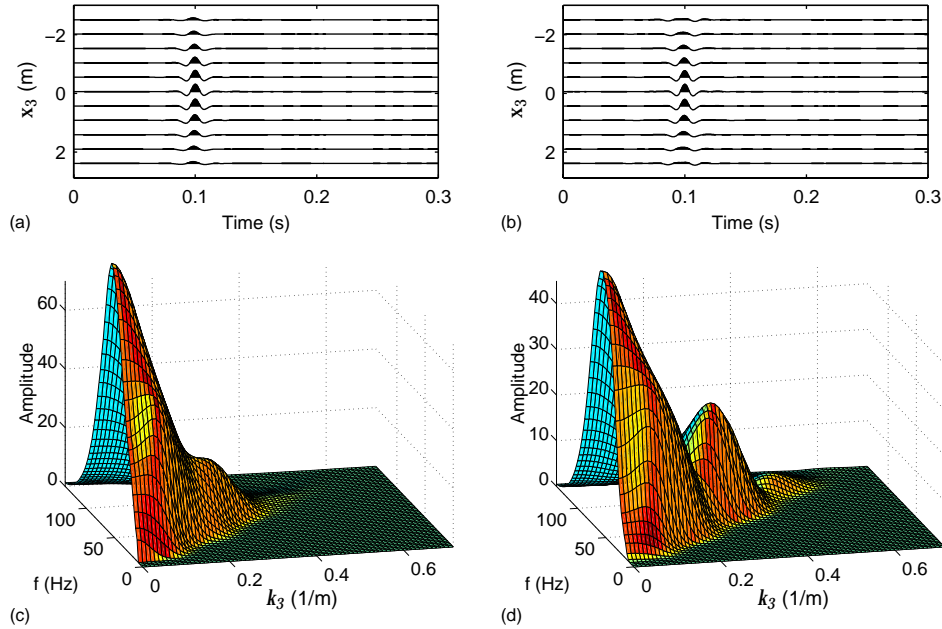


**Figure 6.7:** Inverse extrapolation of data sets in Figure 6.6 extended to 401 traces, with 11-points symmetric operators in the  $(x_3, t)$  (asymmetric (a) and symmetric (b)) and the  $(k_3, f)$  domain (asymmetric (c) and symmetric (d))

Figure 6.7 shows the inverse extrapolation of the two data sets after extending to 401 traces, both in the  $(x_3, t)$  and the  $(k_3, f)$  domain. In the spatial domain, only the 11 middle traces are plotted. To perform the extrapolation, the 11-points symmetric operator set is now shifted over the 401 traces for both cases. Because of the smaller number of receivers, the resolution in the  $x_3$  direction has become worse compared to the 21-points example both for the asymmetric extrapolation in Figure 6.7a and the symmetric extrapolation in Figure 6.7b. The resolution of the symmetric example seems to be better. But considering the almost plane wave event in Figure 6.6, the resolution can not be that good and the asymmetric result resembles better the true resolution for the 11 receivers used. Still, even with the limited aperture both extrapolation methods result in a good reconstruction of the source signal. The symmetric extrapolation again causes a more irregular wavenumber spectrum and a decrease of its amplitude as can be seen in Figure 6.7.

## 6.2 Inverse wavefield extrapolation

In a second set of tests, the performance of the operator in inverse extrapolation is investigated. The basic principles are the same as in the previous section. A data set with a small number of traces and containing a hyperbolic event is inverse extrapolated with the use of short asymmetric as well as symmetric operators. Then the data sets are extended to a large number of traces and the same forward extrapolation is carried out on both data sets. The performance of the inverse extrapolation and the effect of the limited number of receivers are discussed by comparing the reconstruction of the event in both data sets.

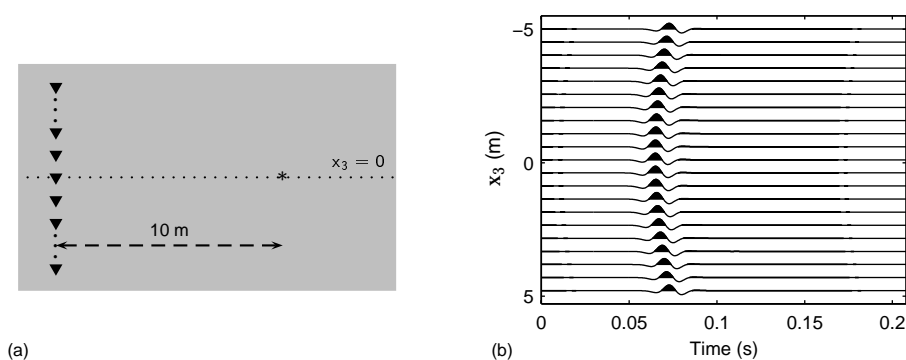


**Figure 6.8:** Input model for inverse extrapolation (a), input data with 21 traces (b)

The recording in Figure 6.8 is modelled with a line of 21 receivers at a 0.5 m spacing in a homogeneous background of 150 m/s. A source at  $x_1 = 10$  m from the receiver line and at the spatial position  $x_3 = 0$  emits a Ricker wavelet. Because of the small aperture of 10 m, only the top part of an hyperbolic event is visible in the  $(x_3, t)$  plot. Outside this range, no data is recorded.

For the first step, a homogeneous velocity model with the same  $x_3$  range as the recording in Figure 6.8 is considered. The same 21-points asymmetric and symmetric operator sets that were described in the previous section are used in these experiments, but now for inverse extrapolation. A total extrapolation step of 10 m is carried out with recursive extrapolation steps of 0.1 m, bringing the event to  $t = 0$ . This is shown in Figure 6.9.

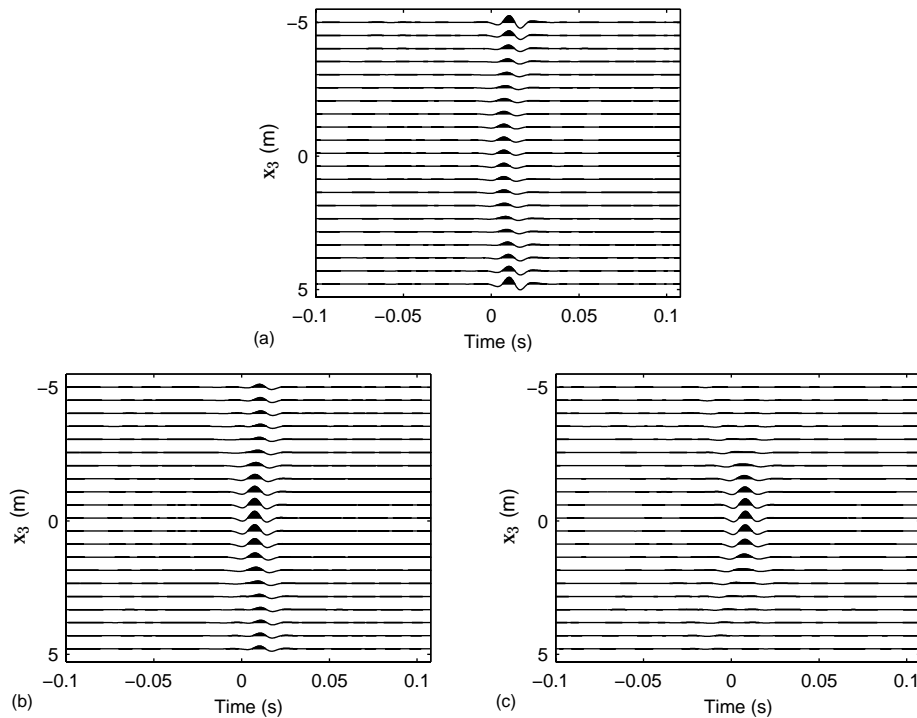


**Figure 6.9:** Inverse extrapolation of data in Figure 6.8a using 21-points asymmetric operators (a), 21-points asymmetric operators and 3-points operators at edges (b) and 21-points symmetric operators (c)

Firstly, the asymmetric extrapolation is performed with 21-points operators over the entire receiver range. Figure 6.9a clearly shows the negative influence of the instable operators for the outmost traces. Just like in the forward extrapolation, the recursive character of the method causes the artefacts to blow up and dominate the data set. In migration, a forward extrapolation of the source signal and an inverse extrapolation of the recorded data will be carried out and those will be correlated for each recursive step. When these distortions line up in the correlation, they will be amplified and hide the real events in the data.

In order to decrease the side effects of the asymmetric extrapolation, the option of applying short 3-points operators for the outmost points is chosen here also. The result can be seen in Figure 6.9b. The artefacts are highly damped now and the extrapolated wavefield is visible at  $t = 0$ . Because of the limited aperture, the hyperbole can not be brought back to a single pulse. The main energy is spread

over the 5 middle traces. This is also the case for the extrapolation with symmetric operators in Figure 6.9c. The distortion caused by the asymmetric extrapolation is focussed in the outmost traces and is stronger than the side effects of the symmetric extrapolation.

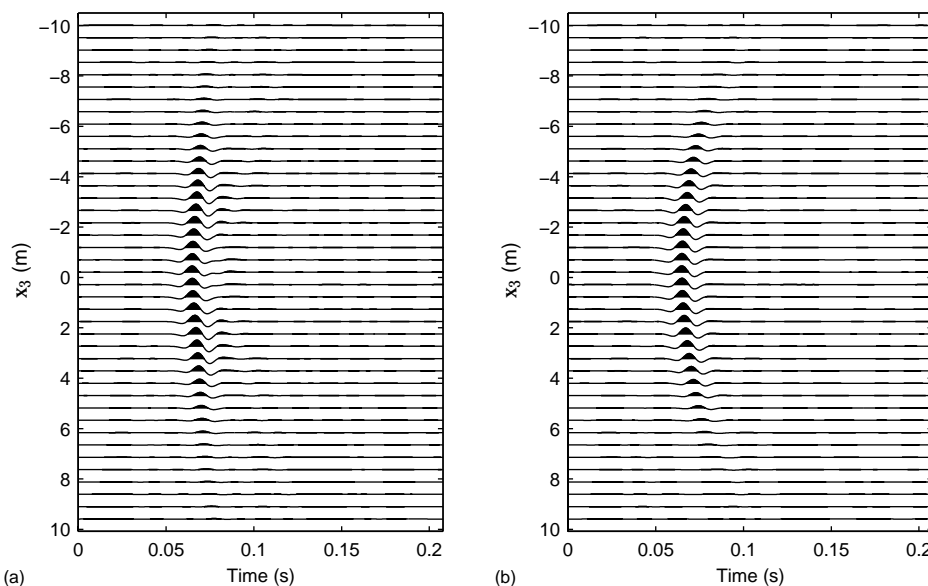


**Figure 6.10:** Forward extrapolation of data sets in Figure 6.9 extended to 401 traces, with 21-points symmetric operators, asymmetric (a) and symmetric result (b)

In the second step, the data sets in Figure 6.9b and c are extended to 401 traces by adding zero traces on both sides. Then they are both extrapolated forward with the symmetric 21-points operators. The final results are shown in Figure 6.10. Here the middle 41 traces are plotted so it can also be investigated how the operators spread the energy outside the range of the original data set. For the event itself, it can be observed that after the symmetric extrapolation the hyperbolic character in Figure 6.10b is reconstructed better than after the asymmetric extrapolation in Figure 6.10a. This is caused by the side effects in the first step of the experiments where the result of the symmetric extrapolation is more focussed. Both hyperboles are damped much faster as a function of  $|x_3|$  than the input data. They both continue with low energy outside the  $(x_3 = -5, x_3 = 5)$  interval where originally no data was present. By changing the operator angles, the damping can be influenced. But when applying a similar range of angles in both methods, the effect on the in-

verse extrapolation will always be of the same level. Both experiments show a very good reconstruction of the wavelet of the original event.

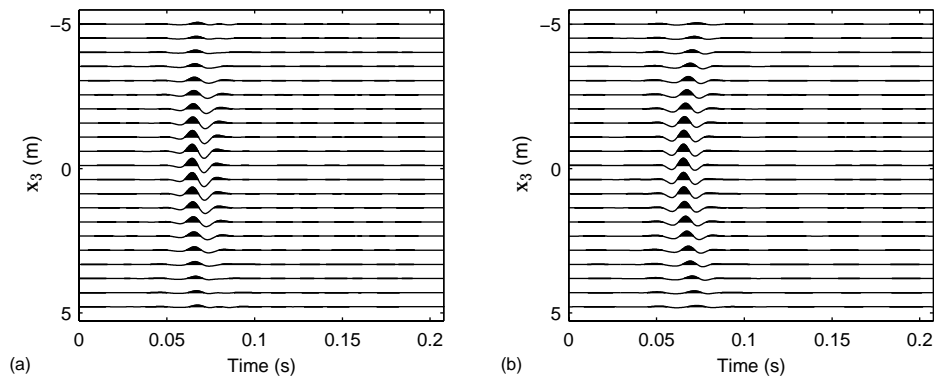


**Figure 6.11:** Result of inverse extrapolation of 11 middle traces of data set in Figure 6.8 with 11-points asymmetric operators and 3-points operators at edges (a) and symmetric operators (b) followed by forward extrapolation of data extended to 401 traces with 11-points symmetric operators

This test is also repeated for a recording with 11 receivers. This means that only the interval ( $x_3 = -2.5$ ,  $x_3 = 2.5$ ) of Figure 6.8 is taken for the inverse extrapolation so that the hyperbolic effect of the event in the data is limited more. For the inverse extrapolation with asymmetric operators, the short 3-points operators at the out-most traces ensure the stability of the recursive steps. Inverse extrapolation of the small data set, followed by the forward extrapolation of the extended data set with symmetric 11-points operators leads to the results in Figure 6.11a for the asymmetric and Figure 6.11b for the symmetric case. In both plots, the events again get damped more than the original hyperbole, but the energy is stronger outside the range of the receivers after the symmetric extrapolation. After the symmetric extrapolation the hyperbolic character of the event is better reconstructed.

## Recursive Migration of Tunnelling Configurations

---

*Also in migration, the asymmetric and symmetric operators are applied and compared with the more traditional migration methods. Different configurations are used: changing the shape of the obstacle or the properties of the background. Also the influence of the propagation of the TBM on the imaging is tested.*

In this chapter, the migration of data in some specific tunnelling situations is discussed. The main set-up of the examples consists of a TBM with a diameter of 10 m, with its centre located at 15 m depth. In the 2-D configuration, 21 receivers are considered to be located on a vertical line with a 0.5 m spacing. The TBM is situated in a homogeneous background with a velocity of 150 m/s, a typical shear wave velocity for soft soils. The source emits the same Ricker wavelet used in chapter 6 with a centre frequency of 50 Hz (Figure 6.2). As mentioned before, in all examples with asymmetric operators, the stability of the migration is assured by using 3-points operators for the outmost data traces.

When modelling the input data sets, the entire wavefield (direct and reflected waves) is calculated. The reflected energy is most important in these examples. Therefore the incident wavefield, travelling directly from the source to the receivers, is calculated separately in a homogeneous model and afterwards subtracted from the initial data set.

## 7.1 Boulder in the path of the TBM

In a first model, a boulder is located in the path of the TBM, at 17 m depth, which is 2 m off-centre. A sketch of the model is shown in Figure 7.1a. The boulder is represented by a square with 1 m long sides at a distance of 10 m from the TBM. The earth surface is not taken into account in this example. It is assumed that the properties of the soil continue for  $x_3 > 0$ . This means that there is no reflector present at  $x_3 = 0$  and the boulder is the only heterogeneity in the model. Consequently, the result of the forward modelling in Figure 7.1b only shows one event, the direct reflection from the boulder.

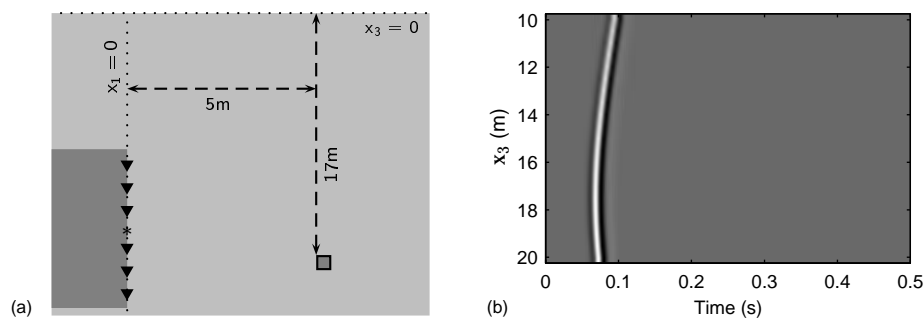


**Figure 7.1:** Model with boulder in the path of the TBM and source and receivers on the head of the TBM (a) and modelled data set (b)

The data in Figure 7.1b is migrated with four different methods so their performance can be compared. In Figure 7.2a an ideal migration is simulated. As input, the data is modelled for 401 receivers instead of 21, keeping the 0.5 m spacing. This way, the entire reflection hyperbole is present in the data and the migration of this data set obviously gives the most accurate result. The migration is performed in the spatial domain with 21-points symmetric operators that are shifted over the data. A focussed event is visible at a distance of 5 m from the receiver line, between  $x_3 = 17$  and 18 m. The migration is not exact though since there are still some artefacts at the edges of the reflection.

In Figure 7.2b, a standard phaseshift migration of the data set with 21 traces is performed in the wavenumber domain. This migration clearly generates the most overall noise. Also the energy from the boulder is cluttered. For a model with more reflectors, the noise would distort the data much more. The noise is mainly gener-

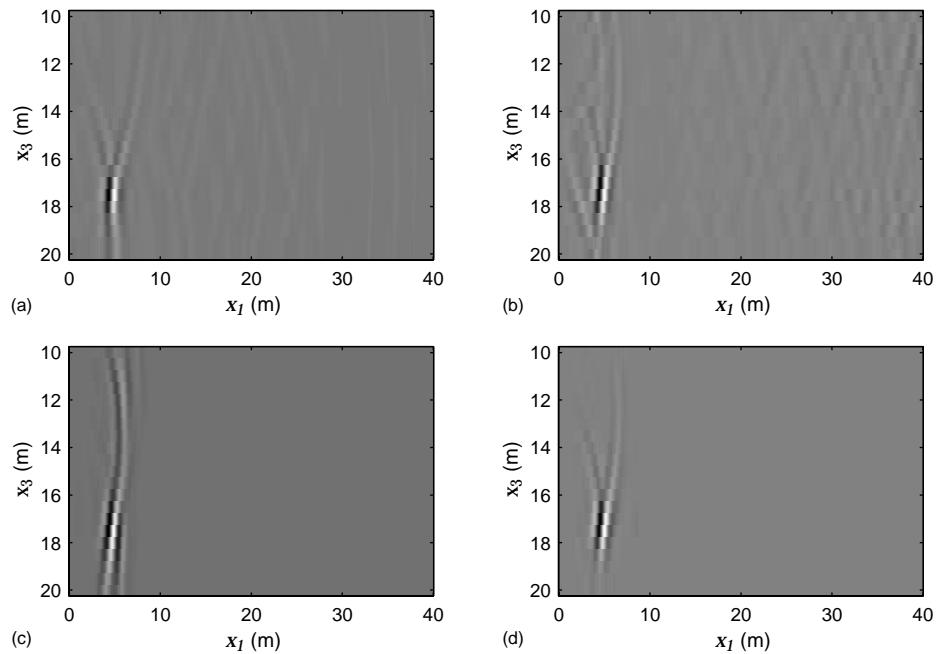


**Figure 7.2:** Migration of data set in Figure 7.1b modelled over 401 traces using 21-points symmetric spatial operators (a), modelled over 21 traces using phase shift migration in the wavenumber domain (b), asymmetric spatial operators (c), symmetric spatial operators (d)

ated by the Fourier transforms to the wavenumber domain and back.

Figures 7.2c and d show the result of migration of the data set with 21 traces in the spatial domain with asymmetric and symmetric extrapolation operators. They both focus the boulder with maximum amplitude at its correct position. Compared to the more ideal situation in Figure 7.2a, the resolution has decreased in both cases, effects are still visible at more shallow depths. The resolution in the  $x_3$  direction is best for the migration with symmetric operators in Figure 7.2d, though this plot shows more distortion in the  $x_1$  direction. The artefacts of the extrapolation at the edges of the data set clearly show their influence after the migration with asymmetric operators in Figure 7.2c. The use of 3-points operators for the outmost points suppressed these side effects in both the forward extrapolation of the source signal and the inverse extrapolation of the data. However, in the correlation these artefacts will line up and their effect will be amplified again. The boulder can be localized in both the asymmetric and the symmetric migration, but like in the extrapolation their average noise level after the asymmetric migration is smaller.

In real measurements, the data will be influenced by the earth surface. Figure 7.3a shows the same sketch as Figure 7.1a, only now the earth surface is a reflector where all seismic energy will be returned. It has a reflection coefficient equal to -1. In the time-distance plot of Figure 7.3b, it can be seen that the receivers have registered four events. The direct reflection of the boulder arrives at the receivers first as a hyperbolic event with its apex between  $x_3 = 17$  and 18 m. Because of the limited aperture, only a small part of the hyperbole is visible. The other 3 events are caused by the earth surface.

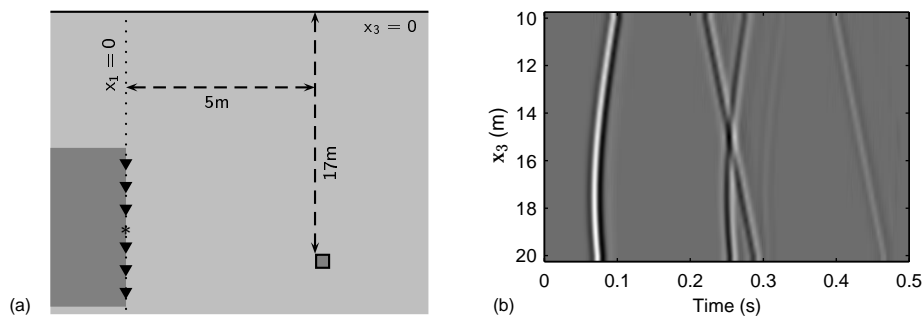


**Figure 7.3:** Model with boulder in the path of the TBM and earth surface taken into account (a), modelled data set (b)

In order to explain the ground reflections, the same model is made without the earth surface, with a long line of 201 receivers ranging from  $x_3 = -50$  m to 50 m. Next to the original source and obstacle, a “ghost” source is located 15 m above the earth surface and a “ghost” obstacle at 17 m. They introduce events in the data that simulate the presence of a reflector at  $x_3 = 0$ . Figure 7.4 shows the recording in which the 4 events from Figure 7.3b reappear. The little sketches show how the waves have travelled to generate the corresponding event. For the direct reflection of event (1), the waves obviously travel directly from the source to the boulder and back to the receiver line. The hyperbolic nature of this reflection is now clearly visible. Event (2) also represents the original obstacle, but in this case the ghost source has been triggered. In reality, this event originates from waves travelling from the source to the earth surface and then to the boulder that reflects them to the receivers. It is shifted in time compared to the direct reflection because of the larger travel path of the source signal. Because of the negative reflection coefficient

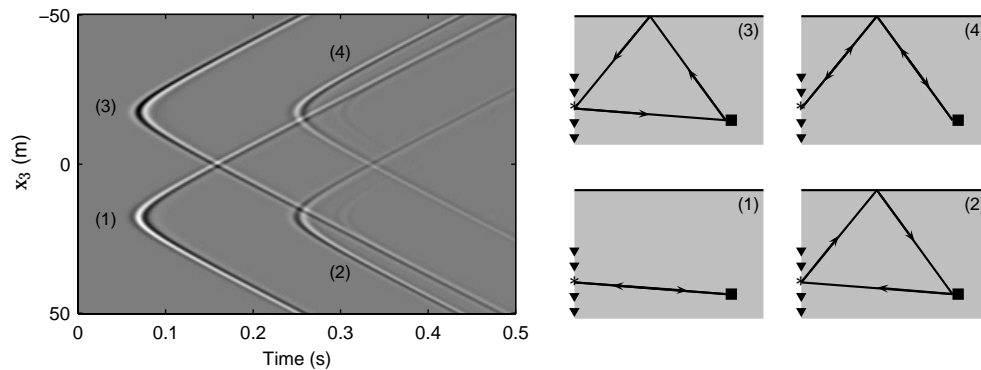


**Figure 7.4:** Reference model to show introduction of the ground surface with ghost source and ghost obstacle

at the earth surface, the polarity of the signals has changed. Hyperboles (3) and (4) are reflections from the ghost obstacle. Their apex coincides with the  $x_3$  position of the ghost obstacle. At the depth of the receivers in Figure 7.3, only the linear side of the hyperbole is visible. In event (3), the incident waves come from the ghost source. In an actual measurement, these waves travel directly from the source to the boulder and are reflected at the earth surface after being scattered by the boulder. Therefore these waves arrive firstly at the most shallow receiver. Because of the reflection at the earth surface, this event also shows a change in polarity. For hyperbole (4), the waves from the real source are reflected by the ghost obstacle. In a real situation, this event is a combination of the previous two, as both the incident and the scattered wavefield are reflected at the earth surface first. For the receivers in Figure 7.3b, this situation requires the longest travel path and thus event (4) will arrive the latest in time. Because of the double earth reflection, event (4) has the same polarity as the direct reflection again.

The presence of earth reflections requires special attention in the analysis of the data. Figures 7.5a and b show the data after migration with asymmetric and symmetric operators respectively. The reflection of the boulder is still clearly visible in both plots. A weak event has appeared around  $x_1 = 19.5$  m though. This is caused by event (2) in Figure 7.4, the waves being reflected at the earth surface before reaching the boulder. It gives the impression that a second boulder is present in the path of the TBM. The two linear events that are present in Figure 7.3b have no influence on the result of the migration since their energy does not get focussed.

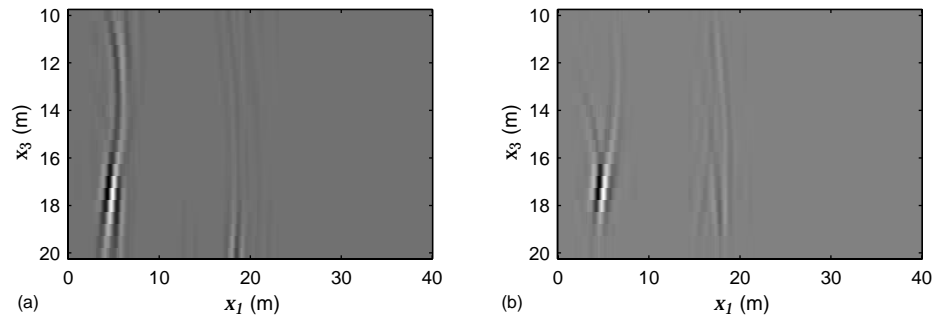


**Figure 7.5:** Migration of data set in Figure 7.3b with asymmetric spatial operators (a) and with symmetric spatial operators (b)

## 7.2 Foundation in the path of the TBM

In a second model, the contrast in the homogeneous subsurface is caused by a foundation (Figure 7.6a). This 0.5 m thick pillar goes vertically into the ground from the earth surface to a depth of 13 m. At the time of the recording, it is located 5 m ahead of the TBM. This example is also considered first without the earth surface. As a result, the data set in Figure 7.6b gives only one reflection in the data, namely the direct reflection from the foundation. The event also has a hyperbolic character. It shows the lowest travel times at the receivers that are at the same level at the

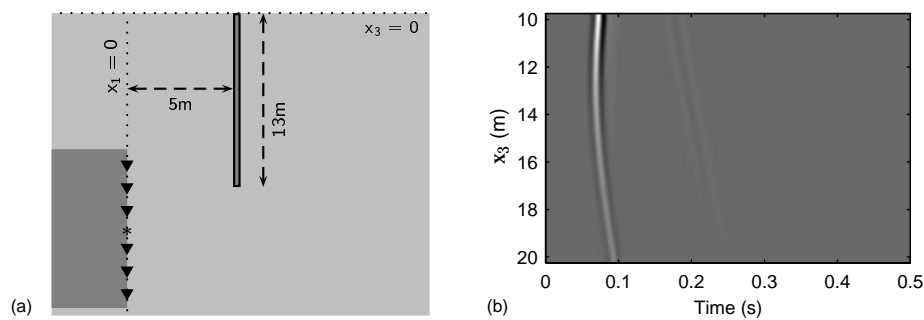


**Figure 7.6:** Model with foundation in the path of the TBM and source and receivers on the head of the TBM (a) and modelled data set (b)

foundation. At lower depths, the travel time increases and the amplitude of the reflection gets damped quickly.

The data set is migrated with the same four methods as the example with the boulder. The results are given in Figure 7.7. As expected, the more ideal migration of the large data set in Figure 7.7a images the foundation perfectly. For the standard phaseshift migration in the wavenumber domain in Figure 7.7b, it can again be concluded that the result has a high noise level. The foundation can be located in the data, but shows many artefacts.

The results of the migration in the spatial domain with asymmetric (Figure 7.7c) and symmetric (Figure 7.7d) operators fall in between these two extremes. Both migrations localize an event for the most shallow receivers at about 5 m from the TBM with side effect deeper in the subsurface. The reflector seems to be more lightly

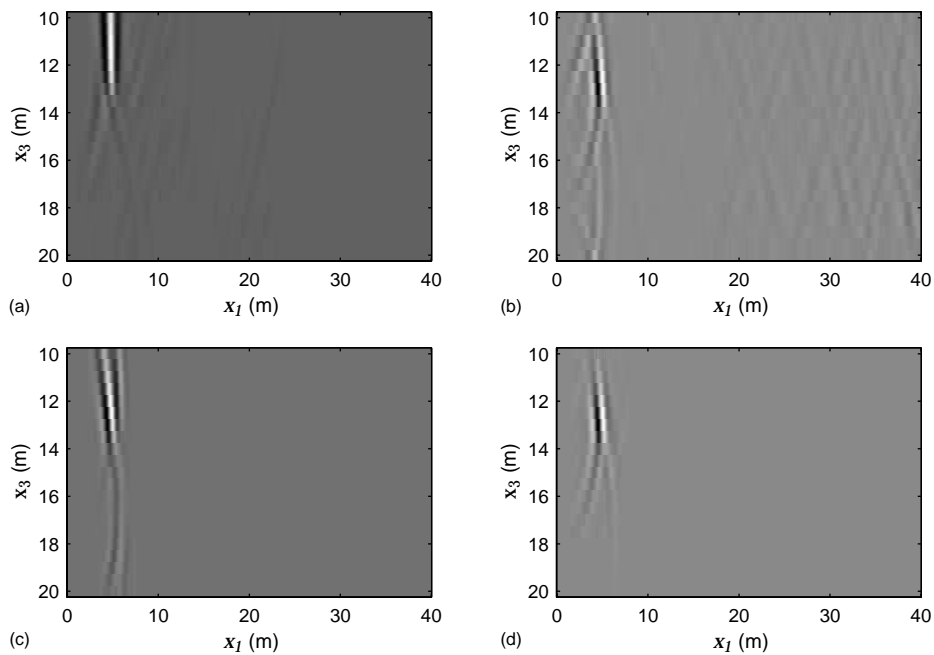


**Figure 7.7:** Migration of data set in Figure 7.6b modelled over 401 traces using 21-points symmetric spatial operators (a), modelled over 21 traces using phase shift migration in the wavenumber domain (b), asymmetric spatial operators (c), symmetric spatial operators (d)

sloping rather than vertical. From the asymmetric migration, it can be concluded that the present obstacle extends at least up to the highest point of the circumference of the TBM. The presence of signal at the outmost receiver at  $x_3 = 10$  m relatively decreases the side effects of the migration at the edges, they are still present, but dominated by the signal. Compared to the result of the migration of the boulder in Figure 7.2c, they are less strong. In the first example, no obstacle was present at either edge of the TBM, leading to artefacts at both sides of the data. The example of the foundation in Figure 7.7c shows no side effects at  $x_3 = 20$  m at all. For the symmetric migration, the difference with the imaging of the boulder is less distinct. Interpretation of Figure 7.7d could easily lead to the conclusion that a small boulder is located around  $x_3 = 13$  m since the reflector is not shown for the most shallow receivers.

The most ideal migration in Figure 7.7a is the only one that generate an unambiguous image of the boulder and the foundation because the entire hyperboles are present in the input data. When only 21 receivers register the reflections, they look very similar in the forward modelled data and will therefore give similar results in the migration.

Figure 7.8b shows how the earth surface has a much stronger influence on the data when the boulder is replaced by a foundation. The earth-surface reflection causes an event in the data that contains much more energy than the direct reflection of the foundation. It is created by all waves that are reflected at the earth surface. The large surface of the foundation generates many reflected waves that interfere and cause one strong event. Because of the reflection at the earth surface, the polarity is inverted. Since the earth-surface reflection results into a linear event, its energy will not be focussed in the migration but will be spread over the data as noise. Therefore the weak hyperbolic reflection of the foundation shows as a strong event both after the asymmetric migration in Figure 7.8c and the symmetric migration in Figure 7.8d. The noise generated by the earth-surface reflections is still visible in both plots because of the high energy content in the data set. In the symmetric migration, it is spread between  $x_1 = 10$  and 20 m. Since the noise is spread over the entire  $x_3$  range, it causes artefacts at the edges of the data set after asymmetric migration, which increases the average noise level.

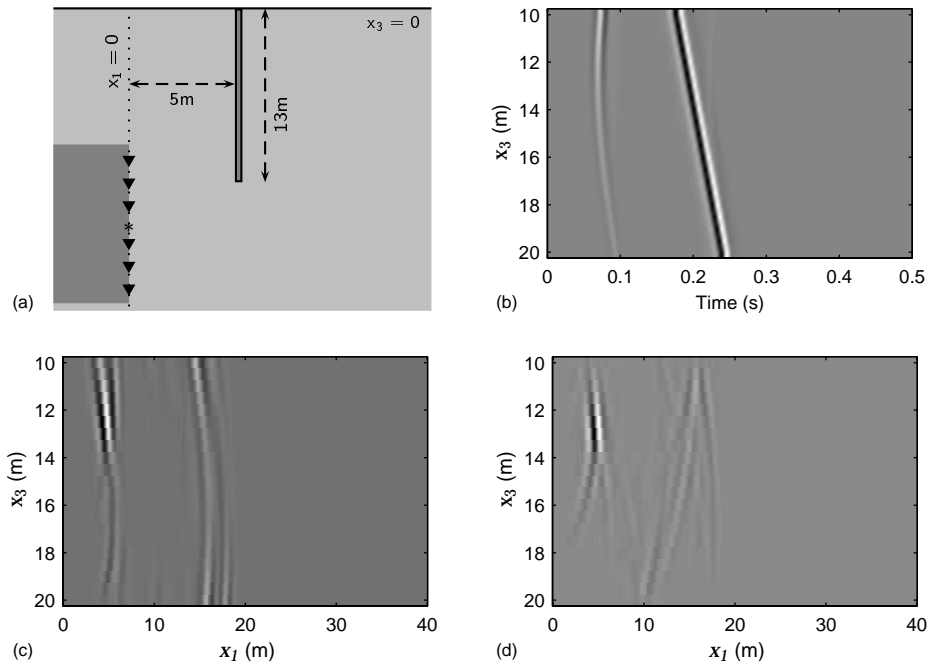


**Figure 7.8:** Model with foundation in the path of the TBM and earth surface taken into account (a), modelled data set (b), migration of data set with asymmetric spatial operators (c) and with symmetric spatial operators (d)

### 7.3 Layered background

In all previous examples, a homogeneous background was considered. In reality, the subsurface is dominantly horizontally layered. Its influence on the imaging of obstacles in front of the TBM is investigated in the next two examples. A two-layer model is considered. The soil of the bottom layer has a velocity of 150 m/s. In the top layer, waves travel at 75 m/s. At a depth of 15 m, there is a gradual transition of the slow layer into the faster one over 0.5 m to avoid artefacts from an abrupt change. The earth surface is not taken into account. In both models, a boulder causes an obstacle for the TBM, at a distance of 5 m from the receiver line. The depth of the boulder varies.

In the first set-up in Figure 7.9a, the boulder is placed at a depth of  $x_3 = 17$  m, which is in the lower layer. Figure 7.9b shows the corresponding data set. One

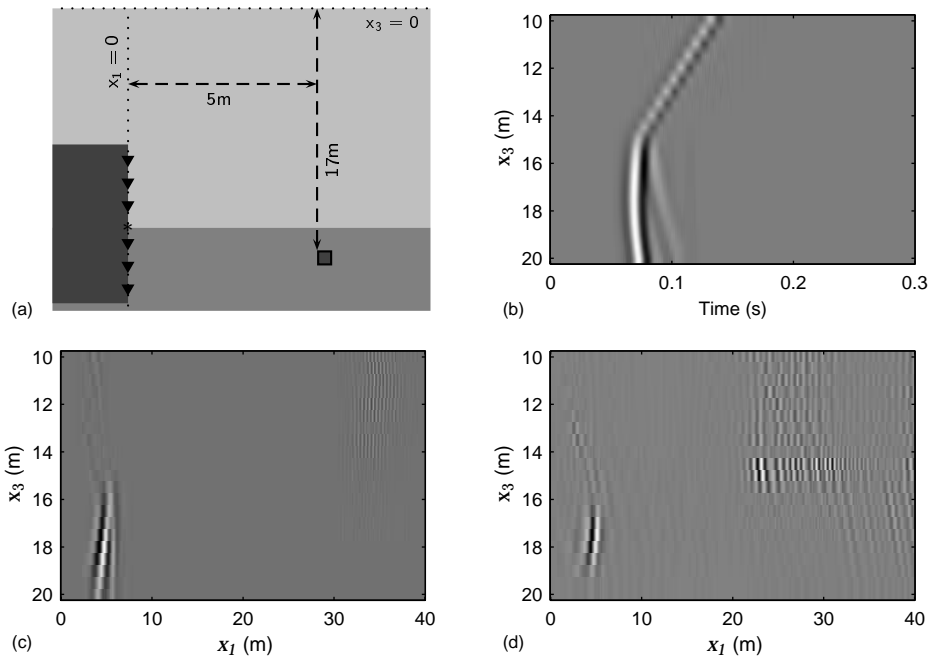


**Figure 7.9:** Model with boulder in a layered background (a), modelled data set (b), migration of data set with asymmetric spatial operators (c) and with symmetric spatial operators (d)

event is recorded in which the layering of the subsurface is clearly visible. When the velocity decreases at the most shallow receivers, the travel time of the waves becomes longer. The receivers in the lower layer register a second weak event that arrives shortly after the direct reflection of the boulder. At the depth of the interface, it coincides with the main event. This event is generated when the wavefield that is scattered by the boulder reflects at the interface before reaching the receiver line. This explains why it is not visible in the upper layer.

This data set is migrated with asymmetric operators (Figure 7.9c) and with symmetric operators (Figure 7.9d). For the migration, the layered background is taken into account. For each output point, the local velocity in the model is checked for the design of the correct operator. Both methods focus the energy at the correct location of the boulder in the subsurface. The resolution in  $x_3$  direction after the asymmetric migration is again slightly influenced by the side effects of the technique. The symmetric migration however generates much more noise in data at later times, especially in the slower top layer. The noise is so strong that the relevant image of the boulder in the data gets suppressed. When the background becomes more

layered, the negative effects of the symmetric migration will increase.

The same observations can be made in the second model. In this case, the boulder is located at a depth of  $x_3 = 12$  m, meaning in the top layer of the model. Therefore the event in Figure 7.10b arrives later in time. The reflection of the interface is now visible in the top layer. The migration with asymmetric operators in Figure 7.9c still gives a very clear image of the boulder at its correct position. The symmetric migration generates even more noise at later times and the reflection of the boulder is hardly visible in the data set.

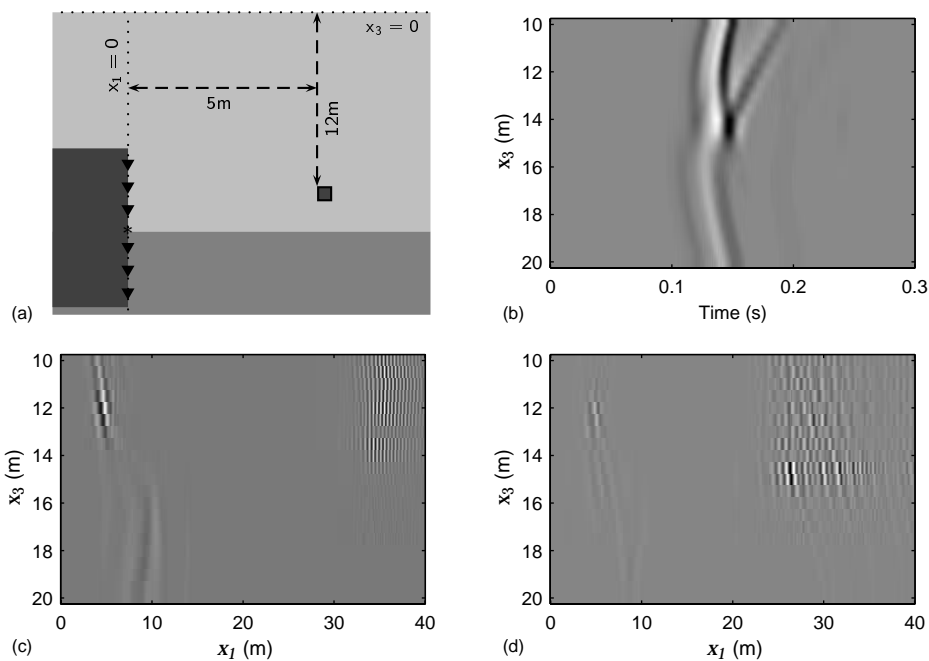


**Figure 7.10:** Model with boulder in a layered background (a), modelled data set (b), migration of data set with asymmetric spatial operators (c) and with symmetric spatial operators (d)

## 7.4 Forward propagation of the TBM

Typical about the configuration with a TBM is that the distance to any obstacle in its path decreases when the machine propagates forward. This means that the same reflectors will be registered at different positions. Combination of these measurements will give extra information about the obstacle and will make it easier to identify. This is clarified in Figure 7.11 with a model where a boulder is placed in a homogeneous background at changing distances from the receiver line. The earth surface is not included in the model. The top of the obstacle is located at  $x_3 = 17$  m. The data set in Figure 7.11a shows the reflector of the obstacle at 10 m in front of the TBM, the result of migration with asymmetric operators is plotted in Figure 7.11b. Figure 7.11c and d give the same data sets in case the obstacle is situated at  $x_1 = 5$  m. In Figure 7.11e and f, the TBM has moved to 2 m from the boulder. In the time-distance plots, it can be seen how the travel time of the waves decreases when the TBM gets closer to the boulder. At the same time, the hyperbolic effect of the reflector in the data increases which will improve the resolution in the migration. This effect is clearly visible in the  $(x_1, x_3)$  plots. When the distance between the boulder and the TBM decreases, the image of the boulder becomes more focussed. Also the artefacts from the asymmetric operators at the edges of the data set disappear slowly. While in Figure 7.11b it is possible to indicate the presence of an obstacle, in Figure 7.11f its position and size can be clearly identified. Instead of only looking at the separate recordings, the information of each measurement at different lateral positions of the TBM can be combined to improve the image. Adding the migrated data sets after applying a shift in the  $x_1$  direction to compensate for the progression of the TBM, will amplify the image of the boulder and cancel the artefacts.

For measurements where the receivers also register the earth surface, the propagation of the TBM helps identifying the earth-surface reflections in the migrated data. Events generated by two separate boulders would remain at a constant  $x_1$  distance from each other. If the second event were caused by the earth surface, its distance to the direct reflection in the migrated data would decrease proportionally with the distance between the TBM and the boulder.

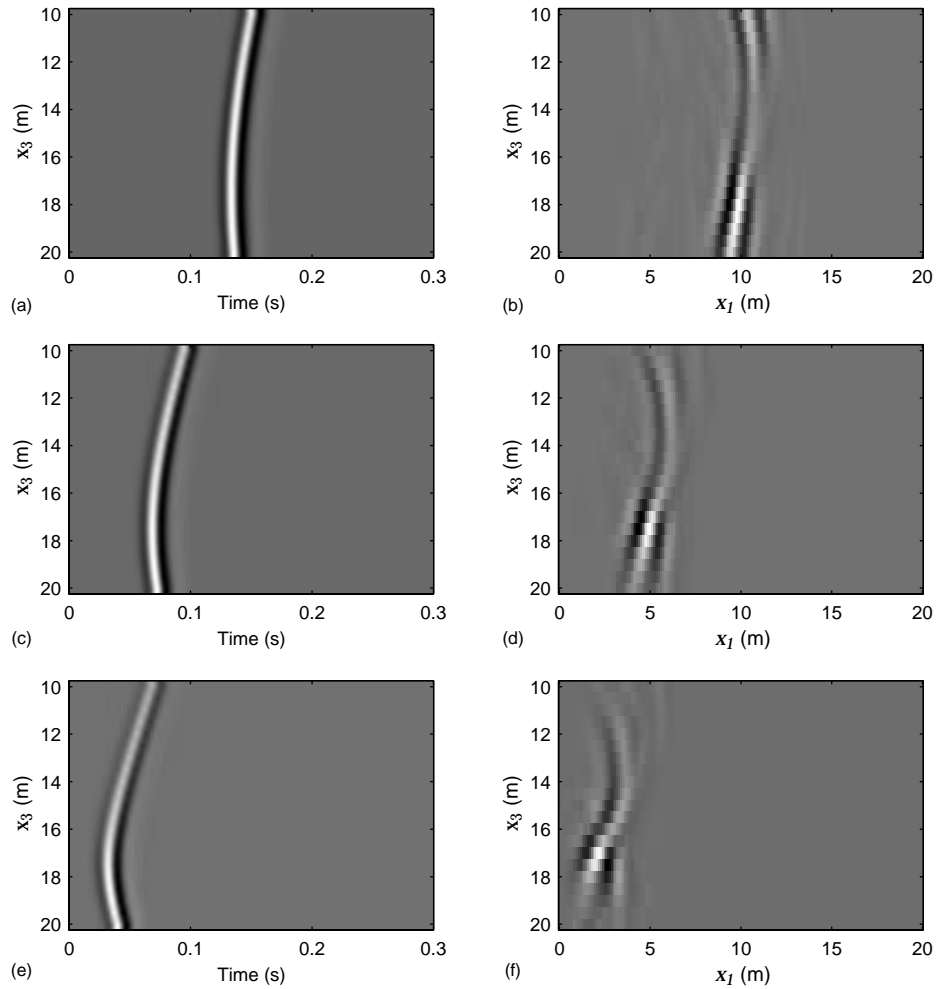


**Figure 7.11:** Forward modelled data set and migration with asymmetric spatial operators of model with boulder at depth 17 m and at a distance 10 m (a and b), 5 m (c and d) and 2 m (e and f) of the TBM



## Conclusions and Discussion

---

It is important to be able to make an accurate image of the subsurface in front of a Tunnel Boring Machine. Detection of obstacles in the path of the TBM can avoid large damage to the machine and to constructions on the earth surface resulting in high cost of repairs and delays. A detailed knowledge of the geological structures at the front face will simplify the tunnelling process as parameters can be adjusted in time. Shear seismics is an excellent method for imaging soft soils. The best image will be obtained with a system on the TBM itself. It will provide information to complete the profiles made from surface seismics and geotechnical surveys.

The first part of this thesis examined the seismic energy emitted by the TBM. When the TBM is drilling, it generates waves that can be registered by geophones at the earth surface. They are shear waves with a velocity varying between 110 and 180 m/s, depending on the soil conditions (content of sand, clay or peat) of the subsurface. This signal has frequencies in the range of 5 to 100 Hz. These seismic waves are excellent for imaging soft soils found in the Dutch subsurface. Shear waves, unlike compressional waves, are not influenced by ground water.

The source of these seismic waves are the hydraulic jacks, located approximately 8 m behind the cutter wheel, at the end of the TBM. The signals are not caused by the engines and pumps in the tunnelling machine, or the measuring equipment inside the hydraulic jacks. They are possibly generated by an interaction between the hydraulic jacks and the shield of the machine, related to the friction on the shield when the TBM progresses. The exact interaction between the hydraulic jacks and the shield of the TBM is not investigated. Installing a high-frequency displacement sensor to measure the relative displacement between the jacks and the shield could give more insight into the mechanism. Obviously, the progress of the TBM depends on the soil around it. This will influence the interaction between the jacks and the shield and therefore the emission of the shear waves. The disadvantage of working with a passive source is that the frequency of the emission of signals cannot be controlled. Depending on soil conditions, it is possible that no seismic energy

is generated. Nevertheless, the passive source is still very useful for monitoring. When the source signal itself is also registered, correlation methods will give a very feasible solution. Installation of an active, fully controllable source on the TBM would give a more stable data set and, therefore, a better image of the subsurface in front of the TBM.

Experiments with the TBM as a seismic source have shown that it is possible to register reflections from obstacles around and in front of the TBM with geophones installed on the lining of the tunnel. Because of the position of the source at the end of the shield of the TBM it is difficult to image the entire area in front of the machine. There will always be a blind zone at the face that cannot be reached by the seismic waves. This can be solved by combination with other systems. Again, a better solution is to install an active source, not on the shield of the TBM, but on the cutter wheel. This is the most advantageous position for both source and receivers to image the subsurface ahead of the tunnel face.

Experiments did not make it clear whether seismic waves propagate in the bentonite slurry in front of the TBM. Pressure transducers on the TBM did not register explosives. Geophones installed at depth also did not record the signal very clearly. It is crucial, especially in shear seismics, that there is a direct contact between the transducers and the soil. When designing an active source and receivers to install on the cutter wheel of the TBM, this problem should be taken into account. Therefore, a part of future research should examine a movable source and receivers, from the blades of the cutter wheel towards the soil face. In addition, the thixotropic behaviour of the bentonite and its influence on penetration by seismic waves should be investigated further.

The configuration with a seismic source and receivers on the cutter wheel requires special care in processing techniques. Data recorded with a small number of receivers with limited aperture will incorporate large artefacts. Phase shift migration in the wave number domain is not the best method. Migration should be performed in the spatial domain. Using a weighted least-squares approximation, short spatial operators are designed that are accurate over a chosen wave number interval in the wave number domain and stable over the entire wave number range. Introduction of a smoothed desired operator, instead of a block-filtered operator, in the approximation procedure has increased the accuracy of the operators. Making these operators asymmetric avoids truncation of the operators at the edges of a data set improving the stability of the operator. By varying the weight and the wave num-

ber interval in which the operator should be accurate, the optimal operator for the selected output point can be determined. At the outermost points, special attention is still needed to ensure stability of the operators.

The short spatial asymmetric and symmetric operators are compared in some synthetic extrapolation tests. Other than some small differences, both sets of operators have a similar effect on the data. The limited aperture has less influence on the forward extrapolation with asymmetric extrapolators. The symmetric operators distort the wave number spectrum of the data. In the inverse extrapolation, the symmetric operators generate fewer side effects. The accuracy of the operators decreases with the length of the operators for all situations and therefore increases distortion of the data.

In models with a horizontally layered background, migration with asymmetric operators clearly results in a better image. Both methods will image reflectors at their correct position, but the symmetric operators generate more artefacts in the data. In the Netherlands, irregular layering is an important property of the shallow subsurface. For simple models with a homogeneous background, the performance of the short symmetric and asymmetric spatial operators is similar. The presence of an earth surface in the model will generate an extra event in the migrated data set, but by making recordings at different distances from the reflector, these earth reflections can be easily separated from the direct reflections from heterogeneities in the subsurface. The image of a reflector becomes more accurate when the TBM approaches. By combining several recordings at decreasing distances, the migrated data sets could be improved further.

The new processing techniques provide a large improvement in migration of the data for tunnelling applications in comparison with traditional phaseshift migration in the wave number domain. It is possible to make an accurate image of the heterogeneities ahead of the tunnel face as shown in the 2D examples in this thesis. For real data, the operator design obviously should be extended to a 3D configuration. This will increase the amount of data and the processing time. When developing data processing software for imaging ahead of the TBM, this should be taken into account so that measures can be taken in time. The use of the short asymmetric operators for migration will increase safety for tunnelling in soft soils.



# A

## Field configuration 1

---

The measurements described here are carried out between October 28 and November 4, 1997. They are set up at the Test Field South of the Second Heinenoord Tunnel. At this point, the excavation of the first (West) tunnel tube has passed underneath the Oude Maas. The TBM goes from North to South under the test field. On the Test Field South, several monitoring systems are installed by companies and organizations involved in this project. The seismic set-up uses the TCH (Tunnel Combinatie Heinenoord) points as a reference frame. An overview of the seismic lines is given in Figure A.1.

One line of geophones is installed parallel to the axis of the TBM. This is called the in-line direction. The geophones are not placed right above the tunnel axis, but 3.1 m to the West. The TBM has a diameter of 8.3 m so it still passes underneath the geophone line. Geophone 11 is located opposite TCH-point 22. The line consists of 48 1-component 10 Hz geophones with a 2 m spacing. They register only the vertical component of the seismic energy that reaches them. The TBM passes geophone 48 first and travels towards geophone 1.

The other two geophone lines are put perpendicular to the axis of the tunnel. They are in the cross-line direction. These are 3-component 10 Hz geophones. Besides the vertical energy component, they also measure 2 perpendicular horizontal components. The geophones are positioned in such a way that one of the horizontal components is parallel to the tunnel axis, the so-called in-line component, and the other one perpendicular to the tunnel axis, the cross-line component.

Cross-line measurements start on cross-line 1. This line consists of 26 geophones at a spacing of 1.5 m. It is placed 5 m North of TCH-point 22. Geophone 18 is in the middle between geophones 13 and 14 of the in-line. The geophones are numbered from East to West.

Later measurements are done on cross-line 2, which is situated just outside the Test

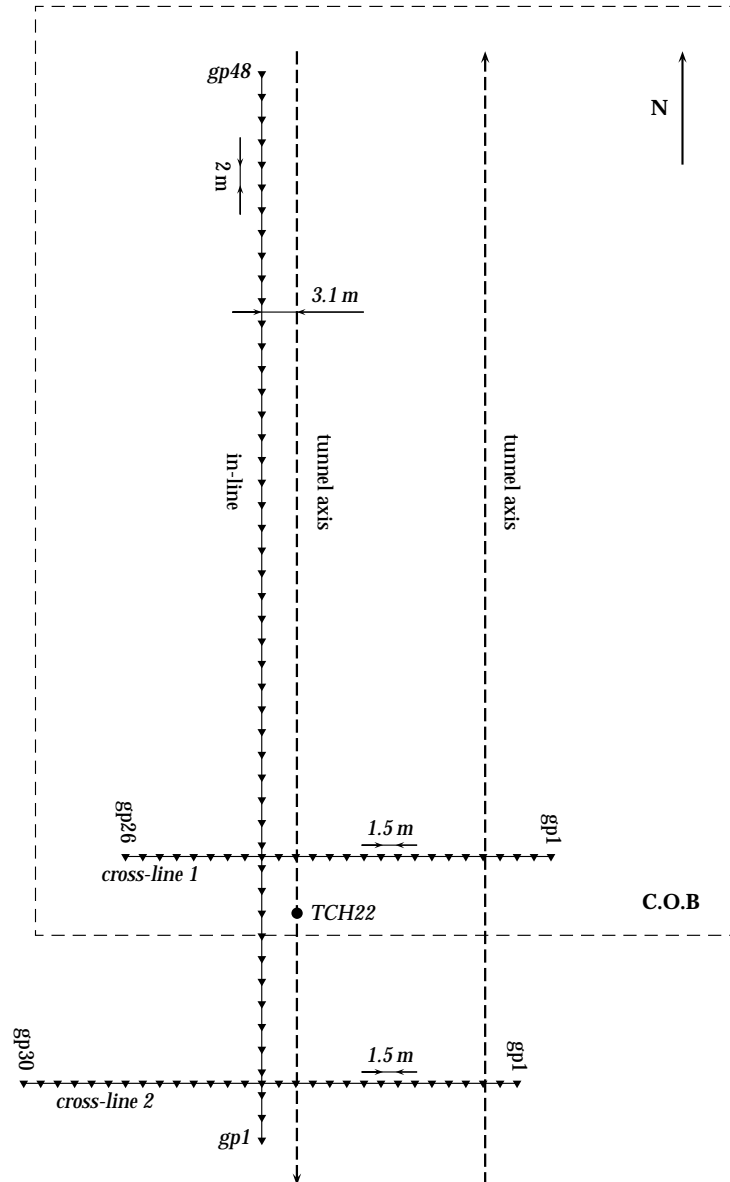


**Figure A.1:** Geometry of the geophones for the experiments in October-November 1997 at the Test Field South of the Second Heinenoord Tunnel

Field South. 30 geophones are set, also at a 1.5 m spacing. This line is put 15 m South of TCH-point 22. This coincides with the turbo-cone measurements that are performed simultaneously by Grondmechanica Delft. Geophone 16 is in the middle between geophones 3 and 4 of the in-line. The geophones are numbered from East to West.



# B

## Field configuration 2

---

The measurements described in this appendix are carried out in March 1998. They are set up outside the Test Field South of the Second Heinenoord Tunnel. At this time, the excavation of the first (West) tunnel tube is finished. Boring of the East tunnel tube has started and the TBM passes the set-up from South to North before it reaches the test field.

### B.1 Geophones in depth

To investigate the penetration of the seismic signals in front of the TBM, a special experiment is set up to bury 3-component geophones in the subsurface at the depth of the TBM. For these measurements, eight geophones are used, of which four are in the trajectory of the TBM. They are all positioned in the same plane parallel to the bore front, in the middle of tunnel ring 49. Therefore the TBM will reach the geophones after installation of ring 43. The geophones are not in a vertical plane since at that point, the TBM is inclined down with a slope of 1 m every 30 m. The axis of the tunnel here is at 11.75 m below N.A.P. . The geometry of the geophones in this plane is shown in Figure B.1.

To install the geophones in the subsurface, holes are bored from the surface, a little bit deeper than the required depth. They are brought in their exact position using positioning tools from Grondmechanica Delft. Figure B.1 actually shows the desired depth of the geophones. There will always be divergences because of inaccuracies during drilling the boreholes. Unfortunately, in reality problems are bigger. Successful trial tests were performed near the experiment site. During the actual installation of some of the geophones, a very local and rather stiff peat layer is encountered at approximately 6 m below the surface (at 2.75 m above N.A.P). After getting the drilling bit stuck in this layer several times, these few geophones

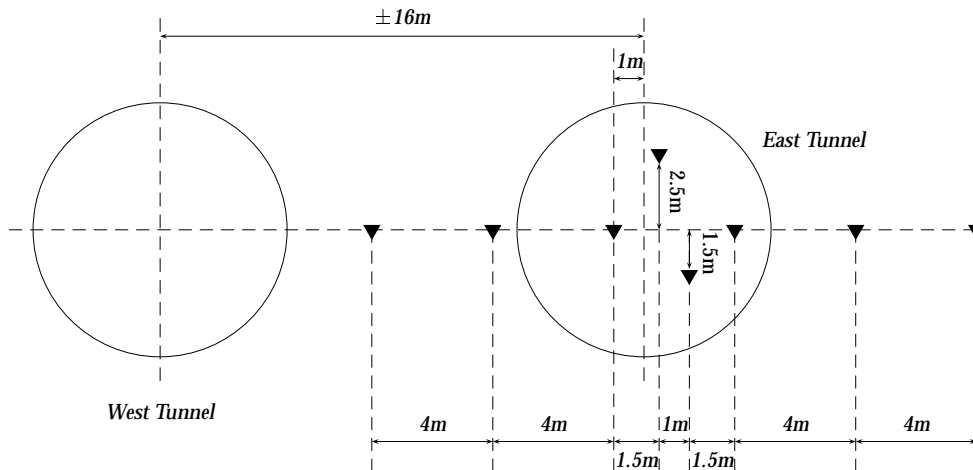


**Figure B.1:** Desired geometry of the 3-component geophones at depth in the plane parallel to the bore front for the experiments in March 1998

are placed in the subsurface as deep as practically possible, so not at the desired position. The positioning tool of Grondmechanica Delft can determine their actual position. The deviations have to be taken into account during processing of the data.

Because some of the geophones are situated in the trajectory of the TBM, several precautionary measures are taken to make sure the excavation process is not disturbed when the geophones are destroyed.

Traditional geophones for surface applications have a special hard-plastic box-shaped casing. For these experiments, Sensor b.v. constructed special geophones (Type SM-7 UGT 50 Hz 370 Ohm) in a cylinder casing so they could easily be installed in the cylindrical borehole. The casing is also adjusted to assure easy destruction by the cutter wheel of the TBM without damaging the cutter teeth. Each geophone consists of 3 coils (one for each component) of 31 mm length and 25 mm diameter. These coils are wrapped with a polyurethane coating and installed in their correct relative position inside a PVC tube with an internal diameter of 40 mm. To restrict loading of the cutter wheel even more, the four geophones in the trajectory of the TBM are at various distances to the axis of the machine in the original set-up. This would cause them all to be hit by different cutter teeth.

The geophones are connected to the recording device at the surface with a six-wire cable that runs through the borehole. Several stress-strain tests have been performed on the cables to control their quick brittle failure. If the cable shows very plastic behaviour, there is a risk that it would get entangled in the cutter wheel before breaking. A string inside the cable guarantees a very small absolute deformation of the cable. After the geophones are in position, the boreholes are closed with a grout mixture existing of

- 3 kg unshrinkable mortar, type CALMIX 931, maximum pressure strength 80 N/mm<sup>2</sup>
- 0.3 kg bentonite
- 10 l water

This grout has a low compressive strength and it assures a good closing of the boreholes. As extra precaution, two knots are made in the cable every 10 cm, with a little plastic disc in between the knots. This ensures the cable to break in between the discs when cutter wheel hits the grout column and pulls the cable. The boreholes are not drilled vertically, but at an angle of 20° to the South (towards the TBM). This causes the TBM to crush the grout column gradually and limits loading of the cutter teeth.

The precautionary measures like the discs and the grout column are only applied for the four geophones in the trajectory of the TBM. In the other four boreholes, the adjusted geophones are also used for easy installation. Special treatment of the cables however is not necessary because they will not influence the excavation process. The boreholes are only closed with sand and swelling clay to avoid instabilities above the TBM. After the measurements, these geophones are retrieved and the boreholes sealed definitely.

The depth of the geophones can be determined exactly by the positioning tool. Because they are in a cylindrical casing, the polarization of the horizontal components can not be controlled while the geophones are lowered in the boreholes. The geophones are fixed with the grout or the swelling clay. Afterwards, explosives (see section B.5) are fired. Analysis of the explosion energy on the recordings will determine the directivity of the geophones in the subsurface.

## B.2 Geophones at the surface

To link the measurements in the subsurface with the previous experiments, a line of 3-component geophones is set up at the surface. Eight geophones are placed vertically above the geophones buried at depth, above ring 49 of the East tunnel tube. Therefore their spacing is not constant, they are closer together around the tunnel axis. The geophones are shown in the view of the surface in Figure B.2.

## B.3 Geophones in the TBM

Several 3-component geophones are used for measurements inside the TBM to register the direct seismic signals emitted by some of the mechanical elements of the machine. Traditional geophones for surface applications are made of a casing that holds the measuring instrumentation. On the bottom of the casing, spikes are attached to ensure solid contact with the soil. These spikes are removed for the measurements inside the TBM. The casing is levelled on the respective TBM element and firmly strapped in position with wire wraps. The geophones are connected to the seismograph, which is located in the measuring cabin inside the TBM.

Four geophones are attached to hydraulic jacks at the end of the TBM. Seven groups of hydraulic jacks are divided over the circumference of the shield of the machine. Each group consists of two jack pairs. The geophones are all strapped to a hydraulic jack of a different group. Two are put on the West wall of the TBM, two on the East wall. They are all in the lower half of the machine due to easy reachability.

Attaching geophones to the shield of the TBM is not possible. Therefore two geophones are tied to U-profiles that are soldered to the shield. The U-profiles are situated near the hydraulic jacks. One geophone is put on one of the hydraulic engines near the front of the machine. A last one is strapped on the axis of the cutter wheel, near the hydraulic engine.

All these geophones are installed for the entire duration of the experiments. A few extra measurements are done with spare geophones on other engines and pumps inside the TBM. They are put in position in a similar way. These measurements only take a few minutes.

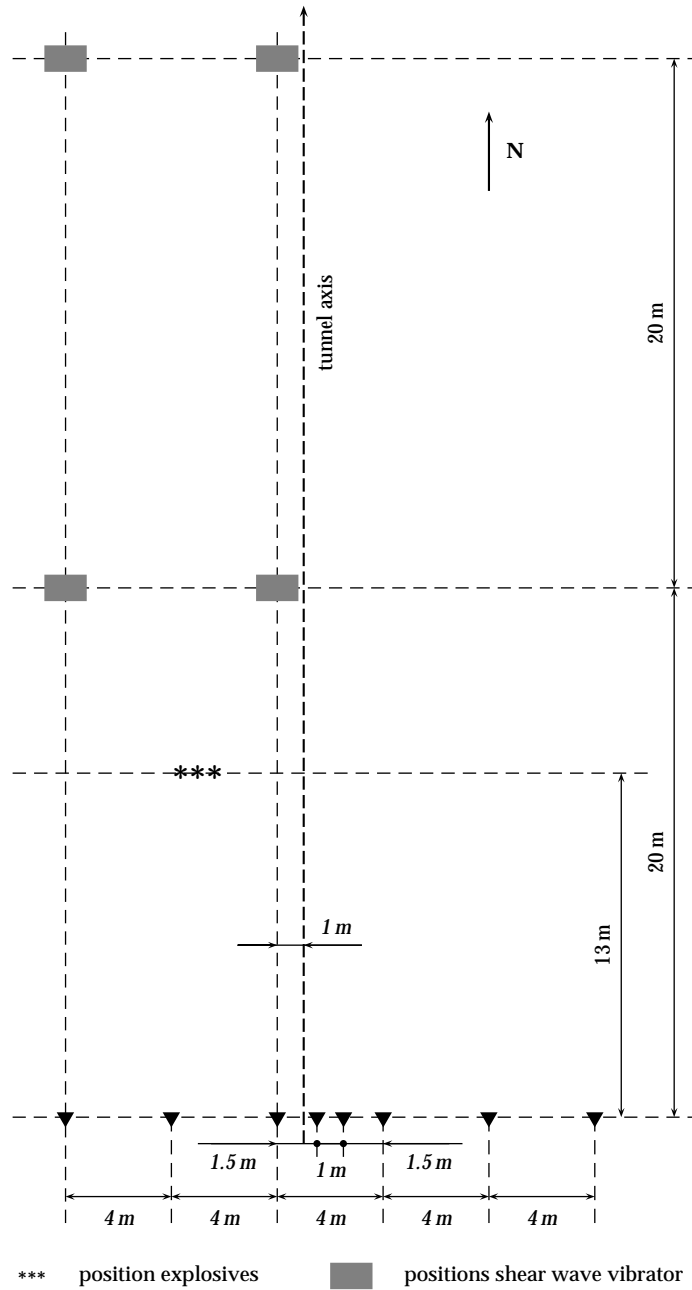


**Figure B.2:** Geometry of the sources and the geophones at the surface for the experiments in March 1998 near the Test Field South of the Second Heineoord Tunnel

## **B.4 Pressure sensors**

For testing the propagation of seismic energy through the bentonite slurry, pressure transducers on the cutter wheel and the diaphragm are used. These sensors are originally installed by WL Delft Hydraulics to monitor pressure variations in the soil in front of the TBM. In these circumstances, the transducers are connected to a data logger which records continuously at a frequency of 1 Hz. For seismic applications this is insufficient. The measuring equipment of the geophones is set at 1 kHz. Temporary adjustments to the existing systems are necessary to change to this higher frequency and to connect the sensors to the seismic system.

### **B.4.0.3 Pressure sensors on the diaphragm**

The pressure sensors on the diaphragm are connected to a data logger that controls the monitoring. An A/D-converter is also incorporated in this data logger. The seismograph is constructed to receive analogue data. Therefore the pressure sensors are directly connected to the seismograph. For the accuracy of the measurements, five pressure sensors are chosen. Figure B.3 shows the distribution of the transducers over the diaphragm. Sensors P09, P12, P13, P14 and P15 are used for the seismic experiments. The other pressure sensors stay connected to the data logger and can continue recording at 1 Hz. After the experiments, the old connections are restored.

### **B.4.0.4 Pressure sensor on the cutter wheel**

The eight pressure sensors on the cutter wheel are also connected to a data logger. This data logger is located on the rotating wheel and can not be reached directly. It performs an A/D conversion on the measurements before they are transmitted to the static part of the TBM where a connection with an external recording device can be made. This would however add an unknown and undesired time delay to the data. Major adjustments to the system only for these seismic measurements would be too excessive at this point. The original measuring unit is maintained and the data will be retrieved later. The system is manually triggered and registers for 15 seconds. Synchronization (see section B.6) will ensure the link with the other recordings.

Since the sensors on the cutter wheel can not be connected directly to the seismograph, adjustments to the data logger are necessary to have it record at a higher



## B.5 Sources

### B.5.0.5 Shear wave vibrator

To test the capability of shear waves to travel through the bentonite slurry a strong active shear wave source is used. It is investigated if this shear energy either propagates through the bentonite or if it is converted into compressional energy that can reach the pressure sensors at the diaphragm or the cutter wheel. A shear wave vibrator of OYO-CAG (Nieuwegein, Netherlands) sends a linear sweep ranging from 10 to 400 Hz into the subsurface.

These measurements are done when the TBM was not excavating and its head is at about 11 m South of the geophone line. The shear wave vibrator is moved to the 4 different locations shown in Figure B.1. The first two positions are at 20 m from the geophone line, so about 31 m from the TBM. The other two are 20 m further. Two positions are in-line with the most West geophone. The other two are 8 m more to the East, 1 m from the tunnel axis.

### B.5.0.6 Explosives

Explosives are used as a source to test the ability of compressional waves to propagate through the bentonite slurry. The pressure sensors on the diaphragm and the cutter wheel should record them. The explosives are also applied to determine the polarization of the geophones at depth after they have been put in position. Finally, the explosives are the controlling factor in the synchronization of all different recording units.

The explosives are buried in the subsurface at approximately 1 m depth. They are fired at different positions on a line 13 m North of the geophone line as can be seen in Figure B.1. To avoid any possible instabilities of the soil when the TBM passes this area, no explosives are shot above the trajectory of the East tunnel. The load of the explosives will not cause damage to the West tunnel tube.

## B.6 Synchronization

The optimal system would connect all the source and receivers to the same trigger box. This ensures synchronized measurements. The pressure sensor at the cutter wheel can however not be incorporated in this system because of the digital con-

nection. The following sequence was set up to make easy combination of all data afterwards possible:

1. The pressure sensor at the cutter wheel is manually triggered and records during 15 s.
2. A trigger box connected to the seismographs simultaneously activates all 3-component geophones, at the surface and in depth, the pressure sensors at the diaphragm and the explosives. The transducers make a recording of 10 s.
3. The shear wave vibrator is activated and produces an 11 s sweep.

There is a time shift of about 1 s between each of these steps. the necessary travel time for the compressional energy of the explosives to reach the pressure sensor at the cutter wheel can be calculated. Tracing the first arrival in the data of this sensor enables linking of these recordings with those controlled by the seismograph.

The first experiments are done during standstill of the TBM. Recordings are made on March 17, 1998, after excavation of ring 41. The shear wave vibrator is used as a source.

A second set of experiments is made while the TBM is active to test the source signal of the machine itself. No shear wave vibrator is used. This is done on March 18; 1998, during excavation of rings 46 and 47.



# C

## Field configuration 3

---

The experiments described here are performed on June 16, 1998, during the excavation of rings 444, 445 and 446 of the East tunnel tube. To record reflections from the West tube, geophones have to be installed on the West wall of the East tube. In the elements that form the tunnel rings, several screw threads are built in. They are used to fasten the supports for the pipelines, to attach gangways, etc. Unused screw threads are available for the seismic experiments. The M20 screw threads that are present in the middle of each element are chosen for the installation of the geophones.

For these experiments, 1-component geophones are used. The geophones are horizontally polarized in the direction of the source signal, parallel to the tunnel axis. To install the geophones into the tunnel lining, some adjustments are necessary. The spikes that are attached to the casing of traditional geophones for surface seismics are removed. Thin metal plates are put onto the geophones and on these plates, M20 bolts were fixed. With these, the geophones can be firmly attached to the screw threads in the tunnel lining and put in the desired direction.

The tunnel rings are installed in such a way that the elements of the even rings are shifted with respect to those of the odd rings. This can be seen in Figure C.1 where the lower half of both rings is shown with the position of the M20 screw threads.

A line of 24 geophones is used. For the convenience of processing, the geophones should be on a horizontal line. Therefore either only the even or the odd rings should be used. This way, the geophones would have a constant spacing of 3 m. Based on the availability and the reachability of the screw threads, this is difficult to accomplish. Therefore the first ten geophones are installed in the O4 screw thread holes of the odd rings; geophone 1 being the closest to the TBM. From that point,

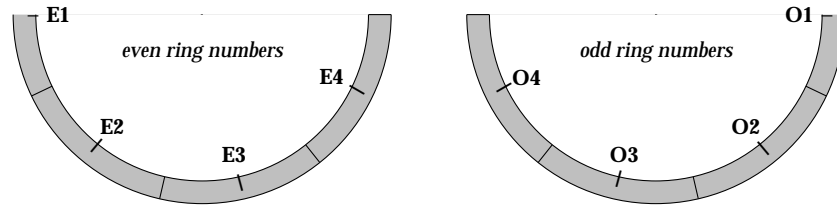


**Figure C.1:** Position of the tunnel elements for the lower half of the odd and even rings of the Second Heinenoord Tunnel and the location of the M20 screw threads

these holes are used for the pipelines. The last 14 geophones are put in the E2 screw threads of the even rings. This causes a spacing of only 1.5 m between geophone 10 and 11. During processing, this is taken into account and corrected for.

## Bibliography

---

- R.J. Aartsen and G.H. Wijnants. Implementation of monitoring strategy Hermes at the Green Heart Tunnel. In *(Re)Claiming the Underground Space, Proceedings of the ITA World Tunnelling Congress 2003, Amsterdam, The Netherlands*, pages 753 – 755, 2003.
- G. Arends, H.J.R. Deketh, and Th.A. Feijen. *Handboek ondergronds bouwen. Dl. 1. Ondergronds bouwen in breed perspectief*. Balkema, Rotterdam, 1997. ISBN 90-5410-437-6.
- Y. Ashida, T. Matsuoka, T. Watanabe, and H. Kusumi. Seismic imaging ahead of tunnel face with three component geophones. In *72th Ann. Internat. Mtg., Soc. Expl. Geophys., Expanded Abstracts*, 2002.
- K.J. Bakker, F. de Boer, J.B.M. Admiraal, and E.P. van Jaarsveld. Monitoring pilot projects using bored tunnelling: the Second Heinenoord Tunnel and the Botlek Rail Tunnel. *Tunnelling and Underground Space Technology*, 14(2):121–129, 1999.
- K.J. Bakker, W. van Schelt, and J.W. Plekkenpol. Predictions and monitoring scheme with respect to the boring of the Second Heinenoord Tunnel. *Geotechnical Aspects of Underground Construction in Soft Ground*, pages 459 – 464, 1996.
- K. B appler and J.H. Jonker. Sophiaspoortunnel - tunnel technique and development of the continuous advance method. In *(Re)Claiming the Underground Space, Proceedings of the ITA World Tunnelling Congress 2003, Amsterdam, The Netherlands*, pages 951 – 955, 2003.
- A.J. Berkhout. *Seismic Resolution: resolving power of acoustic echo techniques*. Geophysical Press Ltd, 1984.
- A.J. Berkhout. *Seismic migration: Imaging of acoustic energy by wave field extrapolation. A. Theoretical aspects*. Elsevier science publishers, 1985.
- A.J. Berkhout and C.P.A. Wapenaar. One-way versions of the Kirchhoff integral. *Geophysics*, 54(4):460 – 467, 1989.
- O. Blacqui ere, H.W.J. Debeye, C.P.A Wapenaar, and A.J. Berkhout. 3D Table-driven migration. *Geophysical Prospecting*, 37(8):925 – 958, 1989.

- X. Borràs i Gabarró, R. Boté i Frech, B. Maidl, and N. Della Valle. Metro barcelona línea 9 - Europ's greatest metro project with shield tunnel boring machines of large diameters. In *(Re)Claiming the Underground Space, Proceedings of the ITA World Tunnelling Congress 2003, Amsterdam, The Netherlands*, pages 637 – 643, 2003.
- W. Broere. *Tunnel face stability & New CPT applications*. PhD thesis, Delft University of Technology, January 2001.
- J. Brouwer, R. Ghose, K. Helbig, and V. Nijhof. The improvement of geotechnical subsurface models through the application of S-wave reflection seismic exploration. In *Proc. Environ. Engin. Geophys. Soc. meeting, Aarhus, 1997*.
- COB/CUR. Monitoring graafront boorproces, Ontwikkeling speurneus concept. Technical Report L 330-03, COB/CUR, Gouda, December 1999.
- R. de Leeuw and E. Oele. Westerschelde Tunnel: integrating the fitting out during the boring process - a complex period. In *(Re)Claiming the Underground Space, Proceedings of the ITA World Tunnelling Congress 2003, Amsterdam, The Netherlands*, pages 599 – 605, 2003.
- Z. Eisenstein and O. Ezzeldine. The role of face pressure for shields with positive ground control. *Tunnelling and Ground Conditions*, pages 557 – 571, 1994.
- C. Falk. Pre-Investigation of the Subsoil Developments in Construction of the 4th Elbe Tunnel Tube. *Tunnelling and Underground Space Technology*, 13(2):111 – 119, 1998.
- J.T. Fokkema and P.M. van den Berg. *Seismic Applications of Acoustic Reciprocity*. Elsevier, Amsterdam, 1993. ISBN 0-444-89044-0.
- J. Gazdag. Wave equation migration with the phase-shift method. *Geophysics*, 43: 1342 – 1351, 1978.
- R. Ghose. High-frequency shear-wave reflections to monitor lateral variations in soil, supplementing downhole geotechnical tests. In *Proc. World Tunneling Congress, Amsterdam, 2003*.
- R. Ghose and J.C.M. Goudswaard. Integrating S-wave seismic reflection and CPT using a multi-angle, multi-scale approach. *Geophysics*, 2001.
- R. Ghose, V. Nijhof, and J. Brouwer. Shallow, high-resolution, shear-wave reflection imaging: extended potential in geotechnical surveys. In *Proc. Environ. Engin. Soc. Europ. Sec. Meeting, Barcelona, Spain, 1998*.

- P. Grasso, S. Xu, M. Del Fedele, G. Russo, and E. Chiriotti. Particular failure mechanisms of weathered granite observed during construction of metro tunnels by TBM. In *(Re)Claiming the Underground Space, Proceedings of the ITA World Tunnelling Congress 2003, Amsterdam, The Netherlands*, pages 497 – 503, 2003.
- D. Hale. Stable explicit extrapolation of seismic wavefields. *Geophysics*, 56:1770 – 1777, 1991.
- O. Holberg. Towards optimum one-way wave propagation. *Geophysical Prospecting*, 36:99 – 114, 1988.
- H. Hosaka, K. Goto, T. Goto, and H. Sakurai. F-NAVI shield tunneling method - simultaneous excavation and segment erection for high-speed tunneling. In *(Re)Claiming the Underground Space, Proceedings of the ITA World Tunnelling Congress 2003, Amsterdam, The Netherlands*, pages 701 – 706, 2003.
- T. Inazaki, H. Isahai, S. Kawamura, T. Kurahashi, and H. Hayashi. Stepwise application of horizontal seismic profiling for tunnel prediction ahead of the face. *Leading Edge*, pages 1429 – 1431, 1999.
- J.H. Jonker, D. Handke, and S. van der Woude. Experience with the application of innovative shield tunnelling techniques during the construction of the betuweroute. In *(Re)Claiming the Underground Space, Proceedings of the ITA World Tunnelling Congress 2003, Amsterdam, The Netherlands*, pages 591 – 597, 2003.
- P.S. Jovanovic and J.H. Jonker. Retrospective of tunnelling projects in the Netherlands, 1993-2003, ten years of challenges. In *(Re)Claiming the Underground Space, Proceedings of the ITA World Tunnelling Congress 2003, Amsterdam, The Netherlands*, pages 867 – 873, 2003.
- S. Kanayasu, I. Kubota, and N. Shikibu. Stability of face during shield tunneling - A Survey on Japanese shield tunneling. *Underground Construction in Soft Ground*, pages 337 – 343, 1995.
- G. Kneib, A. Kassel, and K. Lorenz. Automatic seismic prediction ahead of the tunnel boring machine. *First Break*, 18(7):295 – 302, 2000.
- T. Kobayashi, J. Satou, S. Maeda, T. Yamamoto, S. Suguru, T Honjou, and K. Nishioka. New development of hard rock TBMs excavation monitoring tool and control system and true reflection tomography. In *(Re)Claiming the Underground Space, Proceedings of the ITA World Tunnelling Congress 2003, Amsterdam, The Netherlands*, pages 957 – 963, 2003.

- K. Kurihara, H. Kawata, and J. Konishi. Current practise of shield tunneling methods - A Survey on Japanese shield tunneling. *Underground Construction in Soft Ground*, pages 329 – 336, 1995.
- W.L. Leendertse, K.J. Bakker, and E.A.H. Teunissen. TBM - Tunnelling in the Netherlads – An overview of research and development. *Tunnels for People*, pages 593 – 603, 1997.
- U. Maidl and S. Hintz. Comparative analysis between the support of the tunnel face with foam (EPB) or bentonite (slurry shield) in Dutch soft ground. In *(Re)Claiming the Underground Space, Proceedings of the ITA World Tunnelling Congress 2003, Amsterdam, The Netherlands*, pages 773 – 778, 2003.
- A. Nautiyal, S.H. Gray, N.D. Whitmore, and J.D. Garing. Stability versus accuracy for an explicit wavefield extrapolation operator. *Geophysics*, 58:277 – 283, 1993.
- H. Netzel and F.J. Kaalberg. Monitoring the deformation behaviour of buildings in amsterdam. In *(Re)Claiming the Underground Space, Proceedings of the ITA World Tunnelling Congress 2003, Amsterdam, The Netherlands*, pages 999 – 1001, 2003.
- D.J.M. Ngan-Tillard, B. Bhattacharta, C. Bremmer, H. Kok, G. Kruse, J. Maccabi-ani, A. den Outer, D. Solomatine, J. Streng, H. Veldkamp, and H. Weerts. Semi-automatic interpretation of CPT's for better predictions of the subsurface. *Canadian Geotechnical Journal*, 2003. submitted for publication.
- T. Nomoto, H. Mori, and M. Matsumoto. Overview on ground movements during shield tunneling - A Survey on Japanese shield tunneling. *Underground Construction in Soft Ground*, pages 345 – 351, 1995.
- J. Nymann and S.D. Taylor. Construction of the Copenhagen Metro. In *(Re)Claiming the Underground Space, Proceedings of the ITA World Tunnelling Congress 2003, Amsterdam, The Netherlands*, pages 607 – 612, 2003.
- A.J.M. Peters and J.W. Plekkenpol. Nauwkeurige sensoren registreren het boren. *Land + Water*, 7:13 – 17, 1997.
- L. Petronio, F. Poletto, and A. Schleifer. Seismic-While-Drilling using the Tunnel-Boring-Machine noise. In *70th Ann. Internat. Mtg., Soc. Expl. Geophys., Expanded Abstracts*, 2000.
- J.W. Rayleigh. *Theory of Sound, Volume II (second edition)*. Macmillan, London, 1945.
- J.W. Rector and B.P. Marion. The use of drill-bit energy as a downhole seismic source. *Geophysics*, 56(5):628 – 634, 1991.

- J.M.C. Roxo. Tunnels as a sustainable environmental solution - a case study. In *(Re)Claiming the Underground Space, Proceedings of the ITA World Tunnelling Congress 2003, Amsterdam, The Netherlands*, pages 139 – 144, 2003.
- G. Sattel, P. Frey, and R. Amberg. Prediction ahead of the tunnel face by seismic methods – pilot project in Centovalli Tunnel, Locarno, Switzerland. *First Break*, 10(1):19 – 25, 1992.
- G. Sattel, B.K. Sander, F. Amberg, and T. Kashiwa. Tunnel Seismic Prediction, TSP - some case histories. *Tunnel & Tunnelling*, 1996.
- MTS Sensor Technology GmbH & Co. KG. Temposonics II, Baureihen TTA; TTM und TTS für externe Auswerteeinheit. MTS - TII - 94D, 1994.
- B. Stack. *Handbook of Mining and Tunnelling Machinery*. Wiley - Interscience, 1982.
- W. Steiner. Criteria for selecting mechanised tunnelling systems in soft ground. *North American Tunneling*, pages 483 – 491, 1996.
- R.B. Storry, A.S. Stenning, and A.N. MacDonald. Geotechnical design and construction aspects of the Tsing Tsuen Tunnels - contract DB320 KCRC West Rail Project. In *(Re)Claiming the Underground Space, Proceedings of the ITA World Tunnelling Congress 2003, Amsterdam, The Netherlands*, pages 621 – 627, 2003.
- K. Suyama, T. Imai, H. Ohtomo, K. Ohta, and T. Takahashi. *Delineation of structures in alluvium and diluvium using SH-wave reflection and VSP methods*, pages 165–179. Society of Exploration GeoPhysics, 1986.
- J. Thorbecke. *Common Focus Point Technology*. PhD thesis, Delft University of Technology, January 1997.
- J.K. van Deen, G. Greeuw, R. van den Hondel, M.Th. van Staveren, F.J.M. Hoefloot, and B. Vanhout. Horizontal CPTs for reconnaissance before the TBM front. In *Geotechnical Engineering for Transportation Infrastructure*, pages 2023 – 2030. Barends et al., 1999.
- J.K. van Deen and M.W.P. van Lange. Literatuuronderzoek monitoring graafront. Technical Report CO-364140/14, COB/CUR, Gouda, June 1996.
- C.J. van Staalduinen, H.A. van Adrichem Boogaert, M.J.M. Bless, J.W.Chr. Doppert, H.M. Harsveldt, H.M. Montfrans, E. Oele, R.A. Wermuth, and W.H. Zagwijn. *The Geology of The Netherlands*. Mededelingen rijks geologische dienst, 1979.
- F.J. Wermer. Second Heinenoord tunel - The first bored tunnel in the Netherlands. *Tunnels for People*, pages 411 – 416, 1997.

- J. Zhang, D.J. Verschuur, and C.P.A. Wapenaar. Depth migration of shot records in heterogeneous transversely isotropic media using optimum explicit operators. *Geophysical Prospecting*, 49:287 – 299, 2001.

# Summary

---

## **The TBM, not a blind mole!**

This thesis deals with some aspects of seismic imaging of the soft soil in front of a Tunnel Boring Machine to help tunnel constructors “see” the subsurface they are approaching, instead of steering the TBM forward like a “blind mole”. The Dutch shallow subsurface has a very irregular layering and contains many heterogeneities. Geotechnical investigation of a tunnelling site, like soundings and borings, gives only local information of the soft subsurface and interpolation of the data will be inaccurate. This affects the safety during tunnel construction. The more information about the soil and obstacles in front of the TBM is known, the better tunnelling parameters can be controlled and damage to the TBM can be avoided. A seismic survey of the area will provide information on lateral variations in the subsurface. In combination with the geotechnical data, a much more accurate image of the tunnel trajectory can be made.

Surface seismics will not always be easy, for example in urbanized areas. A solution would be to have a seismic system on the TBM. Seismic energy emitted from the machine reflects on contrasts ahead of the bore front and is recorded again by receivers on the TBM. The reflected energy gives the tunnel constructors an image of the subsurface in front of the TBM and therefor increases safety of the tunnelling.

The source is a very important element of every seismic system. Its properties have to be optimal so that the emitted signals are suitable for the tunnelling application. In the shallow soft soils of the Netherlands, the use of shear waves is preferred over compressional waves as the former are less influenced by the water in the pores. Since the loose soils cause a high damping, the source signals should be low frequent. Some practical aspects to be investigated are the position of the source (and receivers) on the TBM and the contact with the soil for perfect transmission of the seismic energy.

The design of such a seismic source falls outside the scope of this research. Instead of developing an active source, this thesis firstly examines if seismic energy is emitted by the TBM itself and, if this is the case, whether it is suitable for imaging in soft soils. The construction of the Second Heinenoord Tunnel near Rotterdam is set up as an experimental project in which many aspects of soft soil tunnelling in

the Netherlands are investigated. On this site, seismic experiments are performed, on the earth surface, in the subsurface, in the TBM and in the tunnel. The first geophone lines on the earth surface show recordings of seismic energy coming from the TBM. Processing of the data indicates that the TBM emits shear waves in a frequency range between 5 and 100 Hz. As said before, these are good properties for a seismic source that is to be used in soft soils. Depending on the position of geophone lines, events with an average wavespeed varying from 100 to 200 m/s are registered. These are typical velocities for shear waves in soft soils, higher when the sand content increases, lower when more clay is present. Some recordings show distinct events with a regular amplitude and periodicity. At other locations, these can be very irregular, which makes it more difficult to analyse the data.

In combination with recordings in the TBM itself, the actual source of the seismic signals is determined. Engines and pumps can be excluded quickly. Clear pulses are registered by geophones that are attached to the hydraulic jacks at the end of the TBM. These jacks push the machine forward against the tunnel elements that are already in place. The propagation of the TBM in the soil is not always a smooth movement, but it is influenced by friction effects between the machine and the surrounding soil. Most probably, the emitted seismic signals are related to the operation of the hydraulic jacks and therefore depending on the soil type around the TBM. This explains the variations in amplitude and periodicity.

Experiments in the subsurface and inside the tunnel are carried out to test the suitability of the TBM as a seismic source. Performance of shear wave seismics in soft soils is very good, but for tunnelling applications new aspects have to be taken into account. Whether the TBM is used as a seismic source or an active source is developed, the optimal position for receivers when imaging the subsurface in front of the TBM is the cutter wheel. The slurry shield TBM used for the construction of the Second Heinenoord Tunnel pumps a viscous bentonite to the bore front to ensure its stability. For seismic recording on the cutter wheel, the penetrability of the bentonite by shear waves is crucial. To exclude any uncontrollable aspects of the hydraulic jacks, external compressional and shear wave sources are used in this experiment. As receivers, geophones at depth, in the path of the TBM, and pressure sensors on the cutter wheel are applied. The results are rather ambiguous. The recordings on the geophones show that the waves are highly attenuated. But not even the compressional waves are recorded on the cutter wheel. It is possible that the pressure sensors are not suitable for these kind of measurements. If, on the other hand, the seismic energy could not penetrate the bentonite, special hardware adjustments are necessary.

Also the efficiency of the jacks as seismic source is tested. During construction of

the second tunnel tube of the Second Heinenoord Tunnel, the first tube is used as a strong reflector. Geophones are attached to the tunnel wall of the second tube. The recordings have a very high signal-to-noise ratio. After removal of the direct waves, travelling through the tunnel wall, reflected events generated by the other tunnel tube can be traced in the data, although they are very weak. Reflections coming from ahead of the TBM might therefore be even harder to distinguish. Applying the TBM as an efficient, reliable and controllable seismic source for imaging requires more research on the operation of the hydraulic jacks and the influence of the soil surrounding the TBM.

The theoretical part of this thesis focusses on processing of data from a seismic system for tunnelling, where receivers are installed on the cutter wheel of the TBM. Seismic surveys for oil- and gas exploration are performed over a very large area, using hundreds of receivers. Traditional seismic processing techniques are optimised for these configurations. In tunnelling applications, the receivers are limited in aperture by the diameter of the TBM and in number by the available space on the cutter wheel. Applying the existing processing techniques, like phaseshift migration, on this new configuration will introduce large artefacts into the data because of the truncation of the extrapolation operator. Short, symmetric, spatial extrapolation operators that are stable in a specified wavenumber range are designed, using a weighted-least-squares optimisation. Migration in the spatial domain instead of the frequency domain makes it possible to take small lateral soil variations (perpendicular to the cutter wheel in case of tunnelling applications) into account. For a large number of receivers, the short operators will limit computation time extensively. In tunnelling, the length of the operator will be based on the number of receivers on the cutter wheel. However, the symmetric operators are only optimal for the middle receiver. For the other data points, the operator is shifted and gets asymmetrically truncated, which again generates artefacts. Also, only part of the data points are used in the extrapolation, which is rather inefficient if so few data are available. Therefore the weighted-least-squares optimisation is adjusted to design short, asymmetric, spatial extrapolation operators. For each data point, a new operator is created, based on the number of receivers and the relative position of the data point, taking all other data points into account. By varying the weight and the wavenumber range in which the operator should be accurate, the optimal operator can be calculated. For the outmost points, special attention is necessary to ensure stable operators.

The performance of the symmetric and asymmetric operators in both forward and

inverse extrapolation is compared, for different operator lengths. In the forward experiment, a source signal is forward extrapolated, once with symmetric and once with asymmetric operators. On both data sets, inverse extrapolation is performed with the same, symmetric method so that differences in the final result are only due to the forward extrapolation. Comparison with the original input signal gives an indication of the performance of the operators. A similar experiment is performed to investigate the inverse extrapolation. In this case, a modelled data set is inverse extrapolated once with symmetric and once with asymmetric operators. Then both data sets are forward extrapolated with the same operator set and compared with the input data. Both experiments show that the accuracy of the operators decreases with the operator length. In general, the symmetric and asymmetric operators have a similar level of performance. The symmetric operators have less negative effects on the inverse extrapolation. In the forward extrapolation, the asymmetric operators introduce less artefacts.

Finally, the extrapolation operators are applied on simple modelled 2D data sets with homogeneous and layered backgrounds. Migration with symmetric operators for data sets with a small number of receivers introduces more artefacts. These are mainly generated at the outmost data points and are extrapolated further into the data. Especially in layered media, which is typical for the shallow subsurface, the asymmetric operators perform much better. The examples clearly show the advantage of the short asymmetric spatial operators for migration of seismic data from tunnelling applications. They contribute in creating an accurate image of the subsurface in front of the TBM and increase safety of the tunnelling activities.

# Samenvatting

---

## **De TBM, geen blinde mol!**

Deze thesis behandelt bepaalde aspecten van seismische beeldvorming in zachte grond voor een Tunnelboormachine, om tunnel constructeurs te helpen de ondergrond die ze naderen te “zien”, in plaats van de TBM vooruit te sturen als een “blinde mol”. De Nederlandse ondiepe ondergrond is zeer onregelmatig gelaagd and bevat veel heterogeniteiten. Geotechnische onderzoek van het terrein, zoals sonderingen en boringen, geeft enkel lokale informatie over de zachte ondergrond en interpolatie van deze gegevens is onnauwkeurig. Dit heeft invloed op de veiligheid tijdens het boren van de tunnel. Hoe meer informatie over de grond en de obstakels voor de TBM gekend is, hoe beter tunnel parameters gecontroleerd en schade aan de machine vermeden kan worden. Een seismisch onderzoek van het terrein levert informatie over laterale variaties in de ondergrond. In combinatie met de geotechnische gegevens kan een veel nauwkeuriger beeld van het tunnel traject gemaakt worden.

Uitvoeren van oppervlakte seismiek is niet altijd gemakkelijk, bv. in stedelijke gebieden. Dan is een seismisch systeem op de TBM een oplossing. Seismische energy, uitgezonden vanop de machine, reflecteert op contrasten voor het boorfront en wordt opgenomen door ontvangers op de TBM. The gereflecteerde energy levert de tunnel constructeurs een beeld van de ondergrond voor de TBM en verhoogt daardoor de veiligheid tijdens het tunnelboren.

De bron is een belangrijk element van elk seismisch systeem. Zijn eigenschappen moeten optimaal zijn zodat de uitgezonden signalen geschikt zijn voor de toepassing bij tunnelboren. In de ondiepe, zachte, Nederlandse ondergrond is het gebruik van schuifgolven te verkiezen boven druggolven omdat deze laatste meer beïnvloed worden door het water in de poriën. Omdat de losse grond grote demping veroorzaakt, is de bron best laagfrequent. Enkele praktische aspecten die onderzocht moeten worden zijn de positie van de bron (en ontvangers) op de TBM en het contact met de grond voor een perfecte overdracht van de seismische energie.

Het ontwerp van een bron valt buiten het bereik van dit onderzoek. In plaats van het ontwikkelen van een actieve bron, onderzoekt deze thesis eerst of de TBM zelf seismische energie uitzendt en, als dit het geval is, of ze geschikt is voor beeldvor-

ming in zachte grond. De bouw van de Tweede Heinoord Tunnel nabij Rotterdam is opgezet als een experimenteel project waarbij verschillende aspecten van tunnelboren in zachte grond in Nederland onderzocht worden. Seismische experimenten worden uitgevoerd op het aardoppervlak, in de ondergrond, in de TBM en in de tunnel. The eerste gefoonlijnen aan het grondoppervlak tonen registratie van seismische energie, komende van de TBM. Na verwerking van de gegevens, blijkt dat de TBM schuifgolven uitzendt met een frequentie bereik van 5 tot 100 Hz. Zoals al aangegeven zijn dit goede eigenschappen voor een seismische bron in zachte grond. Afhankelijk van de positie van de gefoonlijn worden events geregistreerd met een snelheid die varieëert van 100 tot 200 m/s. Dit zijn typische schuifgolf snelheden in zachte grond, sneller bij een hogere concentratie van zand, trager als er meer klei aanwezig is. Sommige metingen tonen duidelijke events met een regelmatige amplitude en periodiciteit. Op andere plaatsen kunnen ze zeer onregelmatig zijn en wordt de analyse van de gegevens dus moeilijker.

In combinatie met de metingen in de TBM zelf kan de bron van de seismische signalen bepaald worden. Motoren en pompen kunnen snel uitgesloten worden. De gefoons die vastgemaakt zijn aan de hydraulische vijzels registreren duidelijke pulsen. De hydraulische vijzels bevinden zich achteraan in de machine en zij duwen de TBM vooruit door zich af te zetten tegen de reeds geplaatste tunnelelementen. De vooruitgang van de TBM in de grond gebeurt niet altijd in een vloeiende beweging. Zij wordt beïnvloed door wrijvingseffecten tussen de machine en de grond errond. Waarschijnlijk zijn de seismische signalen afhankelijk van de werking van de hydraulische vijzels en daarom ook van het grondtype rond de TBM. Dit verklaart de variaties in amplitude en periodiciteit.

Om de geschiktheid van de TBM als seismische bron te testen, worden experimenten uitgevoerd in de ondergrond en in de tunnel. De prestatie van schuifgolf seismiek in zachte grond is zeer goed, maar voor toepassingen bij tunnelboren moet rekening gehouden worden met nieuwe factoren. Of de TBM gebruikt wordt als bron of een actieve bron ontwikkeld wordt, voor het in beeld brengen van de ondergrond voor de TBM is het snijrad de optimale positie voor het plaatsen van ontvangers. De bentoniet schild TBM die gebruikt wordt voor de constructie van de Tweede Heinoord Tunnel, pompt een viskeuze slurry naar het boorfront om zijn stabiliteit te waarborgen. Om seismische energie te kunnen registreren op het snijrad, is de doordringbaarheid van deze bentoniet voor schuifgolven cruciaal. Om oncontroleerbare invloeden van de hydraulische vijzels uit te sluiten, worden externe druk- en schuifgolf bronnen gebruikt in dit experiment. De ontvangers zijn gefoons op diepte, in het traject van de TBM, en druksensoren op het snijrad. De resultaten geven geen uitsluitel. The metingen van de gefoons geven aan dat de

golven sterk gedempt worden. Maar zelfs de drukgolven worden niet geregistreerd op het snijrad. Het is mogelijk dat de druksensoren niet geschikt zijn voor dit soort metingen. Maar als het probleem echt bij de doordringbaarheid van het bentoniet ligt, dan zijn aanpassingen aan de apparatuur nodig.

De efficiëntie van de vijzels als seismische bron wordt ook getest. Tijdens het boren van de tweede tunnelbuis van de Tweede Heinenoord Tunnel wordt de eerste buis gebruikt als sterke reflector in de zachte grond. Geofoons worden vastgemaakt aan de tunnelwand van de tweede tunnel. The metingen vertonen een zeer hoge signaal/ruis verhouding. Na het verwijderen van de directe golven die zich door de tunnelwand bewegen, kunnen de gereflecteerde events in de data aangeduid worden. Ze zijn heel erg zwak. Reflecties van heterogeniteiten voor de TBM zijn mogelijk dus nog moeilijker te detecteren. Om de TBM te kunnen toepassen als een efficiënte, betrouwbare en controleerbare bron is meer onderzoek nodig naar de werking van de hydraulische vijzels en de invloed van de grond rond de TBM.

Het theoretische deel van deze thesis bekijkt de verwerking van gegevens van een seismisch systeem voor tunnelboren waarbij ontvangers op de snijrad van de TBM geïnstalleerd zijn. Seismisch onderzoek voor olie- en gasexploratie wordt uitgevoerd over een heel groot gebied, met honderden ontvangers. Traditionele data-verwerkingstechnieken zijn geoptimaliseerd voor deze configuraties. In toepassingen voor tunnelboren zijn de ontvangers beperkt in opening door de diameter van de TBM en in aantal door de beschikbare plaats op het snijrad. Toepassing van bestaande verwerkingsmethodes, zoals phaseshift migratie, bij deze nieuwe configuratie zal sterke artefacts in de data brengen door het afkappen van de extrapolatie operator. Korte, symmetrische spatiële extrapolatie operatoren die stabiel zijn in een bepaald golfgetal interval zijn ontwikkeld met een gewogen kleinste kwadraten optimalisatie. Bij migratie in het spatiële in plaats van het frequentie domein wordt het mogelijk om rekening te houden met kleine laterale veranderingen in de grond (bij tunnelboren loodrecht op het snijrad). Bij een groot aantal ontvangers zal de rekentijd sterk verminderd worden. Bij tunnelboren is de lengte van de operator bepaald door de het aantal ontvangers op het snijrad. Symmetrische operatoren zijn echter enkel optimaal voor de middelste ontvanger. Voor de andere data punten wordt de operator verschoven en asymmetrisch afgekapt, wat nieuwe artefacts veroorzaakt. Ook wordt slechts een beperkt deel van de andere data punten meegenomen in de extrapolatie, wat niet efficiënt is als er sowieso slechts weinig gegevens beschikbaar zijn. Daarom is de gewogen kleinste kwadraten optimalisatie aangepast om korte, asymmetrische spatiële extrapolatie operatoren te ontwikkelen. Voor elk data punt wordt een nieuwe operator gemaakt, gebaseerd op het aantal ontvangers en de relatieve positie van het data punt, waarbij alle an-

dere data punten in rekening gebracht worden. Door het gewicht en de golfgetal interval waarin de operator nauwkeurig moet zijn te variëren, kan een optimale operator berekend worden. Het ontwerpen van een stabiele operator voor de uiterste punten vraagt nog extra aandacht.

De prestatie van de symmetrische en asymmetrische operatoren met verschillende operator lengte worden vergeleken, zowel in voorwaartse als inverse extrapolatie. In het voorwaartse experiment wordt een bron signaal voorwaarts geëxtrapoleerd, eenmaal met symmetrische en eenmaal met asymmetrische operatoren. Beide resultaten worden dan inverse geëxtrapoleerd met eenzelfde symmetrische methode zodat de verschillen in de uiteindelijke data enkel te wijten zijn aan de voorwaartse extrapolatie. Vergelijking met de oorspronkelijke invoer geeft een indicatie van de prestatie van de operatoren. Een gelijkaardig experiment is uitgevoerd voor de inverse extrapolatie. In dit geval is een gemodelleerde data set inverse geëxtrapoleerd, eenmaal met symmetrische en eenmaal met asymmetrische operatoren. Daarna worden beide resultaten voorwaarts geëxtrapoleerd met eenzelfde set symmetrische operatoren en vergeleken met de originele data. Beide experimenten tonen aan dat de nauwkeurigheid van de operatoren afneemt met de lengte van de operatoren. In het algemeen presteren de symmetrische en asymmetrische operatoren even goed. The symmetrische operatoren vertonen minder negatieve effecten in de inverse extrapolatie. In de voorwaartse extrapolatie veroorzaken de asymmetrische operatoren minder artefacts.

Uiteindelijk worden de extrapolatie operatoren toegepast op simpele gemodelleerde 2D data sets met homogene en gelaagde achtergronden. Migratie van data sets met een beperkt aantal ontvangers door symmetrische operatoren vertoont meer artefacts. Die zijn vooral veroorzaakt aan de uiterste data punten en dan verder in de data geëxtrapoleerd. Vooral in de gelaagde modellen, typisch voor de ondiepe ondergrond, geven de asymmetrische extrapolatie operatoren een beter resultaat. De voorbeelden tonen duidelijk het voordeel van de korte asymmetrische spatiële operatoren voor migratie van seismische data in toepassingen voor tunnelboren. Zij dragen bij in het nauwkeurig afbeelden van de ondergrond voor de TBM en vergroten daardoor de veiligheid van de activiteiten tijdens het boren van de tunnel.

# Curriculum Vitae

---

## PERSONAL

Name Gerda Swinnen  
Born March 31, 1974, Turnhout, Belgium  
Nationality Belgian

## EDUCATION

1986 - 1992 Mathematics - Sciences  
St. Jozefsinstituut, Herentals, Belgium

1992 - 1997 Catholic University Leuven, Belgium  
Burgerlijk Mijnbouwkundig Ir (MSc in Mining)  
MSc-thesis at Delft, University of Technology, The Netherlands  
*The effect of pressure on wave propagation in reservoir rocks*

1997 - 2003 Delft, University of Technology, The Netherlands  
Departement of Applied Earth Sciences  
PhD research: *Acoustic Monitoring for Tunnel Boring in Soft Soils*



## Acknowledgments / Dankwoord

---

The last pages of the book ... Time to thank some people for joining me in the happy times of the past few years and for helping me through the frustrations that came along too.

My first “thank you” goes to Jacob Fokkema, for luring another Belgian to Delft. Instead of giving me advice about working in the industry, which I came for in the first place, he offered a place in the geophysics group and a challenging research project. Guy Drijkoningen, as supervisor, kept me and the research on the right track (with the help of a lot of cookies!).

Research is not something you do on your own. Insights from others have guided me to this final result. The practical, geotechnical experience of Dominique Ngan-Tillard has certainly helped setting up the experiments on-site. I’ll always remember the tunnel fieldwork! For those, I also want to thank all the helping hands, Leo and Ab and all the people at the site of the Second Heinenoord Tunnel, both engineers and operators.

I have learned a lot from the theoretical discussions with Kees Wapenaar and Jan Thorbecke. Kees was always there to bring new ideas when I got stuck in a theoretical tangle. I would not have made it through the implementation without Jan. Thank you for helping me understand and edit the software and for enduring all my silly questions.

One thing that makes my time in Delft bring a smile on my face, is certainly the colleagues. And even while I was not there too much in the last year, it was always great fun to drop by at the office or at a DOGS borrel. Many new friends came, many old ones left already, Antonio, Deyan, Evert, Gerrit, Jan-Willem, Jeroen, Jeroen, Jesper, Kees, Lourens, Martijn, Menno, Michel, Ranajit, Rutger, Sevgi and of course all the students, especially the Boulogne crew. A special “thank you” goes to Rob, my light in the darkness of  $\LaTeX$  and Fortran, I know I’ve been a pain until the end. A big hug I’ve saved for Aletta, Hedi and Jan, for all the little frustrations and the great laughs (or was it the other way around?) we’ve shared.

Travelling between Essen and Delft every day, it became part of the routine. Chris, my train companion, we've survived! Thanks for the fun rides.

Sometimes a bit of "mysterious" distraction from the long working hours is necessary. (((Cori, Denyl, Ino and Nicky))), for being those "mystery friends" in every way.

"Ze werkt in Delft. Maar wat ze daar nu juist doet, dat moet je mij niet vragen!". Maar de steun van mama en papa, die is mij wel altijd duidelijk geweest. Bedankt!

Noël, mijn ventje. Voor te veel om op te noemen. Ik zou er nog een boek over kunnen schrijven (maar ik denk dat ik daar toch maar voor pas!). Kusje van je Gerdje.

*Yesterday was the deadline for all complaints.*